A numerical model of transient thermal transport phenomena in a high–temperature solid–gas reacting system for CO_2 capture applications

A THESIS
SUBMITTED TO THE FACULTY OF
UNIVERSITY OF MINNESOTA
BY

Lindsey Dat Kay Yue

IN PARTIAL FULFILLMENT OF THE REQUIREMENTS
FOR THE DEGREE OF
MASTER OF SCIENCE

Advised by Professor Wojciech Lipiński

October 2013

Acknowledgements

Thanks and love to my friends and family, who are walking this great journey through life with me, who have made me the person I am today, and who continue to help shape the person I will become tomorrow.

My gratitude to Professor Davidson, Professor Mantell, and Professor Northrop for listen to me and for sharing your wisdom and advice.

Thank you to my classmates, group-mates, and office-mates, who brought humanity and levity to my grad school experience.

And most of all, so much thanks to Professor Lipiński. Your technical exuberance and gentle guidance have been the predominate factors that kept me returning to my research day after day and without which I would not have accomplished all that I have.

Dedication

To all women who have ever felt like they had to—or couldn't ever—do anything. You *never* have to, and you can *always* try.

Abstract

A numerical model coupling transient radiative, convective, and conductive heat transfer and mass transfer to chemical kinetics of a heterogeneous solid−gas reacting system has been developed and applied to a model reaction: the decomposition of calcium carbonate into calcium oxide and carbon dioxide. The model reaction is one of two reactions involved in calcium oxide looping, a proposed thermochemical process suitable for use with concentrated solar power for the capture of carbon dioxide.

The analyzed system is a porous particle in a reactor–like environment that is subjected to concentrated solar irradiation. The system includes the solid particle and the fluid within the pore spaces. The two solid species are calcium carbonate and calcium oxide. The fluid is modeled as a mixture of two ideal gases: air and carbon dioxide. Mass transfer in the solid phase is due only to chemical reaction. The volumetric reaction model is employed for the decomposition reaction. Mass transfer in the fluid phase is due to chemical reaction, diffusion, and advection. Radiation and conduction in the particle are modeled, as well as convection between the solid and fluid phases within the particle and convection between the particle and surrounding environment. The solid phase is modeled as radiatively participating, while the fluid phase does not participate radiatively. The finite volume and explicit Euler methods are used to solve the governing equations numerically.

The model predicts the time-dependent temperature distributions as well as local solid and fluid phase composition. It is used to investigate operating conditions under which calcium oxide looping may be employed for carbon capture. These conditions are particle irradiation, ambient carbon dioxide concentration, and particle size. The sensitivity of the model to reaction rate, intraparticle mass transfer, surface radiative characteristics, and internal radiative heat transfer is also investigated.

Table of Contents

List of Tables

List of Figures

Nomenclature

$\bar{A}$	specific surface area ($m^2\ m^{-3}$)
C_2	second radiation constant, 14387.8 (μm K)
c	adsorption constant ($Pa^{-1/n}$)
c_0	adsorption constant pre-exponential factor ($Pa^{-1/n}$)
$\bar{c}_p$	molar specific heat capacity (J mol^{-1} K^{-1})
D	diffusivity ($m^2\ s^{-1}$)
d	diameter (m)
E_a	activation energy (J mol^{-1})
$E_{b\lambda}$	blackbody emissive power (W m^{-2})
E_c	adsorption constant energy (J mol^{-1})
f_v	volume fraction
$f\left(P_{CO_2}\right)$	functional dependence of reaction rate on CO_2 partial pressure
$f_{\lambda_1 T \to \lambda_2 T}$	blackbody fractional function
g	asymmetry factor of scattering
h	convective heat transfer coefficient (W m^{-2} K^{-1})
h_{mass}	convective mass transfer coefficient (m s^{-1})
$\bar{h}$	molar specific enthalpy (J mol^{-1})
$\Delta H^0_{298\ K}$	enthalpy of reaction (J mol^{-1})
$I_{b\lambda}$	spectral blackbody intensity (W μm^{-1} m^{-2} sr^{-1})
i	spatial index
j''	molar flux across the fluid–solid boundary (mol m^{-2})
K	permeability (m^2)
k	imaginary part of complex refractive index
k	thermal conductivity (W m^{-1} K^{-1})

k_B	Boltzmann constant, 1.38×10^{-23} (J K^{-1})
k_c	reaction rate constant (mol m^{-2} s^{-1})
k_0	reaction rate constant pre-exponential factor (mol m^{-2} s^{-1})
Kn	Knudsen number
L	characteristic length (m)
M	molar mass (kg mol^{-1})
m	complex refractive index
N	number of moles (mol)
N	number of nodes
n	real part of complex refractive index
n	cycle number
Nu	Nusselt number
p	pressure (Pa)
Pr	Prandtl number
Q	efficiency factor
$\mathbf{q}''_{rad}$	radiative flux vector
q''_{rad}	radiative flux (W m^{-2})
$\bar{R}$	ideal gas constant, 8.31451707 (J mol^{-1} K^{-1})
r	radius (m)
r''	surface reaction rate (mol m^{-2} s^{-1})
r'''	volumetric reaction rate (mol m^{-3} s^{-1})
Re	Reynolds number
Sc	Schmidt number
Sh	Sherwood number
T	temperature (K)
t	time (s)
$\mathbf{u}$	velocity vector
u	velocity (m s^{-1})

V	volume (m^3)
X	reaction extent
x	generic variable
x	size parameter
$\bar{y}$	molar fraction
∇	Nabla operator

Greek

α	absorptance
β	extinction coefficient (m^{-1})
ε	emittance
ζ	$C_2/\lambda T$
θ	angle of incidence
θ	fraction of occupied active sites
κ	absorption coefficient (m^{-1})
λ	mean free path length (m)
λ	wavelength (μm)
μ	viscosity (N s m^{-2})
ρ	mass density (kg m^{-3})
ρ	reflectance
$\bar{\rho}$	molar density (mol m^{-3})
$(\Sigma\upsilon)$	diffusion volume (m^3)
σ	Stefan–Boltzmann constant, 5.67×10^{-8} (W m^{-2} K^{-4})
σ_s	scattering coefficient (m^{-1})
ϕ	porosity
Ω	solid angle (sr)

Subscripts

$CaCO_3$	calcium carbonate
calc	calcination
CaO	calcium oxide
CO_2	carbon dioxide
cond	conductive
conv	convective
d	diameter
eff	effective
eq	equilibrium
e	extinction
f	fluid
g	gas diffusion coefficient
g	grain
i	incoming direction
i	spatial index
K	Knudsen
mass	convective mass transfer
mol	molecular
p	particle
phase	fluid–solid interface
R	Rosseland-mean
rad	radiative
surf	surface
s	scattering
s	solid
w	surrounding wall
0	initial state or condition

λ	spectral
$\|\|$	parallel
$\perp$	perpendicular
∞	ambient, free stream

Superscripts

f	fluid
n	time level
s	solid
tr	transport approximation
'	directional
$\cap$	hemispherical

Abbreviations

DM1	diffusion model 1
DM2	diffusion model 2
EM	effective medium
LTE	local thermal equilibrium
LTNE	local thermal non-equilibrium
ODM	optically discrete medium

Chapter 1 Introduction

Global climate change and rising atmospheric greenhouse gas levels have become ever increasing societal concerns. Human energy consumption and concomitant greenhouse gas emissions are predicted to only increase in the future, continuing to add to the level of carbon dioxide (CO_2) in the atmosphere. A field that has drawn significant attention because of these concerns is carbon capture and utilization (CCU). Technologies are being investigated and developed for both the capture of carbon dioxide and then the utilization of the captured CO_2.

The three categories of carbon capture that are currently being investigated are pre-combustion, oxy-combustion, and post-combustion CO_2 capture. Pre-combustion carbon capture typically involves the gasification of fuel into CO_2 and hydrogen gas (H_2) prior to use, and the CO_2 is separated from the hydrogen. Oxy-combustion carbon capture involves the combustion of fuel in pure oxygen instead of air. The resultant emissions are mostly water (H_2O) and carbon dioxide, and the CO_2 is separated from the H_2O. In post-combustion carbon capture, fuel is consumed in its usual manner, and CO_2 is separated from the emissions or flue gas [1]. CO_2 capture from the ambient atmosphere can also be considered a form of post-combustion capture, but generally involves different technologies or operating parameters, because of the large difference in CO_2 concentrations between flue gas (~5–15% CO_2 [2]) and ambient atmosphere (~400 ppm CO_2).

Post-combustion carbon capture methods include absorption, adsorption, membrane separation, and cryogenic separation [2]. All methods have an associated energy requirement in order to separate and concentrate the carbon dioxide. A proposed avenue for post-combustion carbon capture is solar thermochemical capture via calcium oxide looping [3], where CO_2 is chemically absorbed from a dilute source by a calcium oxide sorbent to form calcium carbonate. The calcium carbonate is thermochemically decomposed into concentrated carbon dioxide and regenerated calcium oxide with solar energy. The chemical reaction of calcium oxide and carbon dioxide forming calcium carbonate is referred to as carbonation; the reverse reaction, the chemical decomposition

of calcium carbonate into calcium oxide and carbon dioxide is referred to as calcination. The idealized cycle is shown in Figure 1.1.

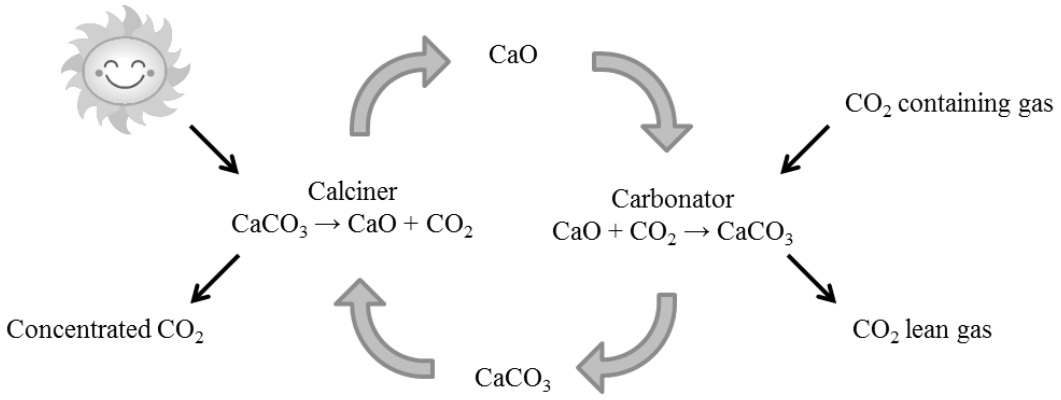

Figure 1.1 Calcium oxide looping carbon capture

Several length scales are involved in the realization of solar thermochemical technologies. These scales are shown in Figure 1.2 and include 10^{1}–10^{2} m at the solar plant level, 10^{-1}–10^{1} m at the reactor level, 10^{-2}–10^{-1} m at the reactor component level, and 10^{-8}–10^{-2} m at the component feature level.

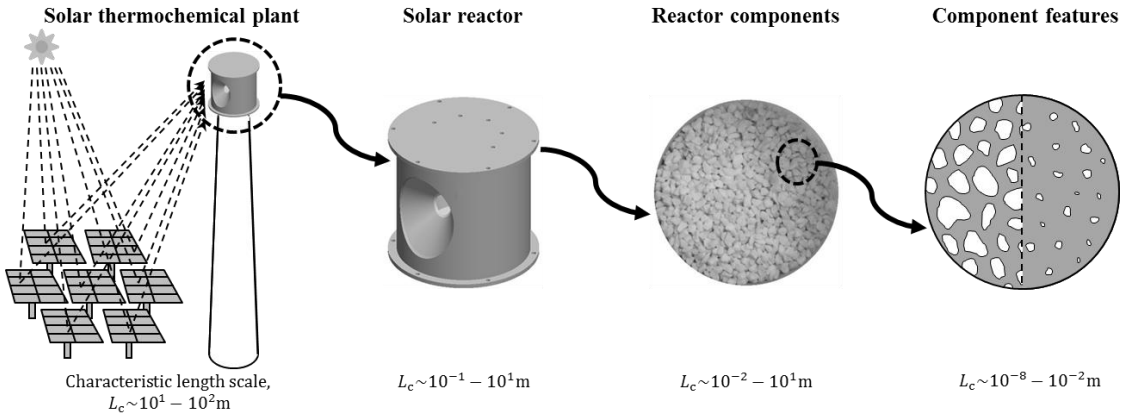

Figure 1.2 Length scales involved in solar thermochemical technologies

In a system for calcium oxide looping, the porous, sorbent particles are a component of interest. Numerical and experimental research has been conducted to investigate phenomena of interest on the particle level. Depending on implementation conditions, intraparticle heat transfer, mass transfer, and chemical kinetics can all be important considerations. Research topics on the particle level include radiation and heat

transfer characteristics [4][5][6], interaction with high flux solar irradiation [7], chemical kinetics of both the calcination reaction [8][9][10] and carbonation reaction [11][12][13], intraparticle mass transfer effects on kinetics [10][14][15], and sorbent degradation [16][17]. Numerical analysis on the single particle level has been conducted considering mass transfer with chemical kinetics [10][14][18] or heat and mass transfer with chemical kinetics [19][20][21]. These models have only considered one reaction direction: either carbonation or calcination, but not both to the best of the author's knowledge.

One aim of this work is to further the field of solar thermochemical carbon dioxide capture via calcium oxide looping by developing a rigorous numerical model encompassing heat and mass transfer with chemical kinetics for both reactions. A model such as this could be used to simulate a particle or group of particles in various reactor conditions and predict the amount of carbon dioxide captured. If extended to a group of particles, the model could be used to help guide reactor design and optimization. The work presented here is a step towards achieving the latter goal.

An important consideration for implementing a calcium oxide looping system is how fast both the carbonation and calcination reactions proceed. The two steps of the reaction pair are:

Exothermic, carbonation step:

$$\mathrm{CaO} + \mathrm{CO_2} \rightarrow \mathrm{CaCO_3}, \qquad \Delta H^0_{298\mathrm{K}} = -178 \text{ kJ mol}^{-1} \tag{1.1}$$

Endothermic, calcination step:

$$\mathrm{CaCO_3} \rightarrow \mathrm{CaO} + \mathrm{CO_2}, \qquad \Delta H^0_{298\mathrm{K}} = 178 \text{ kJ mol}^{-1} \tag{1.2}$$

The speed of a heterogeneous reaction depends on chemical kinetics, mass transfer, and heat transfer. If any of these processes does not occur as fast as the others, it limits the reaction. Temperature, reactant and product concentrations, and pressure can drive or limit a reaction based on Le Chatelier's principle. Carbonation will be mass transfer limited if carbon dioxide does not reach calcium oxide reaction sites; it will be heat transfer limited if heat from the exothermic reaction does not transfer away from the reaction site; and it will be kinetically limited if the previous two conditions are not met. Calcination will be mass transfer limited if the produced carbon dioxide does not leave

the reaction site; it will be heat transfer limited if heat to drive the endothermic reaction is not supplied to the reaction site; and it will be kinetically limited if the previous two conditions are not met. A model that accurately captures chemical kinetics, mass transfer, and heat transfer could be used to elucidate under which conditions a reaction is limited and what mode is limiting it. Knowing these limits will help to design a systems and in the choice of operating parameters of the system.

This work explores and compares methods for numerically modeling the physics involved in a decomposing calcium carbonate particle. Goals of the work include: 1) understanding the coupled heat transfer, mass transfer and chemical processes in the calcination reaction, 2) identifying the effects of physical parameters, and 3) evaluating the selected modeling methods.

Chapter 2 Model system

A semi-transparent, non-uniform, and porous particle is subjected to high-flux solar irradiation in a reactor-like environment. The system to be analyzed consists of solid and gas phases and is shown in Figure 2.1. The thermochemical calcination of calcium carbonate, Eq. (1.2), is selected as the model reaction because of its suitability as the endothermic step of the calcium oxide looping cycle for solar-driven CO_2 capture [22]. The solid phase is a mixture of calcium carbonate and calcium oxide while the fluid in the pore space is a mixture of air and carbon dioxide.

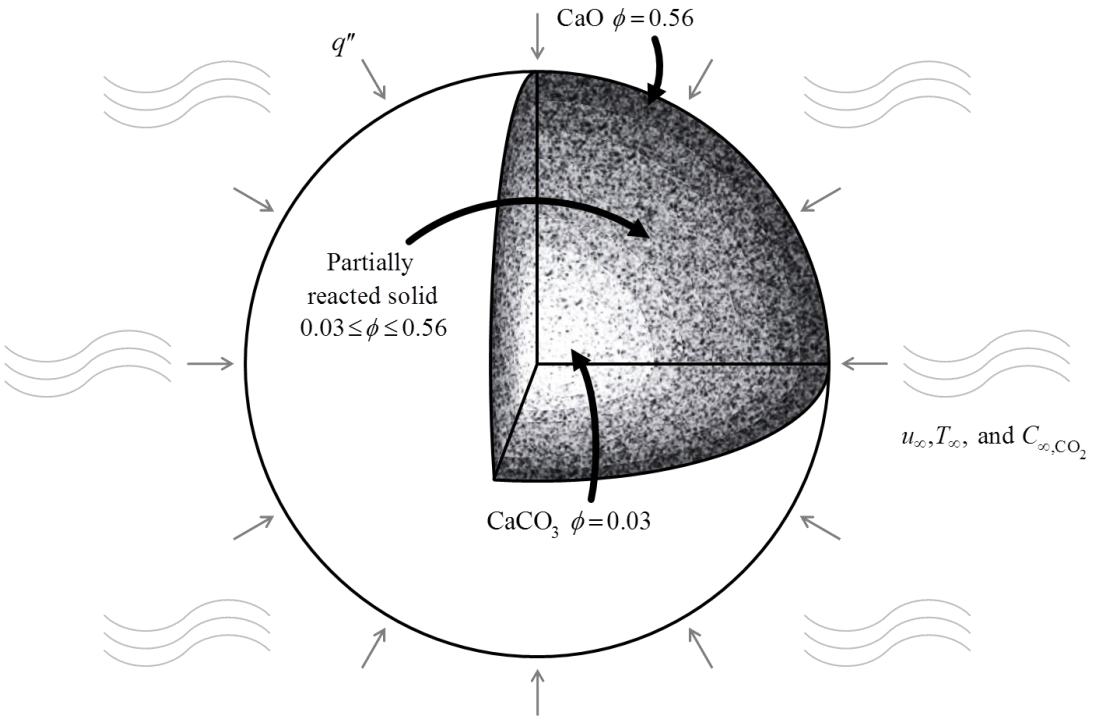

Figure 2.1 Reacting spherical particle

Radiation is incident on the particle surface causing the temperatures of the solid and fluid phases to rise. As the temperature increases, the particle undergoes heterogeneous thermochemical transformations, causing morphological and composition changes in the solid phase and fluid motion in the fluid phase.

2.1 Particle morphology

Several characteristic of the particle's morphology may change due to a chemical reaction. These characteristics include particle radius, porosity, interphase specific surface area, chemical reaction specific surface area, pore diameter, and solid species' grain size. The particle radius and radius of calcium oxide grains are assumed constant. Though size changes can occur when the particle reacts, change in particle size is not significant [9]. The size of calcium oxide grains is assumed constant to simplify radiation modeling, and the size of calcium carbonate grains are not considered in this analysis.

The remaining characteristics are internal and treated as variable. Models exist to describe how these characteristics change with particle composition. Models that are variants of the volumetric reaction model help define particle morphology, like the changing grain model [23] and the random pore model [24][25]. These models make assumptions about intraparticle features and how they change as the particle reacts. For example, the changing grain model assumes the particle is initially comprised of small, individual, nonporous grains of calcium carbonate, and the radius of the individual grains shrinks as they react. Using this model, the interphase specific surface area and chemical reaction specific surface area can be calculated from the total number of grains and the surface area of the individual solid grains.

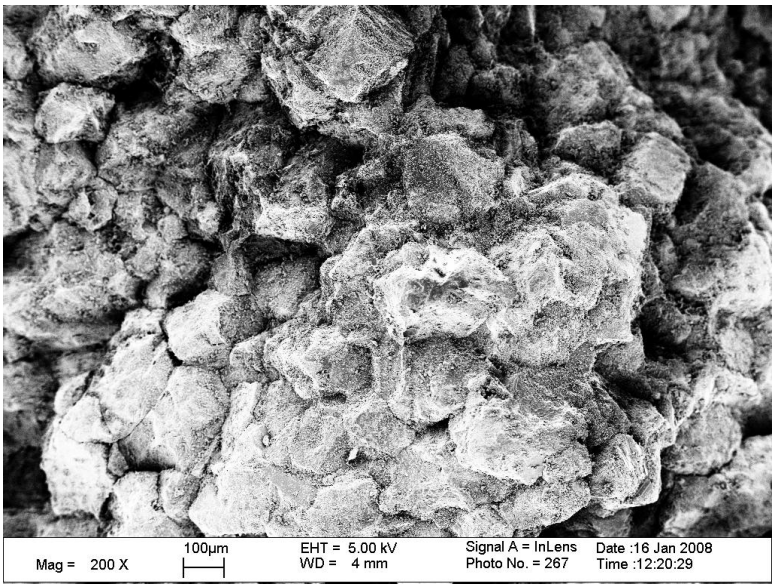

Figure 2.2 SEM image of unreacted calcium carbonate [6], reproduced with permission from ASME

An SEM image of the surface of a calcium carbonate particle, Figure 2.2 shows the calcium carbonate grains are neither spherical nor uniform. No assumptions have been made in this work about internal particle characteristics of calcium oxide grains in order to keep the model general. As a result, separate models for the internal characteristics have been selected or developed.

The porosity of limestone particles before and after calcination was measured by García-Labiano et al. [10]. The values for porosity and other material properties of unreacted Blanca limestone are used for calcium carbonate in this work. Properties of completely calcined Blanca limestone are used for calcium oxide. The values for the initial porosity of unreacted calcium carbonate $\phi_{0,\mathrm{CaCO_3}}$ and the final porosity of completely reacted calcium oxide $\phi_{0,\mathrm{CaO}}$ are presented in Table 2.1. A linear relationship between reaction extent and the initial and final porosity values is used to predict the local porosity of partially reacted solid ϕ. The relationship is

$$\phi = \phi_{0,\mathrm{CaCO_3}} - (Z-1)\left(1-\phi_{0,\mathrm{CaCO_3}}\right) X \tag{2.1}$$

$$Z = 1 + \frac{\rho_{\mathrm{CaCO_3}} \left(V_{\mathrm{M,CaO}} - V_{\mathrm{M,CaCO_3}}\right)}{M_{\mathrm{CaCO3}}} \tag{2.2}$$

where $\rho_{\mathrm{CaCO_3}}$ is the bulk mass density of calcium carbonate, $V_{\mathrm{M,CaO}}$ and $V_{\mathrm{M,CaCO_3}}$ are the molar volumes of calcium oxide and calcium carbonate respectively, and $M_{\mathrm{CaCO_3}}$ is the molar mass of calcium carbonate.

Table 2.1 Physical characteristics of calcium carbonate and completely reacted calcium oxide [10]

Parameter	Value	Units
$\phi_{0,\mathrm{CaCO_3}}$	0.03	
$\phi_{0,\mathrm{CaO}}$	0.56	
$\bar{A}_{0,\mathrm{CaCO_3}}$	300	$\mathrm{m^2\ kg^{-1}}$
$\bar{A}_{0,\mathrm{CaO}}$	19000	$\mathrm{m^2\ kg^{-1}}$

The value predicted by this relation for the porosity of completed reacted calcium oxide matches the value measured by García-Labiano et al. [10]. The relation is rearranged in a more intuitive manner for use in this work:

$$\phi = \phi_{0,\mathrm{CaCO_3}} + \left(1 - \phi_{0,\mathrm{CaCO_3}}\right)\left[1 - \left(\frac{\rho_{\mathrm{CaCO_3}}}{M_{\mathrm{CaCO_3}}} \times \frac{M_{\mathrm{CaO}}}{\rho_{\mathrm{CaO}}}\right)\right] X \tag{2.3}$$

The interphase specific surface area is the specific surface area of the interface between the solid and fluid phases. García-Labiano et al. [10] also measured the interphase specific surface area of unreacted calcium carbonate $\bar{A}_{0,\mathrm{CaCO_3}}$ and completely reacted calcium oxide $\bar{A}_{0,\mathrm{CaO}}$. Values are given in Table 2.1. They present a relationship for local interphase specific surface area as a function of reaction extent:

$$\bar{A}_{\mathrm{phase}} = \frac{\left[\left(1-X\right)\bar{A}_{0,\mathrm{CaCO_3}} + X\bar{A}_{0,\mathrm{CaO}}\right]}{\left[\frac{\left(1-X\right)}{\rho_{\mathrm{CaCO_3}}} + \frac{X}{\rho_{\mathrm{CaO}}}\right]}\left(1-\phi\right) \tag{2.4}$$

The relationship given by Eq. (2.4) is used in this work. It should be noted that the measured specific surface area values are $\mathrm{m^2\ kg^{-1}}$ while the units of $\bar{A}_{\mathrm{phase}}$ are $\mathrm{m^2\ m^{-3}}$.

Before any chemical conversion occurs, the interphase surface area corresponds to the chemical reaction surface area, because all of the solid surface exposed to the fluid phase is calcium carbonate. After the onset of reaction, part of the calcium carbonate is converted to calcium oxide, so the chemical reaction surface area is only the portion of the surface that is calcium carbonate. After the onset of reaction, the interphase surface area is the sum of the calcium carbonate and calcium oxide surface areas. The chemical reaction area should go to zero as the particle completely reacts, leaving no calcium carbonate surface.

Several models exist for predicting the reaction specific surface area, but it was found that a simple linear relationship accurately recreates previously published results without having to make limiting assumptions about the physical characteristics of the reacting solid. The reaction specific surface area is assumed to be linearly related to the

total specific surface area of unreacted calcium carbonate, $\bar{A}_{0,CaCO_3}$ and the local reaction extent, X

$$\bar{A}_{calc} = \left[\bar{A}_{0,CaCO_3} \rho_{CaCO_3} \left(1 - \phi_{0,CaCO_3}\right) \right] (1 - X) \tag{2.5}$$

where the mass density ρ_{CaCO_3} and the initial porosity $\phi_{0,CaCO_3}$ are included to give the reaction specific area the units of $m^2\ m^{-3}$.

Pore diameter is used to predict the effective diffusivity as well as the interphase heat transfer. The pore diameter expression used by García-Labiano et al. [10] is based on porosity and specific surface area.

$$d_{pore} = 4 \frac{\phi}{\bar{A}_{phase}} \tag{2.6}$$

An alternative method for approximating the pore diameter was analytically developed assuming perfectly spherical, non-interconnected pores and using the porosity and specific surface area. For spherical pores, the pore volume and surface area in terms of the pore radius are

$$V_{pore} = \frac{4}{3} \pi r_{pore}^3 \tag{2.7}$$

and

$$A_{pore} = 4 \pi r_{pore}^2 \tag{2.8}$$

The porosity and specific surface can be expressed in terms of the pore volume, pore surface area, and total number of pores of uniform size, N_{pores},

$$\phi = \frac{N_{pores} V_{pore}}{V_{total}} \tag{2.9}$$

and

$$\bar{A}_{phase} = \frac{N_{pores} A_{pore}}{V_{total}} \tag{2.10}$$

Solving for the number of pores and setting the two expressions equal to each other yields

$$\frac{\phi}{V_{\text{pore}}} = \frac{\bar{A}_{\text{phase}}}{A_{\text{pore}}} \tag{2.11}$$

The expressions for the volume of a pore and the surface area of a pore are substituted into the equation, and solving for the pore radius gives

$$r_{\text{pore}} = 3\frac{\phi}{\bar{A}_{\text{phase}}} \tag{2.12}$$

$$d_{\text{pore}} = 6\frac{\phi}{\bar{A}_{\text{phase}}} \tag{2.13}$$

This method for determining the pore diameter yields a theoretical maximum average value, because physically the pores are not perfectly spherical, and they are interconnected. This method predicts a higher, idealized value than the equation given by García-Labiano et al. [10]. The assumption of non-interconnected pores does not accurately represent the system. For those reason and for continuity, the equation predicting the lower value originally proposed by García-Labiano et al. [10] is used in this work.

2.2 Physical phenomena

The physical phenomena considered in the system are chemistry, mass transfer, and heat transfer. The reaction model and chemical kinetics expression used in this work are described in Chapter 3. Chemical kinetics depends on temperature, carbon dioxide concentration, and particle morphology.

Mass transfer in the solid phase is due only to chemistry, while mass transfer in the fluid phase is due to chemistry, species diffusion due to concentration gradients, and bulk advection due to pressure gradients. Gas expansion and chemical reaction create the pressure and concentration gradients that drive mass transfer in the fluid phase. Convective mass transfer occurs between the fluid in the particle pore spaces and the ambient fluid surrounding the particle. The equations and modeling methods are developed in Chapter 4.

The chemical reaction requires added process heat. Heat transfer from the surface to the reaction site is captured in the heat transfer model explained in Chapter 5. The

phases allowed to be at local thermal non-equilibrium (LTNE) and therefore can have different temperatures. Conduction is modeled in both the solid and fluid phases, with intraparticle convective heat transfer between the two phases. Internal radiative heat transfer is modeled in both phases, though the solid phase is radiatively participating while the fluid phase is radiatively non-participating. Convective heat transfer occurs between both the solid and fluid phases at the particle surface and the ambient surrounding fluid. All three physical phenomena are transient and coupled.

2.3 Assumptions

The model is developed with the following assumptions: 1) irradiation and external heat and mass transfer convection are uniform over the particle surface; 2) the incident irradiation is diffuse; 3) the particle radius does not change; 4) all pore spaces are active and connected to the particle exterior; 5) the gas phase is radiatively nonparticipating; 6) calcium carbonate is radiatively nonscattering; 7) calcium oxide grains are assumed to be uniform, spherical, and size $r_{g,CaO} = 0.472$ μm; 8) the solid phase is initially 100% calcium carbonate; 9) air and carbon dioxide act as ideal gases; 10) the only means of fluid mass transfer is by diffusion and advection in the pore space—fluid species do not diffuse into the solid phase; and 11) the surroundings are black and initially at radiative equilibrium with the particle.

2.4 Volume averaging

The governing equations of the mathematical model presented in this work are volume–averaged equations [26][27]. The equations are modified from a volume–averaged model developed by Keene et al. [28] for heat and mass transfer in a reacting heterogeneous medium.

Angle brackets are used to denote volume–averaged quantities. Quantities are averaged either over a single phase volume or over the total volume. Quantities averaged over a single phase—in this work either the fluid or solid phase—are intrinsic averages, and a superscript of ‘f’ or ‘s’ is used to denote the phase over which the averaging is applied. Quantities averaged over the total volume are superficial averages and do not

carry a superscript. Intrinsic and superficial averages are related by the porosity ϕ by the following relations:

$$\langle x \rangle = \phi \langle x \rangle^{\mathrm{f}} \tag{2.14}$$

$$\langle x \rangle = (1-\phi) \langle x \rangle^{\mathrm{s}} \tag{2.15}$$

The mathematical model consists of six coupled conservation equations: four conservation of mass equations for the four species of the system and two conservation of energy equations for the two phases. Additional constraint equations are the equation of state for the fluid phase and a simplified version of the fluid phase conservation of momentum equation. The unknowns are the molar densities of the four species, the temperatures of the two phases, the pressure of the fluid phase, and the velocity of the fluid phase, which vary in time and space. Each equation is presented and developed with appropriate closure equations in the chapters below.

Chapter 3 Chemistry

In this chapter, a chemical kinetic expression for the heterogeneous thermochemical decomposition of calcium carbonation is described. The expression accounts for particle morphology and reactant and product concentrations. The kinetics expression is used with the volumetric reaction model to model chemistry.

The calcination of solid calcium carbonate into solid calcium oxide and gaseous carbon dioxide is endothermic and requires process heat to drive thermal decomposition. Calcium carbonate is the primary component of naturally occurring limestone. It was experimentally observed that limestones decompose in the range 750–950°C under typical process conditions. Material properties and reaction kinetics for Blanca limestone are used in this work.

The local reaction extent is defined as the molar fraction of the particle that has reacted from calcium carbonate to calcium oxide.

$$X \overset{\text{def}}{=} 1 - \frac{\bar{\rho}_{\mathrm{CaCO_3}}}{\bar{\rho}_{0,\mathrm{CaCO3}}} \tag{3.1}$$

It is also equivalent to the molar fraction of calcium oxide in the solid. Chemical kinetics for each reacting constituent are quantified by the reaction rate. The rate is defined to be positive when calcium carbonate decomposes and defined as a volumetric rate for use with the volumetric reaction model.

$$r'''_{\mathrm{CaCO_3}} \overset{\text{def}}{=} -\frac{\mathrm{d}N_{\mathrm{CaCO_3}}}{\mathrm{d}V\mathrm{d}t} = r''' \tag{3.2}$$

$$r'''_{\mathrm{CaO}} \overset{\text{def}}{=} \frac{\mathrm{d}N_{\mathrm{CaO}}}{\mathrm{d}V\mathrm{d}t} = -r''' \tag{3.3}$$

$$r'''_{\mathrm{CO_2}} \overset{\text{def}}{=} \frac{\mathrm{d}N_{\mathrm{CO_2}}}{\mathrm{d}V\mathrm{d}t} = -r''' \tag{3.4}$$

Multiple reaction models have been used to accurately predict experimental calcination results, including (a) a uniform reaction model where the reaction is assumed to take place uniformly throughout the particle [29], (b) a shrinking core model with a well-defined boundary between the unreacted core and the surrounding reacted shell [30],

and (c) volumetric model which allows locations in the particle to be partially reacted [9][10]. Though accurate for certain cases, Khinast et al. suggest the uniform reaction model and shrinking core model can only accurately predict chemical reaction in extreme cases [9]. The volumetric reaction model has been used to accurately predict carbonation kinetics [13]. The volumetric reaction model has been selected for use in this work, because it accurately predicts calcination results, and it allows for extension of the model to include carbonation kinetics with similar numerical treatment as calcination kinetics in future work.

The reaction rate expression developed by García-Labiano et al. [10] for calcination has the form:

$$r''' = -k_{\mathrm{c,calc}} \bar{A}_{\mathrm{calc}} f\left(p_{\mathrm{CO_2}}\right) \tag{3.5}$$

where $k_{\mathrm{c,calc}}$ is the reaction rate constant, $\bar{A}_{\mathrm{calc}}$ is the reaction specific surface area, and $f\left(p_{\mathrm{CO_2}}\right)$ is the functional dependence of the reaction rate on the carbon dioxide partial pressure. The reaction rate constant was fit to measured data using the Arrhenius expression,

$$k_{\mathrm{c,calc}} = k_0 \exp\left(-\frac{E_{\mathrm{a}}}{\bar{R}T}\right) \tag{3.6}$$

The value fit from data in [10] for the pre-exponential factor is $k_0 = 6.7\times10^6$ mol m^{-2} s^{-1} and for the activation energy is $E_{\mathrm{a}} = 1.66\times10^5$ J mol^{-1}. The experiments were performed isothermally, so the solid and fluid phases were at equilibrium and had a single temperature value everywhere in the particle. These isothermal values are used in the Arrhenius expression to fit the pre-exponential factor and activation energy. In order to be used in the present model, which allows for LTNE between the phases and temperature gradients within the particle, an appropriate value for the temperature needed to be selected. The solid phase temperature was selected as the most appropriate value.

$$k_{\mathrm{c,calc}} = k_0 \exp\left(-\frac{E_{\mathrm{a}}}{\bar{R}\left\langle T_{\mathrm{s}}\right\rangle^{\mathrm{s}}}\right) \tag{3.7}$$

Four different methods for predicting the reaction rate dependence on carbon dioxide partial pressure $f\left(p_{\mathrm{CO_2}}\right)$ were investigated by García-Labiano et al. [10]. The first two expressions had been previously proposed in the literature. The second two methods use a Langmuir-Hinshelwood mechanism model shown in Eq. (3.8), with two different adsorption isotherms for the fraction of carbon dioxide occupied active sites $\theta_{\mathrm{CO_2}}$. García-Labiano et al. [10] found good agreement between measured data and the Langmuir–Hinshelwood mechanism model with the Freundlich isotherm for Blanca limestone. It is the model selected for use in this work. The Langmuir–Hinshelwood mechanism model is

$$f\left(p_{\mathrm{CO_2}}\right)=\left(1-\theta_{\mathrm{CO_2}}\right)\left(1-\frac{p_{\mathrm{CO_2}}}{p_{\mathrm{eq}}}\right) \tag{3.8}$$

where $p_{\mathrm{CO_2}}$ is the partial pressure of carbon dioxide and p_{eq} is the equilibrium partial pressure of carbon dioxide. The Freundlich isotherm for the fraction of occupied active sites is

$$\theta_{\mathrm{CO_2}}=c\left(p_{\mathrm{CO_2}}\right)^{1/n} \tag{3.9}$$

where the adsorption constant, c, has temperature dependence defined by

$$c=c_0\exp\left(-\frac{E_{\mathrm{c}}}{\bar{R}T}\right) \tag{3.10}$$

The fraction of occupied active sites is a fraction and therefore limited to the range $0\le\theta_{\mathrm{CO_2}}\le 1$. If the expression yields a value outside the allowable range, the limiting value is taken. Values fit to data for the exponent n, the adsorption constant pre-exponential factor c_0, and the adsorption constant energy E_{c} are 2, 1.8×10^{-7} $\mathrm{Pa^{-1/n}}$, and -9.3×10^{4} J mol^{-1}, respectively. Similar ambiguity exists for the temperature in Eq. (3.10) as did in Eq. (3.6) for the reaction rate constant. Again, the intrinsic average solid phase temperature was taken as the most appropriate value.

$$c=c_0\exp\left(-\frac{E_{\mathrm{c}}}{\bar{R}\left\langle T_{\mathrm{s}}\right\rangle^{\mathrm{s}}}\right) \tag{3.11}$$

The equation of state, formulated for carbon dioxide, is used to calculate the partial pressure of carbon dioxide.

$$p_{\mathrm{CO_2}} = \frac{N_{\mathrm{CO_2}} \bar{R} \left\langle T_{\mathrm{f}} \right\rangle^{\mathrm{f}}}{\phi V} \tag{3.12}$$

The following equation is used to calculate equilibrium partial pressure [31],

$$p_{\mathrm{eq}} = \left(4.137 \times 10^{12}\ \mathrm{Pa}\right) \exp\left(\frac{-2.0474 \times 10^{4}\ \mathrm{K}}{\left\langle T_{\mathrm{f}} \right\rangle^{\mathrm{f}}}\right) \tag{3.13}$$

The effect of the partial pressure of carbon dioxide on the reaction rate for varying temperatures and CO_2 concentrations at atmospheric pressure is shown in Figure 3.1. If no carbon dioxide is present in the ambient gas, there is no effect from CO_2 partial pressure on the reaction rate, and $f\left(p_{\mathrm{CO_2}}\right)$ is 1. When the concentration of carbon dioxide is high, it will prevent the system from reacting, and $f\left(p_{\mathrm{CO_2}}\right)$ is 0, until a high enough temperature is reached to overcome the influence of the carbon dioxide. This onset of reaction temperature increases as carbon dioxide concentration increases.

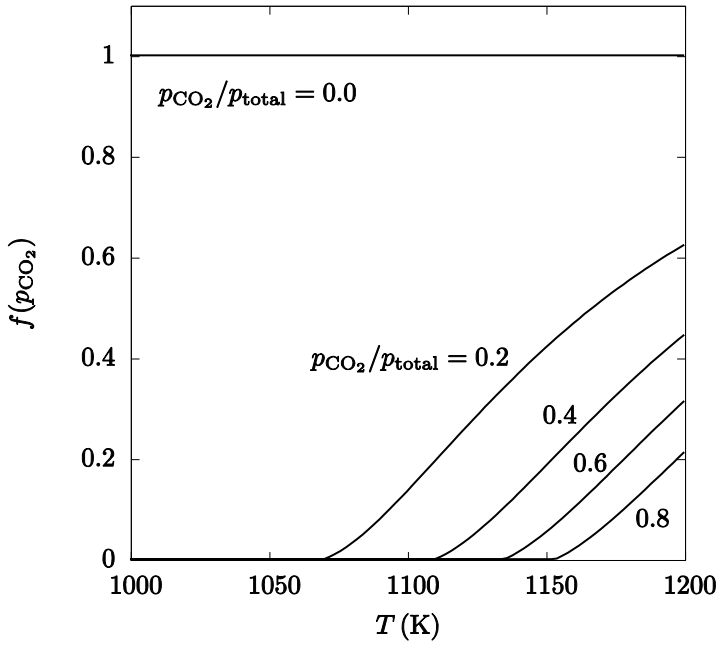

Figure 3.1 Effect of carbon dioxide concentration on reaction rate as a function of temperature

The temperature dependence of the reaction rate per reaction surface area for various carbon dioxide concentrations is shown in Figure 3.2. The reaction rate r'' increases with temperature and decreases with increasing carbon dioxide concentration.

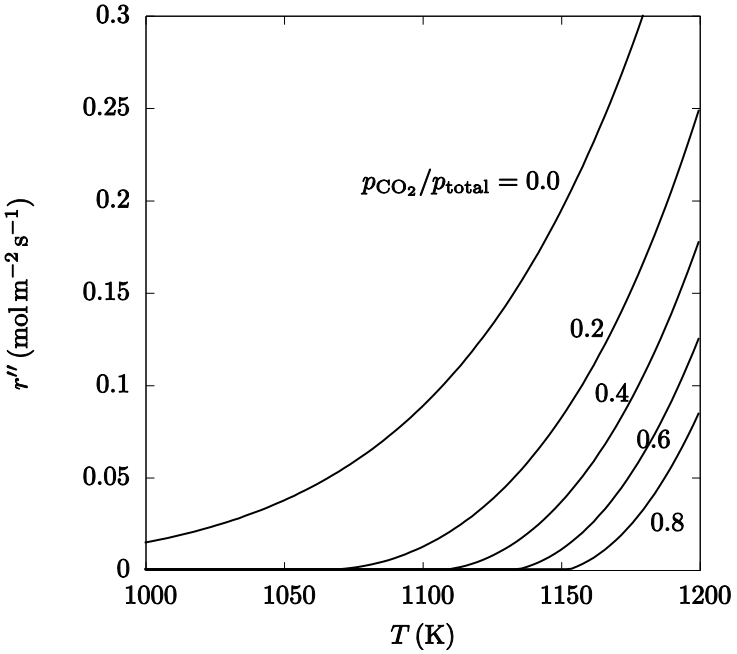

Figure 3.2 Reaction rate as a function of temperature for varying carbon dioxide concentrations

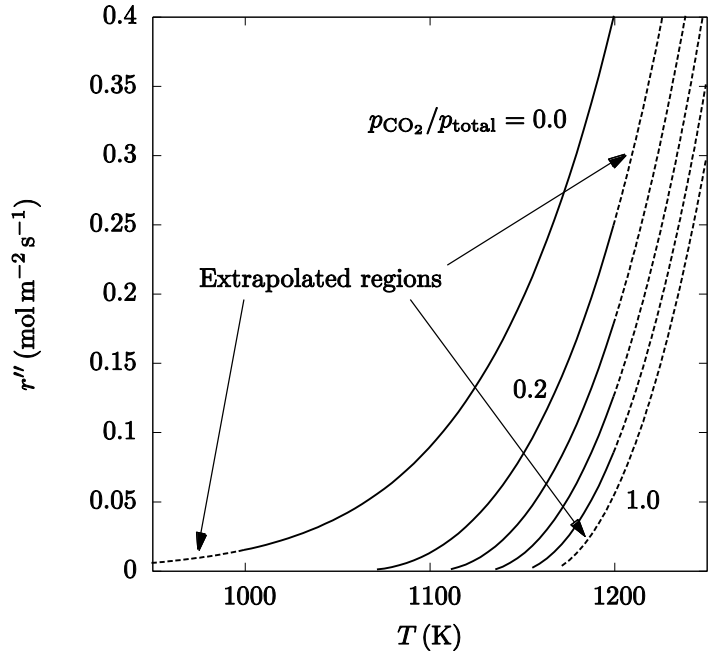

Figure 3.3 Extrapolated reaction rate as a function of temperature for varying carbon dioxide concentrations

The overall expression for the calcination reaction rate, Eq. (3.5), is valid for the range of experimental conditions investigated by García-Labiano et al. [10]. The investigated temperature range is 1048–1173 K; the particle diameter range is 0.4–2.0 mm; and the CO_2 concentration is 0–80%. The expression has been extrapolated and applied outside of the valid range for use in the current model. It is applied to higher and lower temperatures in the range 850–1500 K, to particles up to 10 mm in diameter, and at ambient carbon dioxide concentrations up to 99%. The extrapolated ranges are shown in Figure 3.3. Further investigation is warranted to address the applicability of the reaction model to systems outside the valid range.

Chapter 4 Mass transfer

In this chapter, the conservation of mass equations for the solid and fluid phases are described. In the solid phase, mass transfer is due to chemical reaction only. For the fluid phase, mass transfer is modeled as a combination of chemical reaction flux, diffusion, and advection.

The volume–averaged conservation of mass equation for calcium carbonate and calcium oxide read, respectively:

$$\frac{\partial\left[\left(1-\phi\right)\left\langle\bar{\rho}_{\mathrm{CaCO_3}}\right\rangle^{\mathrm{s}}\right]}{\partial t}=\left\langle r'''_{\mathrm{CaCO_3}}\right\rangle \tag{4.1}$$

$$\frac{\partial\left[\left(1-\phi\right)\left\langle\bar{\rho}_{\mathrm{CaO}}\right\rangle^{\mathrm{s}}\right]}{\partial t}=\left\langle r'''_{\mathrm{CaO}}\right\rangle \tag{4.2}$$

where the reaction rate term on the right hand side is the only source or sink of each solid species.

Two fluid species are considered in the model: carbon dioxide and air. Air is treated as a single species composed of 79% nitrogen and 21% oxygen [32]. The two mechanisms by which fluid species are transported that are considered in this work are species diffusion due to a concentration gradient and bulk advection due to a pressure gradient. The volume–averaged conservation of mass equation for air reads:

$$\frac{\partial\left(\phi\left\langle\bar{\rho}_{\mathrm{air}}\right\rangle^{\mathrm{f}}\right)}{\partial t}+\nabla\cdot\left(\left\langle\bar{\rho}_{\mathrm{air}}\right\rangle^{\mathrm{f}}\left\langle\mathbf{u}_{\mathrm{f}}\right\rangle\right)=\nabla\cdot\left(D_{\mathrm{air,eff}}\nabla\left\langle\bar{\rho}_{\mathrm{air}}\right\rangle^{\mathrm{f}}\right) \tag{4.3}$$

The first term is the storage term. Because the fluid phase is modeled as compressible gases and is comprised of multiple species, this term is allowed to be non-zero. The second term is the advection term and the right hand side term is the diffusion term.

The volume–averaged conservation of mass equation for carbon dioxide is given by:

$$\frac{\partial\left(\phi\left\langle\bar{\rho}_{\mathrm{CO_2}}\right\rangle^{\mathrm{f}}\right)}{\partial t}+\nabla\cdot\left(\left\langle\bar{\rho}_{\mathrm{CO_2}}\right\rangle^{\mathrm{f}}\left\langle\mathbf{u}_{\mathrm{f}}\right\rangle\right)=\nabla\cdot\left(D_{\mathrm{CO_2,eff}}\nabla\left\langle\bar{\rho}_{\mathrm{CO_2}}\right\rangle^{\mathrm{f}}\right)+j''_{\mathrm{CO_2}}\bar{A}_{\mathrm{phase}} \tag{4.4}$$

with the same terms as the air conservation of mass equation and the addition of a source term for mass flux across the phase boundary due to chemical reaction.

4.1 Diffusion

Two models for diffusion are investigated in this work. Diffusion model 1 (DM1) is taken from the method García-Labiano et al. [10] used for the effective diffusivity in the pores. It is used in this work with minor modifications. Diffusion model 2 (DM2) is an effective diffusivity model employed by Keene et al. [28].

In DM1, the effective diffusivity is calculated from the gas diffusion coefficient D_g and particle porosity:

$$D_{eff} = D_g \phi^2 \tag{4.5}$$

The gas diffusion coefficient is a combination of the binary molecular diffusivity D_{mol} and Knudsen diffusivity D_K,

$$D_g = \left(D_{mol}^{-1} + D_K^{-1} \right)^{-1} \tag{4.6}$$

The relation for binary molecular diffusivity was developed by Fuller et al. [33] and is presented below with conversion factors for S.I. units.

$$D_{mol,CO_2} = \frac{C \times T^{1.75} \left(M_{CO_2}^{-1} + M_{air}^{-1} \right)^{0.5}}{p \left[\left(\Sigma \upsilon \right)_{CO_2}^{1/3} + \left(\Sigma \upsilon \right)_{air}^{1/3} \right]^2} \tag{4.7}$$

where T is the fluid temperature in K, M is the molar mass in kg mol^{-1}, p is the total fluid pressure in Pa, and $(\Sigma \upsilon)$ is the diffusion volume in m^3. The constant C is 1.01325×10^{-2} m^3 kg$^{1.5}$ s^{-3} K$^{-1.75}$ mol$^{-0.5}$. Diffusion volumes calculated by Fuller et al. [33] for carbon dioxide and air are 26.9 m^3 and 20.1 m^3, respectively.

García-Labiano et al. [10] only applied the effective diffusivity model to carbon dioxide, but it has been extended to air as well in this work. Since only two fluid species are considered, the binary molecular diffusivity of carbon dioxide in air is equivalent to the binary molecular diffusivity of air in carbon dioxide, and the same value is used for both species.

$$D_{\mathrm{mol,CO_2}} = D_{\mathrm{mol,air}} = D_{\mathrm{mol}} \tag{4.8}$$

The Knudsen diffusivity for carbon dioxide is given by

$$D_{\mathrm{K,CO_2}} = 194 d_{\mathrm{pore}} \sqrt{\frac{T}{M_{\mathrm{CO_2}}}} \tag{4.9}$$

where d_{pore} is the pore diameter. The equation has been extended to air in the following manner

$$D_{\mathrm{K,air}} = 194 d_{\mathrm{pore}} \sqrt{\frac{T}{M_{\mathrm{air}}}} \tag{4.10}$$

The molar diffusivity, the Knudsen diffusivity, and the gas diffusion coefficient for air and carbon dioxide are compared in Figure 4.1. The molar diffusivity at higher temperatures is orders of magnitude larger than both the Knudsen diffusivity and the gas diffusion coefficient.

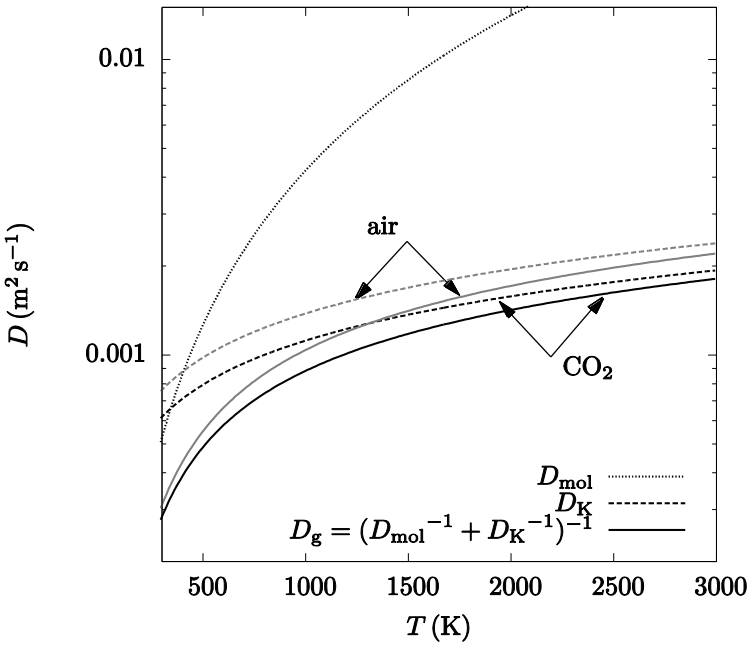

Figure 4.1 Binary molar diffusivity, Knudsen diffusivity, and the gas diffusion coefficient as functions of temperature for air and carbon dioxide

In the DM2, binary molecular diffusivity is downgraded by the particle porosity to find the effective diffusivity.

$$D_{\mathrm{eff}} = \phi D_{\mathrm{mol}} \tag{4.11}$$

In DM2, the effective diffusivity for carbon dioxide is identical to the effective diffusivity for air. The volume–averaged fluid temperature and pressure are used to evaluate the effective diffusivity in both models.

In the present work, the minimum porosity of the solid is 3% and the maximum is 56%. Effective diffusivity for these porosity bounds is shown in Figure 4.2 for both DM1 and DM2. The models vary from less than one order of magnitude to up to almost three orders of magnitude for the lowest porosity. They vary less when porosity is low and more when porosity increases.

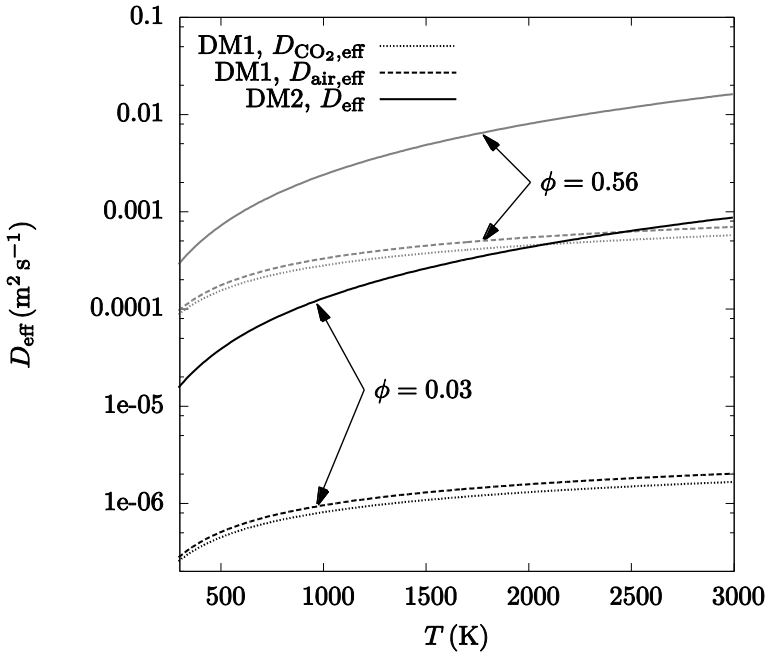

Figure 4.2 Comparison of effective diffusivity models versus temperature for different porosities

The Knudsen number relates the mean free path length λ of a fluid molecule to the characteristic length of the system containing the fluid L. In this work, the mean free path is for the CO_2 and air molecules. The characteristic length is the average pore diameter. The equations for Knudsen number and mean free path length read, respectively:

$$\mathrm{Kn} = \frac{\lambda}{L} \tag{4.12}$$

$$\lambda = \frac{k_{\mathrm{B}} T}{\sqrt{2}\pi p d_{\mathrm{mol}}^2} \tag{4.13}$$

where k_{B} is the Boltzmann constant, T is the temperature of the fluid in K, p is the fluid pressure in Pa, and d_{mol} is the diameter of the molecule in m.

The maximum average pore diameter is found in unreacted calcium carbonate and has the value 2×10^{-7} m. The minimum pore diameter is in calcium oxide and has the value 8×10^{-8} m. The diameter of a molecule of air or carbon dioxide is 3.8×10^{-10} m [32]. The maximum mean free path length occurs when the fluid in the particle is at ambient conditions before heating and is approximately 6.4×10^{-8} m. The minimum mean free path length occurs in the particle at the completion of chemistry when the pressure is at its maximum value. The minimum length is approximately 5.5×10^{-9} m.

The Knudsen number for the system then ranges from 10^{-1} to 10^{-2}. Knudsen diffusion becomes important for Knudsen numbers close to 1 but can be neglected for Knudsen numbers much less than 1. The Knudsen number for the system do not fall far enough to one extreme or another to make conclusions about the importance of Knudsen diffusivity based solely on the Knudsen number.

4.2 Advection

The relationship between bulk fluid velocity and pressure is found by solving Darcy's law simplification of the fluid phase conservation of momentum equation. The volume–averaged equation for momentum which yields fluid bulk fluid velocity is:

$$-\nabla\left(\phi\left\langle p_{\mathrm{f}}\right\rangle^{\mathrm{f}}\right) = \frac{\mu_{\mathrm{f}}}{K}\phi\left\langle \mathbf{u}_{\mathrm{f}}\right\rangle \tag{4.14}$$

where μ_{f} is the viscosity of the fluid phase, K is the permeability of the porous solid phase, and $\left\langle \mathbf{u}_{\mathrm{f}}\right\rangle$ is the superficial fluid velocity. The local fluid pressure is evaluated using the equation of state for the fluid phase: the ideal gas law.

$$\left\langle p_{\mathrm{f}} \right\rangle^{\mathrm{f}} = \left(\left\langle \bar{\rho}_{\mathrm{CO_2}} \right\rangle^{\mathrm{f}} + \left\langle \bar{\rho}_{\mathrm{air}} \right\rangle^{\mathrm{f}} \right) \bar{R} \left\langle T_{\mathrm{f}} \right\rangle^{\mathrm{f}} \tag{4.15}$$

For some systems, a relationship between the permeability and porosity exists. An example is the Kozeny–Carman equation for laminar flow through a packed bed of solids. Unfortunately for carbonate rocks such as the Blanca limestone considered in this work, no relation between porosity and permeability appears to exist. Zinszer and Pellerin [34] conclude from data taken for about 1500 carbonate rock samples that even though it is common practice to adopt porosity-permeability relationships, there is no relation between porosity and permeability for carbonate rocks.

In lieu of a relationship between permeability and porosity, the permeability of the solid in this work is calculated from values of permeability reported for naturally occurring dolomite limestone and industrial lime mortar. A range of permeability for dolomite limestone is given in [27], and the upper limit of the range, 4.5×10^{-14} m^2, is used for calcium carbonate. The value 4.37×10^{-13} m^2 measured for industrial lime [35] is used for calcium oxide. The two values are then molar weighted by the reaction extent.

$$K_{\mathrm{s}} = K_{\mathrm{CaCO_3}} \left(1 - X\right) + K_{\mathrm{CaO}} X \tag{4.16}$$

4.3 Surface convective mass transfer

The convective boundary condition for the fluid phase conservation of mass equations is determined with a correlation for convective mass transfer for a sphere in a flow. The correlation is [36]

$$\mathrm{Sh}_d = 2 + 0.6\,\mathrm{Re}_d^{0.5}\,\mathrm{Sc}^{1/3} \tag{4.17}$$

where Sh_d is the diameter based Sherwood number, Re_d is the diameter based Reynolds number, and Sc is the Schmidt number of the surrounding flow. The Sherwood number is the ratio of convective mass transfer and diffusive mass transfer

$$\mathrm{Sh}_d = \frac{d_{\mathrm{p}} h}{D} \tag{4.18}$$

where d_p is the diameter of the sphere in the flow, h is the convective mass transfer coefficient, and D is the diffusivity. The following definitions are used to evaluate the Reynolds and Schmidt numbers, respectively:

$$\mathrm{Re} = \frac{2 r_0 u_\infty \rho_\infty}{\mu_\infty} \tag{4.19}$$

$$\mathrm{Sc} = \frac{\mu_\infty}{\rho_\infty D_{\mathrm{CO}_2}\big|_{T=T_\infty, P=P_\infty}} \tag{4.20}$$

where r_0 is the radius of the particle, u_∞ is the free stream fluid velocity, ρ_∞ is the mass density of the free stream fluid, and μ_∞ is the viscosity of the free stream fluid. The mass transfer coefficient is obtained using the Sherwood number,

$$h_{\mathrm{mass}} = \frac{\mathrm{Sh}_d \, D_{\mathrm{CO}_2}\big|_{T=T_\infty, P=P_\infty}}{2 r_0} \tag{4.21}$$

Finally, the effective mass transfer coefficient is

$$h_{\mathrm{mass,eff}} = \phi h_{\mathrm{mass}} \tag{4.22}$$

An effective mass transfer coefficient is used with the volume averaged equations, because fluid mass transfer at the boundary is determined by mass transfer in the particle pore space and mass transfer away from the particle. The boundary between these two regions is the fraction of the particle surface that is pore space, which is equivalent to the porosity.

Chapter 5 Heat transfer

The three modes of heat transfer—radiation, conduction, and convection—have been included in the analysis. In the solid and fluid phases, conduction is considered. Interphase convection occurs between the solid porous media and the fluid within the pores. In the fluid phase, heat is advected by bulk fluid motion and diffuses with species motion. Convective heat transfer occurs at the boundary between both phases and ambient conditions. Radiative transfer in the particle is analyzed, as well as radiation incident on the particle surface interacting with both phases.

The volume–averaged conservation of energy equation for the solid phase read:

$$\frac{\partial\left[\left(1-\phi\right)\left\langle\bar{\rho}_{\mathrm{s}}\right\rangle^{\mathrm{s}}\left\langle\bar{h}_{\mathrm{s}}\right\rangle^{\mathrm{s}}\right]}{\partial t}=\nabla\cdot\left(k_{\mathrm{s,eff}}\nabla\left\langle T_{\mathrm{s}}\right\rangle^{\mathrm{s}}\right)-\left\langle\nabla\cdot\mathbf{q}''_{\mathrm{rad}}\right\rangle \\ -j''_{\mathrm{CO_2}}\bar{A}_{\mathrm{phase}}\bar{h}_{\mathrm{CO_2}}-h_{\mathrm{conv}}\bar{A}_{\mathrm{phase}}\left(\left\langle T_{\mathrm{s}}\right\rangle^{\mathrm{s}}-\left\langle T_{\mathrm{f}}\right\rangle^{\mathrm{f}}\right) \tag{5.1}$$

where the left hand side of the equation is the energy storage term. The terms on the right hand side of the equation are the energy fluxes due to convection, radiation, enthalpy crossing phases due to chemistry, and convective heat transfer between the phases.

The volume–averaged conservation of energy equation for the fluid phase is:

$$\frac{\partial\left(\phi\left\langle\bar{\rho}_{\mathrm{f}}\right\rangle^{\mathrm{f}}\left\langle\bar{h}_{\mathrm{f}}\right\rangle^{\mathrm{f}}\right)}{\partial t}+\nabla\cdot\left(\left\langle\bar{\rho}_{\mathrm{f}}\right\rangle^{\mathrm{f}}\left\langle\bar{h}_{\mathrm{f}}\right\rangle^{\mathrm{f}}\left\langle\mathbf{u}_{\mathrm{f}}\right\rangle\right)=\nabla\cdot\left(\left\langle\bar{h}_{\mathrm{CO_2}}\right\rangle^{\mathrm{f}}D_{\mathrm{CO_2,eff}}\nabla\left\langle\bar{\rho}_{\mathrm{CO_2}}\right\rangle^{\mathrm{f}}\right) \\ +\nabla\cdot\left(\left\langle\bar{h}_{\mathrm{air}}\right\rangle^{\mathrm{f}}D_{\mathrm{air,eff}}\nabla\left\langle\bar{\rho}_{\mathrm{air}}\right\rangle^{\mathrm{f}}\right)+\nabla\cdot\left(k_{\mathrm{f,eff}}\nabla\left\langle T_{\mathrm{f}}\right\rangle^{\mathrm{f}}\right) \\ +j''_{\mathrm{CO_2}}\bar{A}_{\mathrm{phase}}\bar{h}_{\mathrm{CO_2}}+h_{\mathrm{conv}}\bar{A}_{\mathrm{phase}}\left(\left\langle T_{\mathrm{s}}\right\rangle^{\mathrm{s}}-\left\langle T_{\mathrm{f}}\right\rangle^{\mathrm{f}}\right) \tag{5.2}$$

where the terms on the left hand side are the storage term and energy flux due to bulk advection. The terms on the right hand side are energy fluxes due to carbon dioxide enthalpy diffusion, air enthalpy diffusion, enthalpy convection, carbon dioxide enthalpy crossing phases due to chemistry, and convective heat transfer between the phases.

5.1 Effective conductivity

The conductivity of the two species, solid phase is calculated by molar weighting the temperature depended conductivities of the individual species:

$$k_{\text{cond,s}} = (1 - X)\, k_{\text{CaCO}_3} + X k_{\text{CaO}} \tag{5.3}$$

The solid conductivity then is downgraded by the solid volume fraction to give the effective solid conductivity:

$$k_{\text{s,eff}} = (1 - \phi)\, k_{\text{cond,s}} \tag{5.4}$$

The fluid phase conductivity and effective conductivity are treated in a similar manner:

$$k_{\text{cond,f}} = \frac{\left\langle \bar{\rho}_{\text{CO}_2} \right\rangle^{\text{f}} k_{\text{CO}_2} + \left\langle \bar{\rho}_{\text{air}} \right\rangle^{\text{f}} k_{\text{air}}}{\left\langle \bar{\rho}_{\text{CO}_2} \right\rangle^{\text{f}} + \left\langle \bar{\rho}_{\text{air}} \right\rangle^{\text{f}}} \tag{5.5}$$

$$k_{\text{f,eff}} = \phi k_{\text{cond,f}} \tag{5.6}$$

Expressions for the conductivity of the species are given in the Appendix.

5.2 Interphase convective heat transfer

The correlation for convective heat transfer used in by Keene et al. [26] for interphase heat transfer is reproduced in this work. The correlation is for heat transfer in packed bed of particle solid particles with flow around them. It is here to describe the heat transfer between the solid pore walls and fluid in the pores. The correlation is based on the diameter based Reynolds number of the flow and the Prandtl number of the fluid, Pr [37].

$$\text{Nu}_d = 2 + 1.1 \text{Re}_d^{0.6}\, \text{Pr}^{1/3} \tag{5.7}$$

The diameter based Nusselt number, Nu_d is evaluated using an average diameter of the pores in place of the diameter of the particles.

$$\text{Nu}_d = \frac{h_{\text{conv}} d_{\text{pore}}}{k_{\text{cond,f}}} \tag{5.8}$$

where h_{conv} is the interphase heat transfer coefficient. The Reynolds number is also evaluated with an average pore diameter. The equation is

$$\mathrm{Re}_d = \frac{\left\langle \rho_\mathrm{f} \right\rangle^\mathrm{f} u_\mathrm{f} d_\mathrm{pore}}{\mu_\mathrm{f}} \tag{5.9}$$

where $\left\langle \rho_\mathrm{f} \right\rangle^\mathrm{f}$ is the mass density of the fluid, u_f is the fluid velocity, and μ_f is the fluid viscosity.

The Prandtl number of the fluid is calculated by molar weighting the Prandtl numbers of each fluid species.

$$\mathrm{Pr} = \frac{\left\langle \bar{\rho}_{\mathrm{CO}_2} \right\rangle^\mathrm{f} \mathrm{Pr}_{\mathrm{CO}_2} + \left\langle \bar{\rho}_\mathrm{air} \right\rangle^\mathrm{f} \mathrm{Pr}_\mathrm{air}}{\left\langle \bar{\rho}_{\mathrm{CO}_2} \right\rangle^\mathrm{f} + \left\langle \bar{\rho}_\mathrm{air} \right\rangle^\mathrm{f}} \tag{5.10}$$

The following equation is used to evaluate the species Prandtl numbers.

$$\mathrm{Pr} = \frac{\bar{c}_\mathrm{p} \mu}{Mk} \tag{5.11}$$

Properties for the Prandtl number are evaluated at the volume–averaged fluid temperature in the pore space. The Nusselt number is calculated and used to solve for the interphase heat transfer coefficient.

$$h_\mathrm{conv} = \frac{k_\mathrm{cond,f} \mathrm{Nu}_d}{d_\mathrm{pore}} \tag{5.12}$$

5.3 Surface convective heat transfer

The correlation used for surface convective heat transfer was proposed by Whitaker [38] for flow past a single particle.

$$\mathrm{Nu}_d = 2 + \left(0.4\,\mathrm{Re}_\infty^{1/2} + 0.06\,\mathrm{Re}_\infty^{2/3}\right)\mathrm{Pr}_\infty^{0.4}\left(\frac{\mu_\infty}{\mu_\mathrm{f}\big|_{r=r_0}}\right)^{1/4} \tag{5.13}$$

The Nusselt number in this case is evaluated using the particle diameter and the free stream fluid conductivity.

$$\mathrm{Nu}_d = \frac{2h_\mathrm{surf} r_0}{k_\infty} \tag{5.14}$$

The Reynolds number is evaluated by Eq. (4.19), and Prandtl number is evaluated by Eq. (5.11) for the free stream fluid and conditions.

The surface heat transfer coefficient is solved for using the Nusselt number.

$$h_{\text{surf}} = \frac{k_{\infty}\text{Nu}_d}{2r_0} \tag{5.15}$$

The effective surface heat transfer coefficient for the solid and fluid phases are, respectively:

$$h_{\text{s,eff}} = (1-\phi)h_{\text{surf}} \tag{5.16}$$

$$h_{\text{f,eff}} = \phi h_{\text{surf}} \tag{5.17}$$

5.4 Radiative heat transfer

The Rosseland diffusion approximation is used to model radiative heat transfer within the particle. It has been shown that the Rosseland diffusion approximation yield similar results to a full solution of the radiation transport equation for a particle of size and optical properties considered in the model [19]. The Rosseland diffusion approximation is [39]

$$\mathbf{q}''_{\text{rad}} = -k_{\text{rad}}\nabla T \tag{5.18}$$

where k_{rad} is radiative conductivity. The radiative conductivity is a function of refractive index, temperature, and the Rosseland-mean extinction coefficient β_{R}:

$$k_{\text{rad}} = \frac{16n^2\sigma T^3}{3\beta_{\text{R}}} \tag{5.19}$$

$$\frac{1}{\beta_{\text{R}}} = \frac{\pi}{4n^2\sigma T^3}\int_{\lambda=0}^{\infty}\frac{n^2}{\beta_{\lambda}}\frac{dI_{\text{b}\lambda}}{dT}\,d\lambda \tag{5.20}$$

In order to evaluate the Rosseland-mean extinction coefficient, the complex refractive index of the medium, m is defined. Electromagnetic wave theory and Mie theory are used to evaluate the spectral scattering coefficient, κ_{λ} and the spectral absorption coefficient, σ_{λ} from the complex refractive index. These coefficients define β_{λ}, the spectral extinction coefficient. The spectral extinction coefficient is used directly with the gray band approximation of Eq. (5.19) to evaluate the radiative conductivity.

Refractive indices of $CaCO_3$, CaO, and the fluid phase

Refractive indices are defined for solid calcium carbonate, solid calcium oxide, porous calcium oxide, and the fluid phase. The real component for all indices of refraction is assumed to be constant for all wavelengths. Values for real components are given in Table 5.1. The real part of the complex refractive index of non-porous calcium oxide is greater than unity and taken to be 1.84. Porous calcium oxide is assumed to not refract light, and the real part of the complex refractive index is 1.

Table 5.1 Real refractive indices

Parameter	Value	Ref.
$n_{\lambda,\mathrm{CaCO_3}} = n_{\mathrm{CaCO_3}}$	1.55	[7][40]
$n_{\lambda,\mathrm{CaO}} = n_{\mathrm{CaO}}$	1.84	[40]
$n_{\lambda,\mathrm{CaO,porous}} = n_{\mathrm{CaO,porous}}$	1	[19]
$n_{\lambda,\mathrm{f}} = n_{\mathrm{f}}$	1	

Imaginary refractive indices for calcium carbonate [7][41] and calcium oxide [19] [40] are functions of wavelength and approximated from experimental data. For calcium carbonate:

$$k_{\lambda,\mathrm{CaCO_3}} = \begin{cases} a_1 \exp\left[b_1 \lambda^2\right] + c_1 \exp\left[d_1\left(\lambda^2 - \lambda_1^2\right)\right] & \lambda \le 3 \\ a_2 & \lambda > 3 \end{cases} \tag{5.21}$$

where a_1 is 0.004, b_1 is -10 μm^{-2}, c_1 is 0.1, d_1 is 0.2 μm^{-2}, λ_1 is 3 μm, and a_2 is 0.1.

For calcium oxide:

$$k_{\lambda,\mathrm{CaO}} = \begin{cases} a_1 \exp\left(b_1 \lambda\right) & 0 < \lambda \le 8.5 \\ a_2 \lambda + b_2 & 8.5 < \lambda \le 10.5 \\ a_3 \lambda + b_3 & 10.5 < \lambda \le 12.25 \\ a_4 \lambda^2 + b_4 \lambda + c_4 & 12.25 < \lambda \le 14 \\ a_5 \lambda + b_5 & 14 < \lambda \le 14.1 \\ a_6 \lambda + b_6 & 14.1 < \lambda \le 14.8 \\ a_7 \lambda + b_7 & 14.8 < \lambda \le 14.97 \\ a_8 \lambda + b_8 & 14.97 < \lambda \le 15.05 \\ a_9 \lambda + b_9 & 15.05 < \lambda \le 16.32 \\ a_{10} \lambda + b_{10} & 16.32 < \lambda \le 17 \\ a_{11} & 17 < \lambda \end{cases} \tag{5.22}$$

where the values of the constant in Eq. (5.22) are given in Table 5.2.

Table 5.2 Values for calculating the imaginary part of the complex refractive index for calcium oxide

Parameter	Value	Units	Parameter	Value	Units
a_1	1.0292		a_6	0.2667	μm^{-1}
b_1	-0.288	μm^{-1}	b_6	-3.347	
a_2	0.0092	μm^{-1}	a_7	0.3294	μm^{-1}
b_2	0.108		b_7	-4.2753	
a_3	0.0366	μm^{-1}	a_8	-0.2	μm^{-1}
b_3	-0.272		b_8	3.65	
a_4	0.665	μm^{-2}	a_9	0.315	μm^{-1}
b_4	-1.6079	μm^{-1}	b_9	-4.1002	
c_4	9.8967		a_{10}	0.5294	μm^{-1}
a_5	-0.27	μm^{-1}	b_{10}	-7.6	
b_5	0.794		a_{11}	1.4	

The fluid phase is non-absorbing so the imaginary refractive index is taken to be 0.

$$k_{\lambda,\mathrm{f}} = k_{\mathrm{f}} = 0 \tag{5.23}$$

The real and imaginary refractive indices for solid calcium carbonate and calcium oxide are shown as a function of wavelength in Figure 5.1.

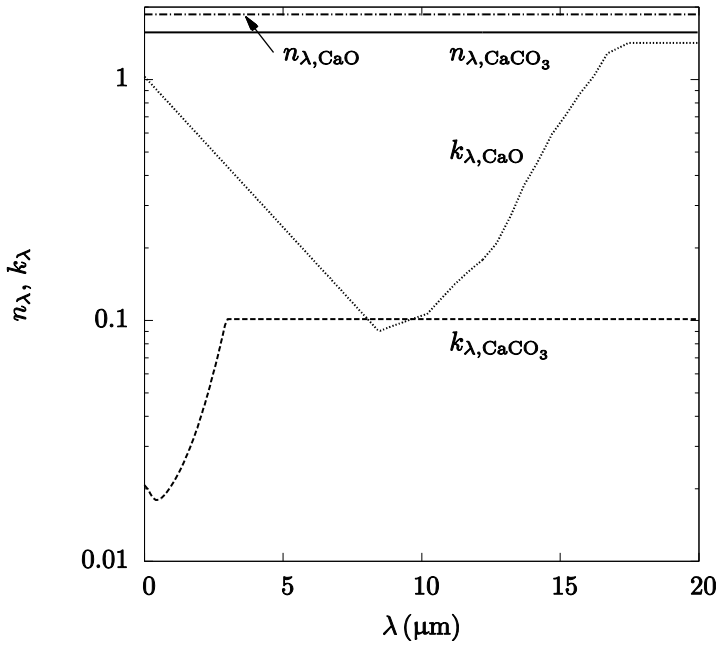

Figure 5.1 Real and imaginary refractive indices for bulk calcium carbonate and calcium oxide

Absorption, scattering, and extinction coefficients

Spectral extinction coefficients for calcium carbonate and calcium oxide are evaluated. Electromagnetic wave theory [39] is used to calculate the spectral extinction coefficient for calcium carbonate with the following:

$$\kappa_{\lambda,\mathrm{CaCO_3}} = \frac{4\pi k_{\lambda,\mathrm{CaCO_3}}}{\lambda} \tag{5.24}$$

Calcium carbonate is assumed to be non-scattering, so the scattering coefficient is set to zero.

$$\sigma_{\lambda,\mathrm{CaCO_3}} = 0 \tag{5.25}$$

The spectral extinction coefficient is the combination of the extinction and scattering coefficients [39]:

$$\beta_{\lambda,\mathrm{CaCO_3}} = \kappa_{\lambda,\mathrm{CaCO_3}} + \sigma_{\lambda,\mathrm{CaCO_3}} \tag{5.26}$$

Calcium oxide is modeled locally as evenly dispersed spherical grains of uniform size. These dense calcium oxide grains scatter and absorb light. Mie theory is used to calculate the efficiency factor for extinction $Q_{\mathrm{e}\lambda}$, the efficiency factor for scattering $Q_{\mathrm{s}\lambda}$, and asymmetry factor of scattering g. The BHMIE subroutine [42] is employed. Particle size

parameter x and the ratio of grain material complex refractive index to host refractive index $m_{\lambda,\text{ratio}}$ are inputs to the BHMIE subroutine and are evaluated by:

$$x = \frac{2\pi r_{\text{g,CaO}}}{\lambda} \tag{5.27}$$

$$m_{\lambda,\text{ratio}} = \frac{m_{\lambda,\text{CaO}}}{n_{\text{CaCO}_3}} = \frac{n_{\text{CaO,bulk}} + ik_{\lambda,\text{CaO}}}{n_{\text{CaCO}_3}} \tag{5.28}$$

The subroutine evaluates the following Mie theory equations:

$$Q_{\text{e}\lambda} = \frac{2}{x^2}\sum_{n=0}^{\infty}(2n+1)\Re(a_n + b_n) \tag{5.29}$$

$$Q_{\text{s}\lambda} = \frac{2}{x^2}\sum_{n=0}^{\infty}(2n+1)\left(|a_n|^2 + |b_n|^2\right) \tag{5.30}$$

The efficiency factors are used to evaluate at the absorption and scattering coefficients with the following equations:

$$\kappa_{\lambda,\text{CaO}} = \frac{3}{4}\frac{f_{\text{v,CaO}}}{r_{\text{g,CaO}}}(Q_{\text{e}\lambda} - Q_{s\lambda}) \tag{5.31}$$

$$\sigma_{\lambda,\text{CaO}} = \frac{3}{4}\frac{f_{\text{v,CaO}}}{r_{\text{g,CaO}}}Q_{s\lambda} \tag{5.32}$$

$$f_{\text{v,CaO}} = \frac{X(1-\phi_0)\rho_{\text{CaCO}_3}M_{\text{CaO}}}{\rho_{\text{CaO}}M_{\text{CaCO}_3}} \tag{5.33}$$

Spherical calcium oxide grains are assumed to be uniform in size for the calculation of the optical behavior, i.e. particle radius $r_{\text{g,CaO}}$ is constant. The volume fraction of calcium oxide $f_{\text{v,CaO}}$ changes with particle composition. The absorption coefficient for calcium carbonate and the absorption and scattering coefficients for calcium oxide are shown in Figure 5.2.

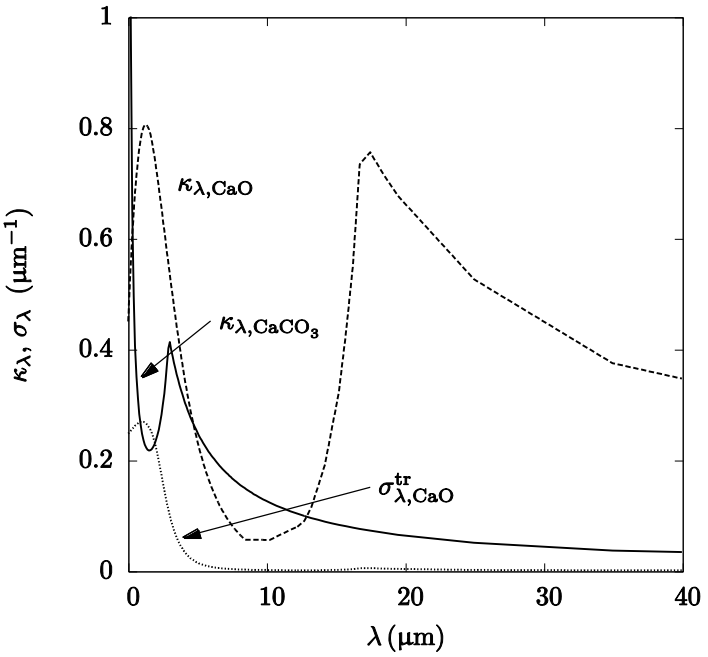

Figure 5.2 Absorption and scattering coefficients for calcium carbonate and calcium oxide as functions of wavelength

The transport approximation for the scattering coefficient is applied by the following equations [43]:

$$\sigma_{\lambda,\mathrm{CaO}}^{\mathrm{tr}} = (1-g)\,\sigma_{\lambda,\mathrm{CaO}} \tag{5.34}$$

The extinction coefficient with the transport approximation for calcium oxide is

$$\beta_{\lambda,\mathrm{CaO}}^{\mathrm{tr}} = \kappa_{\lambda,\mathrm{CaO}} + \sigma_{\lambda,\mathrm{CaO}}^{\mathrm{tr}} \tag{5.35}$$

The spectral extinction coefficients as function of wavelength for calcium carbonate and calcium oxide are compared in Figure 5.3. The effect of the transport approximation on the spectral extinction coefficient for calcium oxide is shown in Figure 5.4. The transport approximation decreases the scattering coefficient to account for the forward scattering of radiation. An effective extinction coefficient is used for the two species of the solid phase.

$$\beta_{\lambda,\mathrm{eff}} = (1-X)\,\beta_{\lambda,\mathrm{CaCO_3}} + X\,\beta_{\lambda,\mathrm{CaO}}^{\mathrm{tr}} \tag{5.36}$$

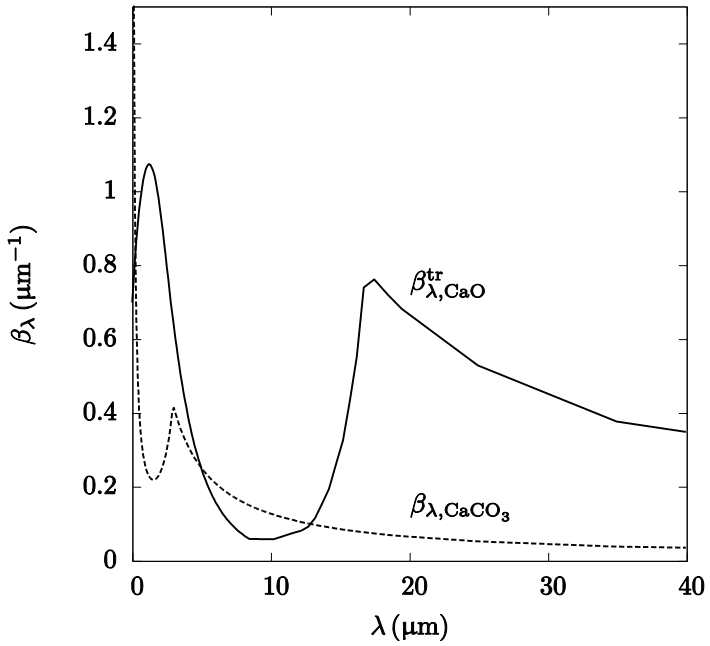

Figure 5.3 Spectral extinction coefficients for calcium carbonate and calcium oxide as a function of wavelength

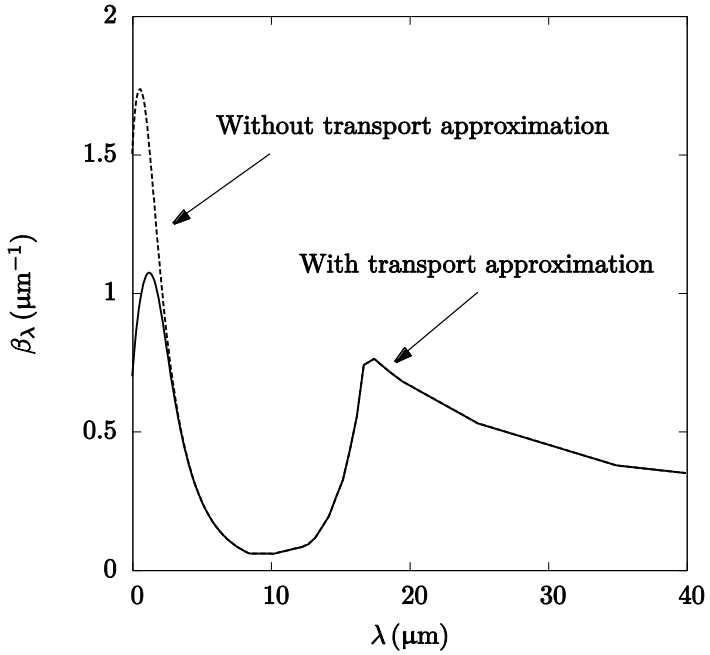

Figure 5.4 Spectral extinction coefficient for calcium oxide as a function of wavelength with and without the transport approximation

Gray band approximation

The gray band approximation [4] is used to evaluate radiative conductivity. It is used to approximate the indefinite integral of the extinction coefficient in Eq. (5.20):

$$k_{\text{rad}} \approx \frac{4}{3}\sigma T^3 \left\{ \frac{1}{\beta_{\lambda,\text{eff}}\big|_{0-\lambda_1}} \left[4 f_{0-\lambda_1 T} + \frac{15}{\pi^4} \frac{\zeta_1^4}{\text{e}^{\zeta_1} - 1} \right] \right.$$
$$+ \frac{1}{\beta_{\lambda,\text{eff}}\big|_{\lambda_1-\lambda_2}} \left[4 f_{\lambda_1 T-\lambda_2 T} + \frac{15}{\pi^4} \left(\frac{\zeta_2^4}{\text{e}^{\zeta_2} - 1} - \frac{\zeta_1^4}{\text{e}^{\zeta_1} - 1} \right) \right] \tag{5.37}$$
$$\left. + \ldots + \frac{1}{\beta_{\lambda,\text{eff}}\big|_{\lambda_n-\infty}} \left[4 f_{\lambda_n T-\infty} - \frac{15}{\pi^4} \frac{\zeta_n^4}{\text{e}^{\zeta_n} - 1} \right] \right\}$$

$$\zeta = C_2 / \lambda T \tag{5.38}$$

120 discrete wavelength bands are used based on the behavior of the extinction coefficient as a function of wavelength for the evaluation of Eq. (5.37). An effective radiative conductivity is used in the same manner as effective conductivity.

$$k_{\text{rad,eff}} = (1-\phi) k_{\text{rad}} \tag{5.39}$$

The radiative conductivity is added to the solid phase effective conductivity.

5.5 Surface radiation properties

The boundary condition for the solid phase conservation of energy equation requires the absorptance and emittance of the particle surface. Both properties are calculated from the reflectance using the following equations:

$$\alpha = 1 - \rho_{T_{\text{solar}}} \tag{5.40}$$

$$\varepsilon = 1 - \rho_{T_{\text{surface}}} \tag{5.41}$$

where α is the total, hemispherical absorptance, ε is the total, hemispherical emittance, $\rho_{T_{\text{solar}}}$ is the total, hemispherical reflectance averaged over the solar spectrum, and $\rho_{T_{\text{surface}}}$ is the total, hemispherical reflectance averaged over the spectrum of a blackbody at the same temperature as the particle surface.

The total reflectance is calculated using electromagnetic wave theory. Fresnel equations are first used to evaluate the spectral, directional-hemispherical reflectance of the interface using the refractive index of the ambient fluid (medium 1) and the refractive index of the solid phase (medium 2). Medium 2 is modeled as a combination of calcium carbonate, calcium oxide, and fluid in the pore space. The spectral, directional–hemispherical reflectance is averaged over all directions and wavelengths to evaluate the appropriate total, hemispherical reflectance. The reflectance is then used in Eqs. (5.40) and (5.41) to evaluate the total, hemispherical absorptance and emittance, respectively.

Four different models for the surface radiative properties are presented and investigated in this work. The models are based on two assumptions: (a) the absorption of medium 2 and (b) the relative surface feature size of medium 2 compared to wavelength. For assumption (a), Medium 2 is modeled as either absorbing or non-absorbing. For assumption (b), if the surface features are assumed much smaller than the incident wavelength, the effective medium (EM) assumption is used for medium 2. If the surface features are assumed much larger than the incident wavelength, the optically discrete medium (ODM) assumption is used for medium 2. SEM images and the spectral distribution of the incident radiation should be used to assess the surface feature to wavelength relation. The four models are outlined in Table 5.3.

Table 5.3 Surface radiative property models

	Effective medium	Optically discrete medium
Non-absorbing medium	Model 1: EM, $k_2 = 0$	Model 2: ODM, $k_2 = 0$
Absorbing medium	Model 3: EM, $k_2 \neq 0$	Model 4: ODM, $k_2 \neq 0$

Figure 5.5a outlines the steps for evaluating the surface absorptance and emittance for Models 1 and 3, assuming an EM. Figure 5.5b outlines the steps for evaluating the surface absorptance and emittance for Models 2 and 4, assuming an ODM. Model 1 has been previously employed in literature [19][21].

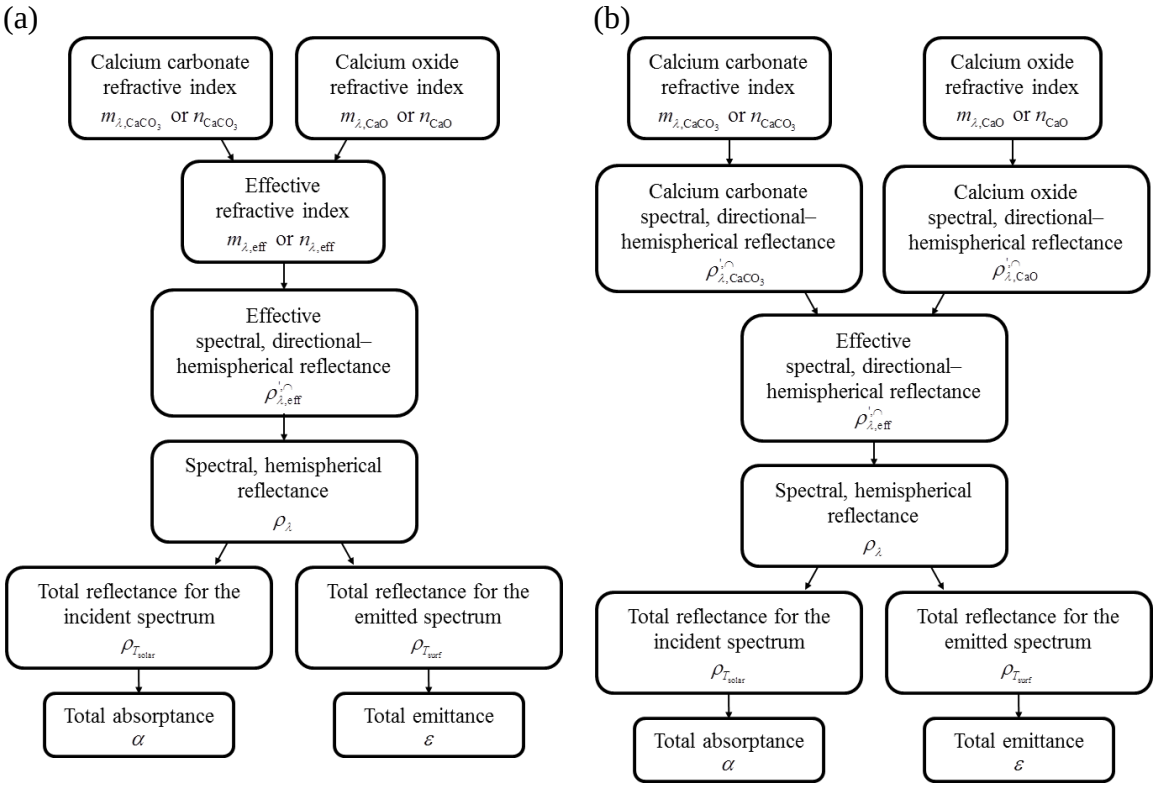

Figure 5.5 Flowchart for calculating absorptance and emittance assuming (a) effective medium and (b) optically discrete medium

This work follows the convention established in [39] for referring to surface radiative properties. The three surface properties of interest are reflectance, absorptance and emittance. Properties are spectral or total and directional or hemispherical. Spectral properties are specific to single wavelength while total properties have been averaged over all wavelengths. Directional properties are specific to a direction while hemispherical properties are averaged over the all directions. Hemispherical absorptance is averaged over all incoming direction. Hemispherical emittance is averaged over all outgoing directions. Hemispherical reflectance is averaged twice over the incoming and outgoing directions.

Absorbing versus non-absorbing medium

For medium 1, the complex refractive index of air is used regardless of the composition of the fluid phase. It is treated as a non-scattering, non-absorbing media, so the real and imaginary parts of the refractive index are, respectively:

$$n_1 = n_{\lambda,\text{air}} = 1 \tag{5.42}$$

$$k_1 = k_{\lambda,\text{air}} = 0 \tag{5.43}$$

Medium 2 is a mixture of calcium carbonate, calcium oxide, and fluid in the pore space. In all models, the refractive index of fluid in the pore space is taken as Eqs. (5.42) and (5.43). In all models, the real part of a solid component's refractive index is taken as the respective value given in Section 5.4. The value for the imaginary part of a solid component's refractive index depends on the surface radiative property model. When medium 2 is modeled as absorbing (Models 3 and 4), the imaginary refractive indices for the solid components are allowed to be the non-zero values described above: Eq. (5.21) for calcium carbonate and Eq. (5.22) for calcium oxide. When the medium is modeled as non-absorbing, the imaginary component of the refractive index of medium 2 is assumed to be zero.

$$k_{\lambda,\text{CaCO}_3} = k_{\lambda,\text{CaO}} = k_2 = 0 \tag{5.44}$$

Effective versus optically discrete medium

Models 1 and 3 assume an EM which is valid when the feature size of the surface is much smaller than the incident wavelength. In the current system, there are islands of calcium carbonate and calcium oxide as well as pores spaces. This yields three different feature sizes: the characteristic length of the islands of each solid species and the pore spaces. All three should be smaller than the incident wavelength for the EM assumption to be applicable. Numerically this can be expressed as

$$\frac{L_{\text{CaCO}_3}}{\lambda} \ll 1 \tag{5.45}$$

$$\frac{L_{\text{CaO}}}{\lambda} \ll 1 \tag{5.46}$$

$$\frac{L_{\text{pore}}}{\lambda} \ll 1 \tag{5.47}$$

where L_{CaCO_3} is the characteristic length of calcium carbonate islands, L_{CaO} is the characteristic length of calcium oxide islands, and L_{pore} is the characteristic length of the pore spaces. If all feature sizes are small compared to the wavelength, the refractive indices are mixed based on surface composition to yield an effective complex refractive index for the medium.

$$n_{\lambda,\text{eff}} = n_2 = (1-\phi)\left[(1-X)\, n_{\lambda,\text{CaCO}_3} + X n_{\lambda,\text{CaO,porous}}\right] + \phi n_{\lambda,\text{f}} \tag{5.48}$$

$$k_{\lambda,\text{eff}} = (1-\phi)\left[(1-X)\, k_{\lambda,\text{CaCO}_3} + X k_{\lambda,\text{CaO}}\right] + \phi k_{\lambda,\text{f}} \tag{5.49}$$

Models 2 and 4 assume an ODM where the surface feature size is much larger than the incident wavelength.

$$\frac{L_{\text{CaCO}_3}}{\lambda} \gg 1 \tag{5.50}$$

$$\frac{L_{\text{CaO}}}{\lambda} \gg 1 \tag{5.51}$$

$$\frac{L_{\text{pore}}}{\lambda} \gg 1 \tag{5.52}$$

In this case, an effective refractive index is not used. Instead the spectral, directional-hemispherical reflectance of the individual surface components is calculated from the components' individual refractive indices. The distinction between the two paths is shown in the flowcharts in Figure 5.5.

Fresnel equations

The Fresnel equations are employed to calculate the spectral, directional-hemispherical reflectance for the interface between medium 1 and medium 2. The Fresnel equations are applied to effective refractive index in models assuming am EM in the same manner as it is applied to the refractive indices of the individual components in models assuming an ODM.

The Fresnel equations take the refractive index of medium 1 n_1, the complex refractive index of medium 2 $m_2 = n_2 + ik_2$, and the incident angle of radiation θ and yield two components of the spectral, direction–hemispherical reflectance, $\rho_{\lambda,\perp}$ and $\rho_{\lambda,\parallel}$. The spectral, directional–hemispherical reflectance $\rho'^{\cap}_{\lambda}$ is the average of these two values.

$$p^2 = \frac{1}{2}\left[\sqrt{\left(n_2^2 - k_2^2 - n_1^2\sin^2\theta\right)^2 + 4n_2^2k_2^2} + \left(n_2^2 - k_2^2 - n_1^2\sin^2\theta\right)\right] \tag{5.53}$$

$$q^2 = \frac{1}{2}\left[\sqrt{\left(n_2^2 - k_2^2 - n_1^2\sin^2\theta\right)^2 + 4n_2^2k_2^2} - \left(n_2^2 - k_2^2 - n_1^2\sin^2\theta\right)\right] \tag{5.54}$$

$$\rho_{\lambda,\perp} = \frac{\left(n_1\cos\theta - p\right)^2 + q^2}{\left(n_1\cos\theta + \mathrm{p}\right)^2 + q^2} \tag{5.55}$$

$$\rho_{\lambda,\parallel} = \frac{\left(p - n_1\sin\theta\tan\theta\right)^2 + q^2}{\left(p + n_1\sin\theta\tan\theta\right)^2 + q^2}\rho_{\lambda,\perp} \tag{5.56}$$

$$\rho'^{\cap}_{\lambda} = \frac{\rho_{\lambda,\parallel} + \rho_{\lambda,\perp}}{2} \tag{5.57}$$

The prime denotes a directional property with regard to incoming directions, while the superscript "$\cap$" denotes a hemispherical property with regard to outgoing directions. The subscript "λ" denotes a spectral quantity. No subscript is used to denote total quantities.

Reflectance, absorptance, and emittance

An effective spectral, directional-hemispherical reflectance of the surface is next determined. In models assuming EM, the Fresnel equations directly yield the effective spectral, directional-hemispherical reflectance from the effective complex refractive index.

$$\rho'^{\cap}_{\lambda,\mathrm{eff}} = f\left(n_{\lambda,\mathrm{eff}}, k_{\lambda,\mathrm{eff}}\right) \tag{5.58}$$

In models assuming ODM, the Fresnel equations yield spectral, directional–hemispherical reflectance for each component.

$$\rho'^{,\cap}_{\lambda,\mathrm{CaCO_3}} = f\left(n_{\lambda,\mathrm{CaCO_3}}, k_{\lambda,\mathrm{CaCO_3}}\right) \tag{5.59}$$

and similarly for calcium oxide and the fluid phase. The effective spectral, directional–hemispherical reflectance is calculated from these reflectance values in a similar manner as the effective refractive index was calculated.

$$\rho'^{,\cap}_{\lambda,\mathrm{eff}} = (1-\phi)\left[(1-X)\rho'^{,\cap}_{\lambda,\mathrm{CaCO_3}} + X\rho'^{,\cap}_{\lambda,\mathrm{CaO}}\right] + \phi\rho'^{,\cap}_{\lambda,\mathrm{f}} \tag{5.60}$$

Spectral, hemispherical reflectance ρ_λ is calculated from the effective spectral, directional–hemispherical reflectance by averaging the effective spectral, direction–hemispherical reflectance over all incoming directions to yield a property averaged over all incoming and outgoing directions. Assuming the incoming radiation is diffuse, the following equation is used to evaluate the spectral, hemispherical reflectance:

$$\rho_\lambda = \frac{1}{\pi}\int_{2\pi} \rho'^{,\cap}_{\lambda,\mathrm{eff}} \cos\theta_\mathrm{i} d\Omega_\mathrm{i} \tag{5.61}$$

where θ_i is the incoming radiation angle of incidence and Ω_i is the incoming radiation solid angle.

Values for total, hemispherical absorptance and emittance are evaluated from spectral, hemispherical reflectance by averaging the reflectance over the entire incident spectrum and emitted spectrum, respectively [39]. The incident spectrum modeled as the spectrum of a blackbody at 5777 K [44] to approximate solar radiation.

$$\alpha = \frac{\int_0^\infty (1-\rho_\lambda) E_{b\lambda} d\lambda}{\sigma T_\mathrm{sun}^4} \tag{5.62}$$

The emitted spectrum is taken to be the spectrum emitted by a blackbody at the particle surface temperature.

$$\varepsilon = \frac{\int_0^\infty (1-\rho_\lambda) E_{b\lambda} d\lambda}{\sigma T_\mathrm{surf}^4} \tag{5.63}$$

The indefinite integrals in Eqs. (5.62) and (5.63) are approximated using wavelength bands similar to the gray band approximation given by Eq. (5.37).

Chapter 6 Numerical methods

The four conservation of mass equations given by Eqs. (4.1), (4.2), (4.3), and (4.4), and the two conservation of energy equations given by Eqs. (5.1) and (5.2) with the two constraints of the equation of state, Eq. (4.15), and Darcy's law for of the conservation of momentum equation, Eq. (4.14), constitute the full mathematical model. The governing equations are solved numerically in 1D along the radius of the particle for the solid and gas phases. The equations are first discretized in space using the finite volume method and simplified to 1D, then discretized in time using the explicit Euler method. Boundary conditions simulating high-flux solar irradiation and a gas flow, reactor-like environment are applied. The domain is discretized into spherical shell volume elements with the same thickness, Δr. The discrete equations are solved using a FORTRAN 90 code developed for this application.

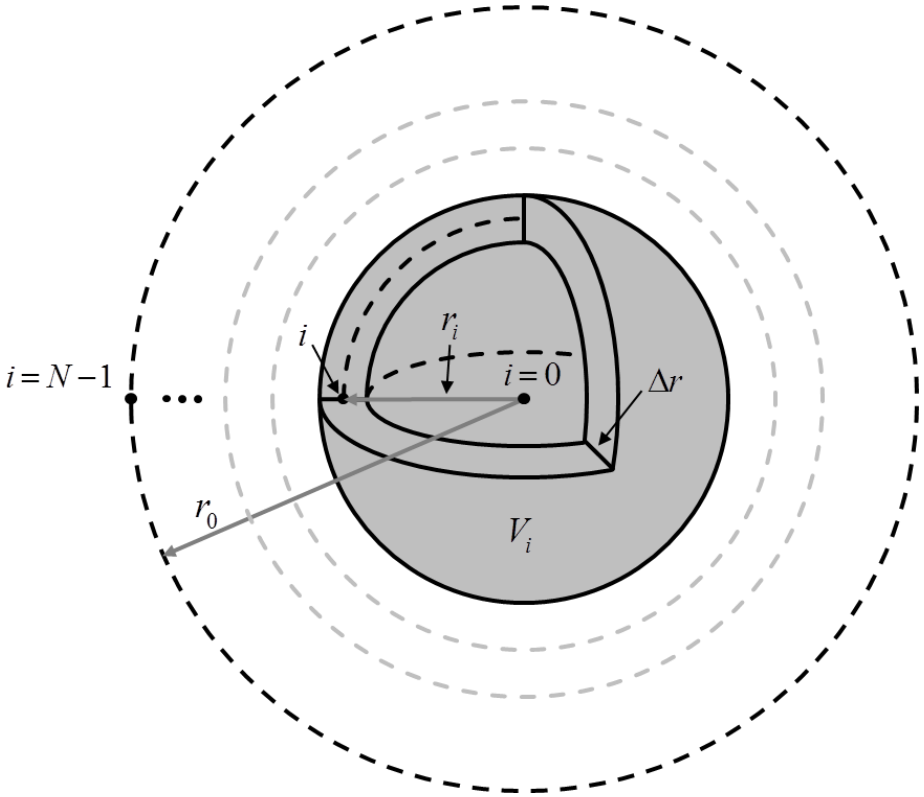

Figure 6.1 A discrete volume element within the particle

6.1 Discrete equations

The finite volume method is applied to the governing equations by integrating each equation over the volume of a single, spherical shell element. Parameters under the integral are approximated as constant throughout the element and are evaluated at the element center. A subscript is used to denote the discrete spatial element for which a quantity is evaluated. To illustrate the application of the finite volume method, the reaction rate for calcium carbonate integrated over the volume element is shown:

$$\int_{V_i} \left\langle r'''_{\mathrm{CaCO_3}} \right\rangle \mathrm{d}V = \left\langle r'''_{\mathrm{CaCO_3}} \right\rangle \Big|_i V_i \tag{6.1}$$

where $\left\langle r'''_{\mathrm{CaCO_3}} \right\rangle \Big|_i$ denotes the reaction rate in for the element V_i which is evaluated with conditions at the volume element center.

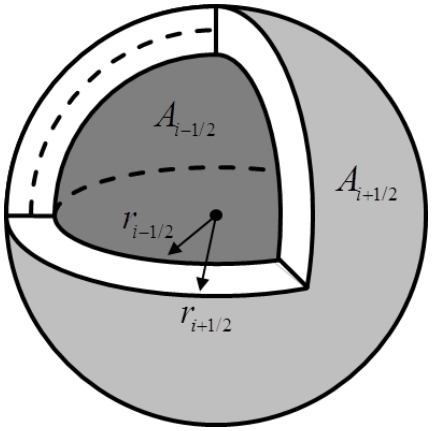

Figure 6.2 Volume element bounding surfaces and radii

Terms in the governing equations that contain the divergence operator are treated with the divergence theorem to transform volume integrals to surface integrals. For example, the advection term in the conservation of mass equation becomes

$$\int_{V_i} \nabla \cdot \left(\left\langle \bar{\rho}_{\mathrm{CO_2}} \right\rangle^{\mathrm{f}} \left\langle \mathbf{u}_{\mathrm{f}} \right\rangle \right) \mathrm{d}V_i = \int_{\delta V_i} \left\langle \bar{\rho}_{\mathrm{CO_2}} \right\rangle^{\mathrm{f}} \left\langle \mathbf{u}_{\mathrm{f}} \right\rangle \cdot \hat{\mathbf{n}} \mathrm{d}A \tag{6.2}$$

The surface over which the surface integral is evaluated consists of the positive and negative faces of the volume element shown in Figure 6.2. The outward facing normal is parallel to the radial axis and is positive for the element's positive face and negative for the element's negative face. The surface integral yields the flux at the positive and

negative faces of the element. The surface integral is evaluated at each face and yields from the example above

$$\int_{\delta V_i} \left\langle \bar{\rho}_{\mathrm{CO}_2} \right\rangle^{\mathrm{f}} \langle \mathbf{u}_{\mathrm{f}} \rangle \cdot \hat{\mathbf{n}} \mathrm{d}A = \left(\left\langle \bar{\rho}_{\mathrm{CO}_2} \right\rangle^{\mathrm{f}} u_{\mathrm{f}} \right)_{i+1/2} A_{i+1/2} - \left(\left\langle \bar{\rho}_{\mathrm{CO}_2} \right\rangle^{\mathrm{f}} u_{\mathrm{f}} \right)_{i+1/2} A_{i-1/2} \tag{6.3}$$

The flux is evaluated uniquely depending on the parameters involved. There are five types of divergence terms in the governing equations. These terms describe advective mass flux, diffusive mass flux, heat flux, advective enthalpy flux, and diffusive enthalpy flux. A description of how these fluxes are evaluated is in Table 6.1.

Table 6.1 Method of evaluating flux terms

Flux term	Parameter	Method of evaluation
$\nabla \cdot \left(\bar{\rho} \mathbf{u}_{\mathrm{f}} \right)$	$\bar{\rho}$	Upwinded based on the direction of $\mathbf{u}_{\mathrm{f}}$
	$\mathbf{u}_{\mathrm{f}}$	Evaluated at the element boundary
$\nabla \cdot \left(D \nabla \bar{\rho} \right)$	D	Averaged between neighboring elements, $D_{i+1/2} = \frac{D_i + D_{i+1}}{2}$
	$\nabla \bar{\rho}$	$\nabla \bar{\rho}_{i+1/2} = \frac{\bar{\rho}_{i+1} - \bar{\rho}_i}{\Delta r}$ where densities are evaluated at the element center
$\nabla \cdot \left(k \nabla T \right)$	k	Averaged by phase volume between neighboring elements, $k_{i+1/2} = \frac{k_i V_i + k_{i+1} V_{i+1}}{V_i + V_{i+1}}$
	∇T	$\nabla T_{i+1/2} = \frac{T_{i+1} - T_i}{\Delta r}$ where temperatures are evaluated at the element center
$\nabla \cdot \left(\bar{\rho} \bar{h} \mathbf{u}_{\mathrm{f}} \right)$	$\bar{\rho} \mathbf{u}_{\mathrm{f}}$	Same as above
	$\bar{h}$	Upwinded based on the direction of $\mathbf{u}_{\mathrm{f}}$
$\nabla \cdot \left(\bar{h} D \nabla \bar{\rho} \right)$	$D \nabla \bar{\rho}$	Same as above
	$\bar{h}$	Upwinded based on the direction of $\nabla \bar{\rho}$

After the equations are discretized in space, the explicit Euler method is applied to discretize the equations in time by integrating each equation over the time step Δt. All terms are evaluated at the current time level, with the exception of the time derivatives. A superscript is used to denote the time level at which a parameter is evaluated, *n* being the

current time level and n+1 the next time level. Conservation of mass time derivatives are evaluated as follows

$$\int_{\Delta t} \left.\frac{\partial \bar{\rho}}{\partial t}\right|_i \mathrm{d}t \approx \left(\frac{\bar{\rho}_i^{n+1} - \bar{\rho}_i^n}{\Delta t}\right)\Delta t = \bar{\rho}_i^{n+1} - \bar{\rho}_i^n \tag{6.4}$$

The conservation of energy time derivatives are first expanded, and then the time integrals are evaluated.

$$\frac{\partial\left(\bar{\rho}\bar{h}\right)}{\partial t} = \bar{\rho}\frac{\partial \bar{h}}{\partial t} + \bar{h}\frac{\partial \bar{\rho}}{\partial t} \tag{6.5}$$

The time derivative in the second term of the expansion is identical to the time derivative in the conservation of mass equations and evaluated identically. The time derivative in the first term is expanded using the definition of molar specific heat capacity.

$$\bar{c}_\mathrm{p} \overset{\mathrm{def}}{=} \left.\frac{\partial \bar{h}}{\partial T}\right|_{P=\text{constant}} \tag{6.6}$$

The definition of specific heat capacity can be rearranged to relate $\mathrm{d}\bar{h}$ to $\mathrm{d}T$ at a constant pressure.

$$\mathrm{d}\bar{h} = \bar{c}_\mathrm{p}\mathrm{d}T \tag{6.7}$$

This relation is used for both the solid and the fluid phases, even though the pressure in the fluid phase is not constant. Substituting Eq. (6.7) into Eq. (6.5) results in

$$\frac{\partial\left(\bar{\rho}\bar{h}\right)}{\partial t} = \bar{\rho}\bar{c}_\mathrm{p}\frac{\partial T}{\partial t} + \bar{h}\frac{\partial \bar{\rho}}{\partial t} \tag{6.8}$$

The temperature derivative is integrated over the time step in a similar manner as the density derivative.

$$\int_{\Delta t}\left(\bar{\rho}\bar{c}_\mathrm{p}\frac{\partial T}{\partial t}\right)_i \mathrm{d}t \approx \bar{\rho}_i^n \bar{c}_{\mathrm{p},i}^n \left(\frac{T_i^{n+1} - T_i^n}{\Delta t}\right)\Delta t = \bar{\rho}_i^n \bar{c}_{\mathrm{p},i}^n \left(T_i^{n+1} - T_i^n\right) \tag{6.9}$$

The entire energy time derivative then expands to

$$\int_{\Delta t}\frac{\partial\left(\bar{\rho}\bar{h}\right)}{\partial t}\mathrm{d}t \approx \bar{\rho}_i^n \bar{c}_{\mathrm{p},i}^n \left(T_i^{n+1} - T_i^n\right) + \bar{h}_i^n \left(\bar{\rho}_i^{n+1} - \bar{\rho}_i^n\right) \tag{6.10}$$

The ideal gas law equation of state contains no space or time derivatives so the evaluation is straightforward. The gradient in the conservation of momentum constraint is evaluated in the same manner as the gradients in Table 6.1.

Both the number of moles and the volume of each phase changes with time, so the molar density variables are expanded to be the number of moles, *N* over the phase volume. The number of moles and the porosity, which relates the phase volumes, are then solved for in time.

With the finite volume and explicit Euler methods applied as described above, the abbreviated discrete equations are:

- Calcium carbonate conservation of mass:

$$N_{\mathrm{CaCO_3},i}^{n+1} - N_{\mathrm{CaCO_3},i}^{n} = \left\langle r''' \right\rangle\Big|_i^n V_i \Delta t \tag{6.11}$$

- Calcium carbonate conservation of mass:

$$N_{\mathrm{CaO},i}^{n+1} - N_{\mathrm{CaO},i}^{n} = -\left\langle r''' \right\rangle\Big|_i^n V_i \Delta t \tag{6.12}$$

- Carbon dioxide conservation of mass:

$$\begin{aligned}
&\left(N_{\mathrm{CO_2},i}^{n+1} - N_{\mathrm{CO_2},i}^{n}\right) \\
&\quad + \left(\left\langle \bar{\rho}_{\mathrm{CO_2}} \right\rangle^{\mathrm{f}}\right)_{i+1/2}^{n} \left(u_{\mathrm{f}}\right)_{i+1/2}^{n} A_{i+1/2}\Delta t - \left(\left\langle \bar{\rho}_{\mathrm{CO_2}} \right\rangle^{\mathrm{f}}\right)_{i-1/2}^{n} \left(u_{\mathrm{f}}\right)_{i-1/2}^{n} A_{i-1/2}\Delta t \\
&\quad = \left(\frac{D_{\mathrm{CO_2},\mathrm{eff},i+1}^{n} + D_{\mathrm{CO_2},\mathrm{eff},i}^{n}}{2}\right) \frac{\left(\dfrac{N_{\mathrm{CO_2},i+1}^{n}}{\phi_{i+1}^{n} V_{i+1}}\right) - \left(\dfrac{N_{\mathrm{CO_2},i}^{n}}{\phi_{i}^{n} V_{i}}\right)}{\left(r_{i+1} - r_i\right)} A_{i+1/2}\Delta t \\
&\quad - \left(\frac{D_{\mathrm{CO_2},\mathrm{eff},i}^{n} + D_{\mathrm{CO_2},\mathrm{eff},i-1}^{n}}{2}\right) \frac{\left(\dfrac{N_{\mathrm{CO_2},i}^{n}}{\phi_{i}^{n} V_{i}}\right) - \left(\dfrac{N_{\mathrm{CO_2},i-1}^{n}}{\phi_{i-1}^{n} V_{i-1}}\right)}{\left(r_i - r_{i-1}\right)} A_{i-1/2}\Delta t \\
&\quad - \left\langle r''' \right\rangle\Big|_i^n V_i \Delta t
\end{aligned} \tag{6.13}$$

- Air conservation of mass:

$$\begin{aligned}
&\left(N_{\text{air},i}^{n+1}-N_{\text{air},i}^{n}\right)\\
&\quad+\left(\left\langle\bar{\rho}_{\text{air}}\right\rangle^{\text{f}}\right)_{i+1/2}^{n}\left(u_{\text{f}}\right)_{i+1/2}^{n}A_{i+1/2}\Delta t-\left(\left\langle\bar{\rho}_{\text{air}}\right\rangle^{\text{f}}\right)_{i-1/2}^{n}\left(u_{\text{f}}\right)_{i-1/2}^{n}A_{i-1/2}\Delta t\\
&\quad=\left(\frac{D_{\text{air,eff},i+1}^{n}+D_{\text{air,eff},i}^{n}}{2}\right)\frac{\left(\dfrac{N_{\text{air},i+1}^{n}}{\phi_{i+1}^{n}V_{i+1}}\right)-\left(\dfrac{N_{\text{air},i}^{n}}{\phi_{i}^{n}V_{i}}\right)}{\left(r_{i+1}-r_{i}\right)}A_{i+1/2}\Delta t\\
&\quad-\left(\frac{D_{\text{air,eff},i}^{n}+D_{\text{air,eff},i-1}^{n}}{2}\right)\frac{\left(\dfrac{N_{\text{air},i}^{n}}{\phi_{i}^{n}V_{i}}\right)-\left(\dfrac{N_{\text{air},i-1}^{n}}{\phi_{i-1}^{n}V_{i-1}}\right)}{\left(r_{i}-r_{i-1}\right)}A_{i-1/2}\Delta t
\end{aligned}\tag{6.14}$$

- Solid phase conservation of energy:

$$\begin{aligned}
&\left(N_{\text{CaCO}_3,i}^{n}\bar{c}_{\text{p,CaCO}_3,i}^{n}+N_{\text{CaO},i}^{n}\bar{c}_{\text{p,CaO},i}^{n}\right)\left(\left\langle T_{\text{s}}\right\rangle_{i}^{\text{s},n+1}-\left\langle T_{\text{s}}\right\rangle_{i}^{\text{s},n}\right)\\
&\quad=\left[\frac{k_{\text{s,eff},i+1}^{n}\left(1-\phi_{i+1}^{n}\right)V_{i+1}+k_{\text{s,eff},i}^{n}\left(1-\phi_{i}^{n}\right)V_{i}}{\left(1-\phi_{i+1}^{n}\right)V_{i+1}+\left(1-\phi_{i}^{n}\right)V_{i}}\right]\left(\frac{\left\langle T_{\text{s}}\right\rangle_{i+1}^{\text{s},n}-\left\langle T_{\text{s}}\right\rangle_{i}^{\text{s},n}}{r_{i+1}-r_{i}}\right)A_{i+1/2}\Delta t\\
&\quad-\left[\frac{k_{\text{s,eff},i}^{n}\left(1-\phi_{i}^{n}\right)V_{i}+k_{\text{s,eff},i-1}^{n}\left(1-\phi_{i-1}^{n}\right)V_{i-1}}{\left(1-\phi_{i}^{n}\right)V_{i}+\left(1-\phi_{i-1}^{n}\right)V_{i-1}}\right]\left(\frac{\left\langle T_{\text{s}}\right\rangle_{i}^{\text{s},n}-\left\langle T_{\text{s}}\right\rangle_{i-1}^{\text{s},n}}{r_{i}-r_{i-1}}\right)A_{i-1/2}\Delta t
\end{aligned}\tag{6.15}$$

- Fluid phase conservation of energy:

$$
\begin{aligned}
&\left(N^n_{\mathrm{CO_2},i}\bar{c}^n_{\mathrm{p,CO_2},i}+N^n_{\mathrm{air},i}\bar{c}^n_{\mathrm{p,air},i}\right)\left(\left\langle T_\mathrm{f}\right\rangle_i^{\mathrm{f},n+1}-\left\langle T_\mathrm{f}\right\rangle_i^{\mathrm{f},n}\right)\\
&\quad+\bar{h}^n_{\mathrm{CO_2},i}\left(N^{n+1}_{\mathrm{CO_2},i}-N^n_{\mathrm{CO_2},i}\right)+\bar{h}^n_{\mathrm{air},i}\left(N^{n+1}_{\mathrm{air},i}-N^n_{\mathrm{air},i}\right)\\
&\quad=\bar{h}^n_{\mathrm{CO_2},i+1/2}\left(\left\langle\bar{\rho}_{\mathrm{CO_2}}\right\rangle^{\mathrm{f}}u_\mathrm{f}\right)^n_{i+1/2}A_{i+1/2}\Delta t-\bar{h}^n_{\mathrm{CO_2},i-1/2}\left(\left\langle\bar{\rho}_{\mathrm{CO_2}}\right\rangle^{\mathrm{f}}u_\mathrm{f}\right)^n_{i-1/2}A_{i-1/2}\Delta t\\
&\quad+\bar{h}^n_{\mathrm{CO_2},i+1/2}\left(D_{\mathrm{CO_2,eff}}\nabla\left\langle\bar{\rho}_{\mathrm{CO_2}}\right\rangle^{\mathrm{f}}\right)^n_{i+1/2}A_{i+1/2}\Delta t\\
&\quad-\bar{h}^n_{\mathrm{CO_2},i-1/2}\left(D_{\mathrm{CO_2,eff}}\nabla\left\langle\bar{\rho}_{\mathrm{CO_2}}\right\rangle^{\mathrm{f}}\right)^n_{i-1/2}A_{i-1/2}\Delta t\\
&\quad+\bar{h}^n_{\mathrm{air},i+1/2}\left(\left\langle\bar{\rho}_{\mathrm{air}}\right\rangle^{\mathrm{f}}u_\mathrm{f}\right)^n_{i+1/2}A_{i+1/2}\Delta t-\bar{h}^n_{\mathrm{air},i-1/2}\left(\left\langle\bar{\rho}_{\mathrm{air}}\right\rangle^{\mathrm{f}}u_\mathrm{f}\right)^n_{i-1/2}A_{i-1/2}\Delta t\\
&\quad+\bar{h}^n_{\mathrm{air},i+1/2}\left(D_{\mathrm{air,eff}}\nabla\left\langle\bar{\rho}_{\mathrm{air}}\right\rangle^{\mathrm{f}}\right)^n_{i+1/2}A_{i+1/2}\Delta t\\
&\quad+\bar{h}^n_{\mathrm{air},i-1/2}\left(D_{\mathrm{air,eff}}\nabla\left\langle\bar{\rho}_{\mathrm{air}}\right\rangle^{\mathrm{f}}\right)^n_{i-1/2}A_{i-1/2}\Delta t\\
&\quad+\left(\frac{k^n_{\mathrm{f,eff},i+1}\phi^n_{i+1}V_{i+1}+k^n_{\mathrm{f,eff},i}\phi^n_iV_i}{\phi^n_{i+1}V_{i+1}+\phi^n_iV_i}\right)\left(\frac{\left\langle T_\mathrm{f}\right\rangle^{\mathrm{f},n}_{i+1}-\left\langle T_\mathrm{f}\right\rangle^{\mathrm{f},n}_i}{r_{i+1}-r_i}\right)A_{i+1/2}\Delta t\\
&\quad-\left(\frac{k^n_{\mathrm{f,eff},i}\phi^n_iV_i+k^n_{\mathrm{f,eff},i-1}\phi^n_{i-1}V_{i-1}}{\phi^n_iV_i+\phi^n_{i-1}V_{i-1}}\right)\left(\frac{\left\langle T_\mathrm{f}\right\rangle^{\mathrm{f},n}_i-\left\langle T_\mathrm{f}\right\rangle^{\mathrm{f},n}_{i-1}}{r_i-r_{i-1}}\right)A_{i-1/2}\Delta t
\end{aligned}
\tag{6.16}
$$

- Equation of state:

$$
\left\langle p_\mathrm{f}\right\rangle_i^{\mathrm{f},n}=\left(\frac{N^n_{\mathrm{CO_2},i}+N^n_{\mathrm{air},i}}{\phi^n_iV_i}\right)\bar{R}\left\langle T_\mathrm{f}\right\rangle_i^{\mathrm{f},n}
\tag{6.17}
$$

- Fluid phase conservation of momentum:

$$
\frac{\left\langle p_\mathrm{f}\right\rangle^{\mathrm{f},n}_{i+1}-\left\langle p_\mathrm{f}\right\rangle^{\mathrm{f},n}_i}{\Delta r}=\frac{\mu^n_i}{K^n_i}u^n_{\mathrm{f},i+1/2}
\tag{6.18}
$$

The evaluation of upwinded, fluid molar density terms and fluid enthalpies are given in Table 6.2, Table 6.3, and Table 6.4.

Table 6.2 Evaluation of upwinded molar density terms in fluid conservation of mass discrete equations

Variable evaluation	Variable evaluation	Condition
$\left(\left\langle \bar{\rho}_{\mathrm{CO_2}} \right\rangle^{\mathrm{f}}\right)^{n}_{i+1/2} = \dfrac{N^{n}_{\mathrm{CO_2},i+1}}{\phi^{n}_{i+1} V_{i+1}}$	$\left(\left\langle \bar{\rho}_{\mathrm{air}} \right\rangle^{\mathrm{f}}\right)^{n}_{i+1/2} = \dfrac{N^{n}_{\mathrm{air},i+1}}{\phi^{n}_{i+1} V_{i+1}}$	$\left(u_{\mathrm{f}}\right)^{n}_{i+1/2} > 0$
$\left(\left\langle \bar{\rho}_{\mathrm{CO_2}} \right\rangle^{\mathrm{f}}\right)^{n}_{i+1/2} = \dfrac{N^{n}_{\mathrm{CO_2},i}}{\phi^{n}_{i} V_{i}}$	$\left(\left\langle \bar{\rho}_{\mathrm{air}} \right\rangle^{\mathrm{f}}\right)^{n}_{i+1/2} = \dfrac{N^{n}_{\mathrm{air},i}}{\phi^{n}_{i} V_{i}}$	$\left(u_{\mathrm{f}}\right)^{n}_{i+1/2} \le 0$
$\left(\left\langle \bar{\rho}_{\mathrm{CO_2}} \right\rangle^{\mathrm{f}}\right)^{n}_{i-1/2} = \dfrac{N^{n}_{\mathrm{CO_2},i}}{\phi^{n}_{i} V_{i}}$	$\left(\left\langle \bar{\rho}_{\mathrm{air}} \right\rangle^{\mathrm{f}}\right)^{n}_{i-1/2} = \dfrac{N^{n}_{\mathrm{air},i}}{\phi^{n}_{i} V_{i}}$	$\left(u_{\mathrm{f}}\right)^{n}_{i-1/2} > 0$
$\left(\left\langle \bar{\rho}_{\mathrm{CO_2}} \right\rangle^{\mathrm{f}}\right)^{n}_{i-1/2} = \dfrac{N^{n}_{\mathrm{CO_2},i-1}}{\phi^{n}_{i-1} V_{i-1}}$	$\left(\left\langle \bar{\rho}_{\mathrm{air}} \right\rangle^{\mathrm{f}}\right)^{n}_{i-1/2} = \dfrac{N^{n}_{\mathrm{air},i-1}}{\phi^{n}_{i-1} V_{i-1}}$	$\left(u_{\mathrm{f}}\right)^{n}_{i-1/2} \le 0$

Table 6.3 Upwinded evaluation of enthalpy transport due to advection in fluid conservation of energy discrete equation

Variable evaluation	Variable evaluation	Condition
$\bar{h}^{n}_{\mathrm{CO_2},i+1/2} = \bar{h}^{n}_{\mathrm{CO_2},i}$	$\bar{h}^{n}_{\mathrm{air},i+1/2} = \bar{h}^{n}_{\mathrm{air},i}$	$\left(u_{\mathrm{f}}\right)^{n}_{i+1/2} > 0$
$\bar{h}^{n}_{\mathrm{CO_2},i+1/2} = \bar{h}^{n}_{\mathrm{CO_2},i+1}$	$\bar{h}^{n}_{\mathrm{air},i+1/2} = \bar{h}^{n}_{\mathrm{air},i+1}$	$\left(u_{\mathrm{f}}\right)^{n}_{i+1/2} \le 0$
$\bar{h}^{n}_{\mathrm{CO_2},i-1/2} = \bar{h}^{n}_{\mathrm{CO_2},i-1}$	$\bar{h}^{n}_{\mathrm{air},i-1/2} = \bar{h}^{n}_{\mathrm{air},i-1}$	$\left(u_{\mathrm{f}}\right)^{n}_{i-1/2} > 0$
$\bar{h}^{n}_{\mathrm{CO_2},i-1/2} = \bar{h}^{n}_{\mathrm{CO_2},i}$	$\bar{h}^{n}_{\mathrm{air},i-1/2} = \bar{h}^{n}_{\mathrm{air},i}$	$\left(u_{\mathrm{f}}\right)^{n}_{i-1/2} \le 0$

Table 6.4 Upwinded evaluation of enthalpy transport due to diffusion in fluid conservation of energy discrete equation

Variable evaluation	Condition	Variable evaluation	Condition
$\bar{h}^{n}_{\mathrm{CO_2},i+1/2} = \bar{h}^{n}_{\mathrm{CO_2},i+1}$	$\left(\nabla\left\langle \bar{\rho}_{\mathrm{CO_2}} \right\rangle^{\mathrm{f}}\right)^{n}_{i+1/2} > 0$	$\bar{h}^{n}_{\mathrm{air},i+1/2} = \bar{h}^{n}_{\mathrm{air},i+1}$	$\left(\nabla\left\langle \bar{\rho}_{\mathrm{air}} \right\rangle^{\mathrm{f}}\right)^{n}_{i+1/2} > 0$
$\bar{h}^{n}_{\mathrm{CO_2},i+1/2} = \bar{h}^{n}_{\mathrm{CO_2},i}$	$\left(\nabla\left\langle \bar{\rho}_{\mathrm{CO_2}} \right\rangle^{\mathrm{f}}\right)^{n}_{i+1/2} \le 0$	$\bar{h}^{n}_{\mathrm{air},i+1/2} = \bar{h}^{n}_{\mathrm{air},i}$	$\left(\nabla\left\langle \bar{\rho}_{\mathrm{air}} \right\rangle^{\mathrm{f}}\right)^{n}_{i+1/2} \le 0$
$\bar{h}^{n}_{\mathrm{CO_2},i-1/2} = \bar{h}^{n}_{\mathrm{CO_2},i}$	$\left(\nabla\left\langle \bar{\rho}_{\mathrm{CO_2}} \right\rangle^{\mathrm{f}}\right)^{n}_{i-1/2} > 0$	$\bar{h}^{n}_{\mathrm{air},i-1/2} = \bar{h}^{n}_{\mathrm{air},i}$	$\left(\nabla\left\langle \bar{\rho}_{\mathrm{air}} \right\rangle^{\mathrm{f}}\right)^{n}_{i-1/2} > 0$
$\bar{h}^{n}_{\mathrm{CO_2},i-1/2} = \bar{h}^{n}_{\mathrm{CO_2},i-1}$	$\left(\nabla\left\langle \bar{\rho}_{\mathrm{CO_2}} \right\rangle^{\mathrm{f}}\right)^{n}_{i-1/2} \le 0$	$\bar{h}^{n}_{\mathrm{air},i-1/2} = \bar{h}^{n}_{\mathrm{air},i-1}$	$\left(\nabla\left\langle \bar{\rho}_{\mathrm{air}} \right\rangle^{\mathrm{f}}\right)^{n}_{i-1/2} \le 0$

6.2 Boundary and initial conditions

Two boundary conditions—one at the particle surface and one at the particle center—are required for the six conservation equations. The solid phase species do not move in space so the fluxes at the center and surface are zero. The mass flux at the center of the particle for all species is zero due to symmetry:

$$\left.\frac{\partial \left\langle \bar{\rho}_{\mathrm{CaCO_3}} \right\rangle^{\mathrm{s}}}{\partial r}\right|_{r=0} = \left.\frac{\partial \left\langle \bar{\rho}_{\mathrm{CaCO_3}} \right\rangle^{\mathrm{s}}}{\partial r}\right|_{r=r_0} = 0 \tag{6.19}$$

$$\left.\frac{\partial \left\langle \bar{\rho}_{\mathrm{CaO}} \right\rangle^{\mathrm{s}}}{\partial r}\right|_{r=0} = \left.\frac{\partial \left\langle \bar{\rho}_{\mathrm{CaO}} \right\rangle^{\mathrm{s}}}{\partial r}\right|_{r=r_0} = 0 \tag{6.20}$$

$$\left.\frac{\partial \left\langle \bar{\rho}_{\mathrm{CO_2}} \right\rangle^{\mathrm{f}}}{\partial r}\right|_{r=0} = 0 \tag{6.21}$$

$$\left[\left\langle \bar{\rho}_{\mathrm{CO_2}} \right\rangle^{\mathrm{f}} u_{\mathrm{f}} - D_{\mathrm{CO_2,eff}} \frac{\partial \left\langle \bar{\rho}_{\mathrm{CO_2}} \right\rangle^{\mathrm{f}}}{\partial r}\right]_{r=r_0} = h_{\mathrm{mass,eff}} \left(\left\langle \bar{\rho}_{\mathrm{CO_2}} \right\rangle^{\mathrm{f}}\Big|_{r=r_0} - \bar{\rho}_{\infty,\mathrm{CO_2}} \right) \tag{6.22}$$

$$\left.\frac{\partial \left\langle \bar{\rho}_{\mathrm{air}} \right\rangle^{\mathrm{f}}}{\partial r}\right|_{r=0} = 0 \tag{6.23}$$

$$\left[\left\langle \bar{\rho}_{\mathrm{air}} \right\rangle^{\mathrm{f}} u_{\mathrm{f}} - D_{\mathrm{air,eff}} \frac{\partial \left\langle \bar{\rho}_{\mathrm{air}} \right\rangle^{\mathrm{f}}}{\partial r}\right]_{r=r_0} = h_{\mathrm{mass,eff}} \left(\left\langle \bar{\rho}_{\mathrm{air}} \right\rangle^{\mathrm{f}}\Big|_{r=r_0} - \bar{\rho}_{\infty,\mathrm{air}} \right) \tag{6.24}$$

For the fluid species, the boundary condition at the surface is a mixed condition. It is defined by advection and diffusion at the particle surface and convective mass transfer away from the particle surface. In Eqs. (6.22) and (6.24), the first term on the left hand side is due to advection and the second term is due to diffusion. These terms together must balance the convective mass transfer term on the right hand side of the equation. The molar densities of the free stream gas species ($\bar{\rho}_{\infty,\mathrm{CO_2}}$ and $\bar{\rho}_{\infty,\mathrm{air}}$) are calculated by the ideal gas law from the total pressure p_0, free stream temperature T_∞, and free stream carbon dioxide concentration $\bar{y}_{\infty,\mathrm{CO_2}}$:

$$\bar{\rho}_{\infty,\mathrm{CO_2}} = \bar{y}_{\infty,\mathrm{CO_2}} \frac{p_0}{\bar{R}T_\infty} \tag{6.25}$$

$$\bar{\rho}_{\infty,\mathrm{air}} = \left(1 - \bar{y}_{\infty,\mathrm{CO_2}}\right) \frac{p_0}{\bar{R}T_\infty} \tag{6.26}$$

For the conservation of energy equations, the boundary conditions at the center of the particle are zero by symmetry. The solid phase surface boundary condition is a mixed condition. The left hand side of Eq. (6.28) is the sum of the conductive and radiative heat fluxes at the surface. The first term of the right hand side is due to convective heat transfer. The second and third terms are absorbed incident radiation and emitted radiation, respectively.

$$\left.\frac{\partial \langle T_\mathrm{s} \rangle^\mathrm{s}}{\partial r}\right|_{r=0} = 0 \tag{6.27}$$

$$\left(k_{\mathrm{s,eff}} + k_{\mathrm{rad,eff}}\right) \left.\frac{\partial \langle T_\mathrm{s} \rangle^\mathrm{s}}{\partial r}\right|_{r=r_0} = h_{\mathrm{s,eff}} \left(T_\infty - \left.\langle T_\mathrm{s} \rangle^\mathrm{s}\right|_{r=r_0}\right) + \alpha_{\mathrm{eff}} q''_{\mathrm{solar}} - \varepsilon_{\mathrm{eff}} \sigma \left[\left(\left.\langle T_\mathrm{s} \rangle^\mathrm{s}\right|_{r=r_0}\right)^4 - T_\mathrm{w}^4\right] \tag{6.28}$$

The fluid phase surface boundary condition for the energy equation, Eq. (6.30) below, is also mixed, but only contains terms for conduction at the surface and convective heat transfer with the free stream.

$$\left.\frac{\partial \langle T_\mathrm{f} \rangle^\mathrm{f}}{\partial r}\right|_{r=0} = 0 \tag{6.29}$$

$$k_{\mathrm{f,eff}} \left.\frac{\partial \langle T_\mathrm{f} \rangle^\mathrm{f}}{\partial r}\right|_{r=r_0} = h_{\mathrm{f,eff}} \left(T_\infty - \left.\langle T_\mathrm{f} \rangle^\mathrm{f}\right|_{r=r_0}\right) \tag{6.30}$$

Initially conditions for the particle are as follows. The initial number of moles in each volume element of calcium carbonate is calculated based on the element volume V_i, the initial porosity, the mass density of solid calcium carbonate, and the molar mass. The initial number of moles of calcium oxide at all locations is zero.

$$\left.\bar{\rho}_{\mathrm{CaCO_3}}\right|_i^{t=t_0} = \frac{\left.N_{\mathrm{CaCO_3}}\right|_i^{t=t_0}}{\left(1-\phi_{0,\mathrm{CaCo_3}}\right)V|_i} = \frac{\rho_{\mathrm{CaCO_3}}}{M_{\mathrm{CaCO_3}}} \tag{6.31}$$

$$\bar{\rho}_{\mathrm{CaO}}\Big|_i^{t=t_0} = \frac{N_{\mathrm{CaO}}\Big|_i^{t=t_0}}{\left(1-\phi_{0,\mathrm{CaCO_3}}\right)V\Big|_i} = 0 \tag{6.32}$$

The initial molar densities of the fluid species inside the particle pore space are the same as the respective free stream molar densities. The initial number of moles of each species is calculated using the free stream molar density, the initial porosity, and the element volume.

$$\bar{\rho}_{\mathrm{CO_2}}\Big|_i^{t=t_0} = \frac{N_{\mathrm{CO_2}}\Big|_i^{t=t_0}}{\phi_{0,\mathrm{CaCO_3}}\,V\Big|_i} = \bar{\rho}_{\infty,\mathrm{CO_2}} \tag{6.33}$$

$$\bar{\rho}_{\mathrm{air}}\Big|_i^{t=t_0} = \frac{N_{\mathrm{air}}\Big|_i^{t=t_0}}{\phi_{0,\mathrm{CaCO_3}}\,V\Big|_i} = \bar{\rho}_{\infty,\mathrm{air}} \tag{6.34}$$

Initially the solid and fluid phases are isothermal at an initial temperature T_0.

$$\left\langle T_{\mathrm{s}}\right\rangle^{\mathrm{s}}\Big|_i^{t=t_0} = T_0 \tag{6.35}$$

$$\left\langle T_{\mathrm{f}}\right\rangle^{\mathrm{f}}\Big|_i^{t=t_0} = T_0 \tag{6.36}$$

6.3 Implementation

The domain is discretized into volume elements by defining Δr based on the particle radius and the number of volume elements being used for the simulation *N*,

$$\Delta r = \frac{r_0}{N} \tag{6.37}$$

The elements are indexed starting with zero and progressing to $N-1$. Parameters for the element are evaluated at the element node, located in the center of the element at r_i. The node location and element volume are defined by the following equations

$$r_i = \Delta r\left(i+0.5\right) \tag{6.38}$$

$$V_i = \frac{4}{3}\pi\left[\left(r_i+\frac{\Delta r}{2}\right)^3-\left(r_i-\frac{\Delta r}{2}\right)^3\right] \tag{6.39}$$

The positive face of a volume element has surface area defined by

$$A_{i+1/2} = 4\pi\left(r_i + \frac{\Delta r}{2}\right)^2 \tag{6.40}$$

and similarly for the negative face.

The program structure is outlined in Figure 6.3. Conditions for the simulation, properties that to not change throughout the simulation, and the mesh are first set. The simulation progresses in time and at each time step, temperature and composition dependent parameters are evaluated, the conservation of mass discrete equations are solved, and then the conservation of energy discrete equations are solved. Data is written to file and the simulation stops when the specified amount of time has been reached.

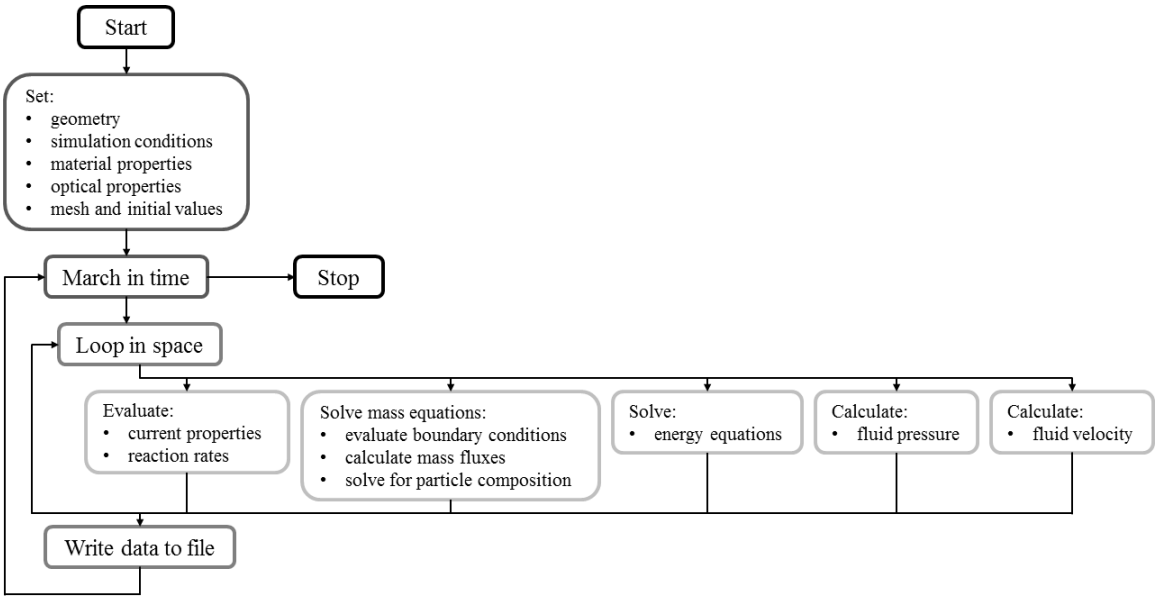

Figure 6.3 Program structure and order of operations

The code is written in FORTRAN 90 using the Geany text editor. It is compiled with the Intel FORTRAN compiler, ifort.

6.4 Stability

Due to the complexity of the governing equations and the multiple physical phenomena occurring in the simulation, a rigorous sensitivity analysis has not been completed. The primary mode of analysis has been trial and error for identifying stable simulation parameters.

Physical components of the model were programmed sequentially and tested as they were implemented. Unfortunately, initial iterations of the full model were very sensitive and required a time step as small as 1×10^{-11} s for stability. This time step was prohibitively small and would have prevented the model from producing meaningful results.

An analysis of the time scales of different physical processes was performed. The results of the analysis found interphase heat transfer occurred on a time scale of 10^{-11} s. It was concluded that the LTNE functionality of the program was the component requiring a very small time step. Possible avenues were considered for how to proceed, and it was decided to simplify the model by assuming local thermal equilibrium (LTE).

For LTE, the two governing equations for conservation of energy are added together, and the temperatures of each phase are assumed equal. The resulting governing equation is:

$$\begin{aligned}\frac{\partial\left(\langle\bar{\rho}\rangle\langle\bar{h}\rangle\right)}{\partial t}+\nabla\cdot\left(\langle\bar{\rho}_{\mathrm{f}}\rangle^{\mathrm{f}}\langle\bar{h}_{\mathrm{f}}\rangle^{\mathrm{f}}\langle\mathbf{u}_{\mathrm{f}}\rangle\right)&=\nabla\cdot\left(\langle\bar{h}_{\mathrm{CO_2}}\rangle^{\mathrm{f}}D_{\mathrm{CO_2,eff}}\nabla\langle\bar{\rho}_{\mathrm{CO_2}}\rangle^{\mathrm{f}}\right)\\&+\nabla\cdot\left(\langle\bar{h}_{\mathrm{air}}\rangle^{\mathrm{f}}D_{\mathrm{air,eff}}\nabla\langle\bar{\rho}_{\mathrm{air}}\rangle^{\mathrm{f}}\right)+\nabla\cdot\left(k_{\mathrm{eff}}\nabla\langle T\rangle\right)-\langle\nabla\cdot\mathbf{q}''_{\mathrm{rad}}\rangle\end{aligned}\tag{6.41}$$

The terms for the interphase heat transfer terms and the enthalpy flux across the solid–fluid interface cancel. A total effective conductivity is used in the LTE conservation of energy equation and is a combination of the effective conductivities of the two phases:

$$k_{\mathrm{eff}}=k_{\mathrm{s,eff}}+k_{\mathrm{f,eff}}\tag{6.42}$$

The discrete equation is:

$$
\begin{aligned}
&\left(N^n_{\mathrm{CaCO_3},i}\bar{c}^n_{\mathrm{p,CaCO_3},i}+N^n_{\mathrm{CaO},i}\bar{c}^n_{\mathrm{p,CaO},i}+N^n_{\mathrm{CO_2},i}\bar{c}^n_{\mathrm{p,CO_2},i}+N^n_{\mathrm{air},i}\bar{c}^n_{\mathrm{p,air},i}\right)\left(\langle T\rangle^{n+1}_i-\langle T\rangle^n_i\right)\\
&\quad+\bar{h}^n_{\mathrm{CaCO_3},i}\left(N^{n+1}_{\mathrm{CaCO_3},i}-N^n_{\mathrm{CaCO_3},i}\right)+\bar{h}^n_{\mathrm{CaO},i}\left(N^{n+1}_{\mathrm{CaO},i}-N^n_{\mathrm{CaO},i}\right)\\
&\quad+\bar{h}^n_{\mathrm{CO_2},i}\left(N^{n+1}_{\mathrm{CO_2},i}-N^n_{\mathrm{CO_2},i}\right)+\bar{h}^n_{\mathrm{air},i}\left(N^{n+1}_{\mathrm{air},i}-N^n_{\mathrm{air},i}\right)\\
&\quad=\bar{h}^n_{\mathrm{CO_2},i+1/2}\left(\left\langle\bar{\rho}_{\mathrm{CO_2}}\right\rangle^{\mathrm{f}}u_{\mathrm{f}}\right)^n_{i+1/2}A_{i+1/2}\Delta t-\bar{h}^n_{\mathrm{CO_2},i-1/2}\left(\left\langle\bar{\rho}_{\mathrm{CO_2}}\right\rangle^{\mathrm{f}}u_{\mathrm{f}}\right)^n_{i-1/2}A_{i-1/2}\Delta t\\
&\quad+\bar{h}^n_{\mathrm{CO_2},i+1/2}\left(D_{\mathrm{CO_2,eff}}\nabla\left\langle\bar{\rho}_{\mathrm{CO_2}}\right\rangle^{\mathrm{f}}\right)^n_{i+1/2}A_{i+1/2}\Delta t\\
&\quad-\bar{h}^n_{\mathrm{CO_2},i-1/2}\left(D_{\mathrm{CO_2,eff}}\nabla\left\langle\bar{\rho}_{\mathrm{CO_2}}\right\rangle^{\mathrm{f}}\right)^n_{i-1/2}A_{i-1/2}\Delta t\\
&\quad+\bar{h}^n_{\mathrm{air},i+1/2}\left(\left\langle\bar{\rho}_{\mathrm{air}}\right\rangle^{\mathrm{f}}u_{\mathrm{f}}\right)^n_{i+1/2}A_{i+1/2}\Delta t-\bar{h}^n_{\mathrm{air},i-1/2}\left(\left\langle\bar{\rho}_{\mathrm{air}}\right\rangle^{\mathrm{f}}u_{\mathrm{f}}\right)^n_{i-1/2}A_{i-1/2}\Delta t\\
&\quad+\bar{h}^n_{\mathrm{air},i+1/2}\left(D_{\mathrm{air,eff}}\nabla\left\langle\bar{\rho}_{\mathrm{air}}\right\rangle^{\mathrm{f}}\right)^n_{i+1/2}A_{i+1/2}\Delta t\\
&\quad+\bar{h}^n_{\mathrm{air},i-1/2}\left(D_{\mathrm{air,eff}}\nabla\left\langle\bar{\rho}_{\mathrm{air}}\right\rangle^{\mathrm{f}}\right)^n_{i-1/2}A_{i-1/2}\Delta t\\
&\quad+\left(\frac{k^n_{\mathrm{eff},i+1}V_{i+1}+k^n_{\mathrm{eff},i}V_i}{V_{i+1}+V_i}\right)\left(\frac{\langle T\rangle^n_{i+1}-\langle T\rangle^n_i}{r_{i+1}-r_i}\right)A_{i+1/2}\Delta t\\
&\quad-\left(\frac{k^n_{\mathrm{eff},i+1}V_i+k^n_{\mathrm{eff},i}V_{i-1}}{V_i+V_{i-1}}\right)\left(\frac{\langle T\rangle^n_i-\langle T\rangle^n_{i-1}}{r_i-r_{i-1}}\right)A_{i-1/2}\Delta t
\end{aligned}
\tag{6.43}
$$

The upwinding schemes for the LTE discrete energy equation are the same as those used in the LTNE discrete equations above. Adjustments were made to the simulation to reflect the LTE assumption, and the required time step for stability was found to be acceptably large to produce meaningful results. The results presented in the following chapter utilize the modified, LTE model.

Chapter 7 Results

Results of the model are presented. Heating of the solid phase is first investigated. The solar flux boundary condition is then cycled on and off to show particle heating and cooling in response to the boundary condition. Previously published simulation results of fixed–pressure heat transfer with chemical kinetics are reproduced. The full model containing heat transfer, mass transfer, and chemical kinetics is implemented and used to investigate the influence of incident irradiation, particle size, and ambient carbon dioxide concentration. A sensitivity analysis of the following parameters is presented: reaction rate, surface radiative properties, diffusivity, permeability, and internal radiative heat transfer.

Baseline parameters for the simulation are selected for continuity and comparison with past work and to simulate potential reactor-like conditions. The parameters are given in Table 7.1.

Table 7.1 Parameters used in the baseline simulation

Parameter	Value	Units
$\overline{y}_{\infty,\mathrm{CO_2}}$	0.99	
N	30	
p_0	101,325	Pa
q''_{solar}	1	MW m^{-2}
r_0	0.0025	m
Δt	5×10^{-6}	s
T_0	300	K
T_w	300	K
ε_w	1	
T_∞	300	K
u_∞	0.09	m s^{-1}

The ambient total pressure p_0, particle size r_0, and free stream fluid velocity u_∞ are taken to match simulation conditions in [19] and [21]. The ambient carbon dioxide concentration is selected to simulate calcination as part of a carbon dioxide capturing

cycle, where the carbon dioxide is released by the particle into a stream of nearly pure CO_2. 99% purity is the industrial standard for the food and beverage industry and medical industry. DM1 for diffusion is used as the baseline diffusion model. Model 4 as described in Table 5.3 for surface radiative properties is used as the baseline surface radiative properties model.

7.1 Particle heating—conduction vs. conduction with radiation

Solid phase heating and the effect of internal radiative heat transfer are investigated. Fluid conductivity, heat capacitance, and mass transfer within the particle are neglected in this section. Chemical kinetics are also neglected. The boundary conditions remain the same. Three isotropic, particle compositions are considered: unreacted calcium carbonate, completely reacted calcium oxide, and a mixture of half calcium carbonate and half calcium oxide.

Results of the simulation are shown below. Temperature is shown for selected locations as a function of time in Figure 7.1. After 40 s of simulation time, the calcium carbonate particle reaches the temperature 2058 K with a difference of 0.02 K throughout the particle; the 50% mixture particle reaches 2052 K with a difference of 0.03 K; and the calcium oxide particle reaches 2050 K with a difference of 0.12 K.

Figure 7.2 shows temperature gradients within the particle for calcium carbonate and calcium oxide for selected times. The temperature gradients within the calcium oxide particle are greater than those within the calcium carbonate particle. This indicates the center of the calcium carbonate particle heats up faster than the center of the calcium oxide particle. However, the surface temperature of calcium oxide heats up faster than the surface temperature of calcium carbonate. The higher temperature gradient in the calcium oxide particle is due to decreased conduction through the more porous calcium oxide. The calcium oxide surface temperature is higher than the calcium carbonate surface temperature, because the calcium oxide surface absorbs more incident radiation than the calcium carbonate surface, and it also conducts into the calcium oxide particle slower than in the calcium carbonate particle. All radiation incident on the pore is allowed to pass into the particle and is absorbed by the particle, because the pore spaces on the

particle surface are modeled as non-scattering and non-absorbing. As a result, the more porous calcium oxide particle absorbs more incident radiation. The mixed particle temperatures lie in between calcium carbonate and calcium oxide, as expected.

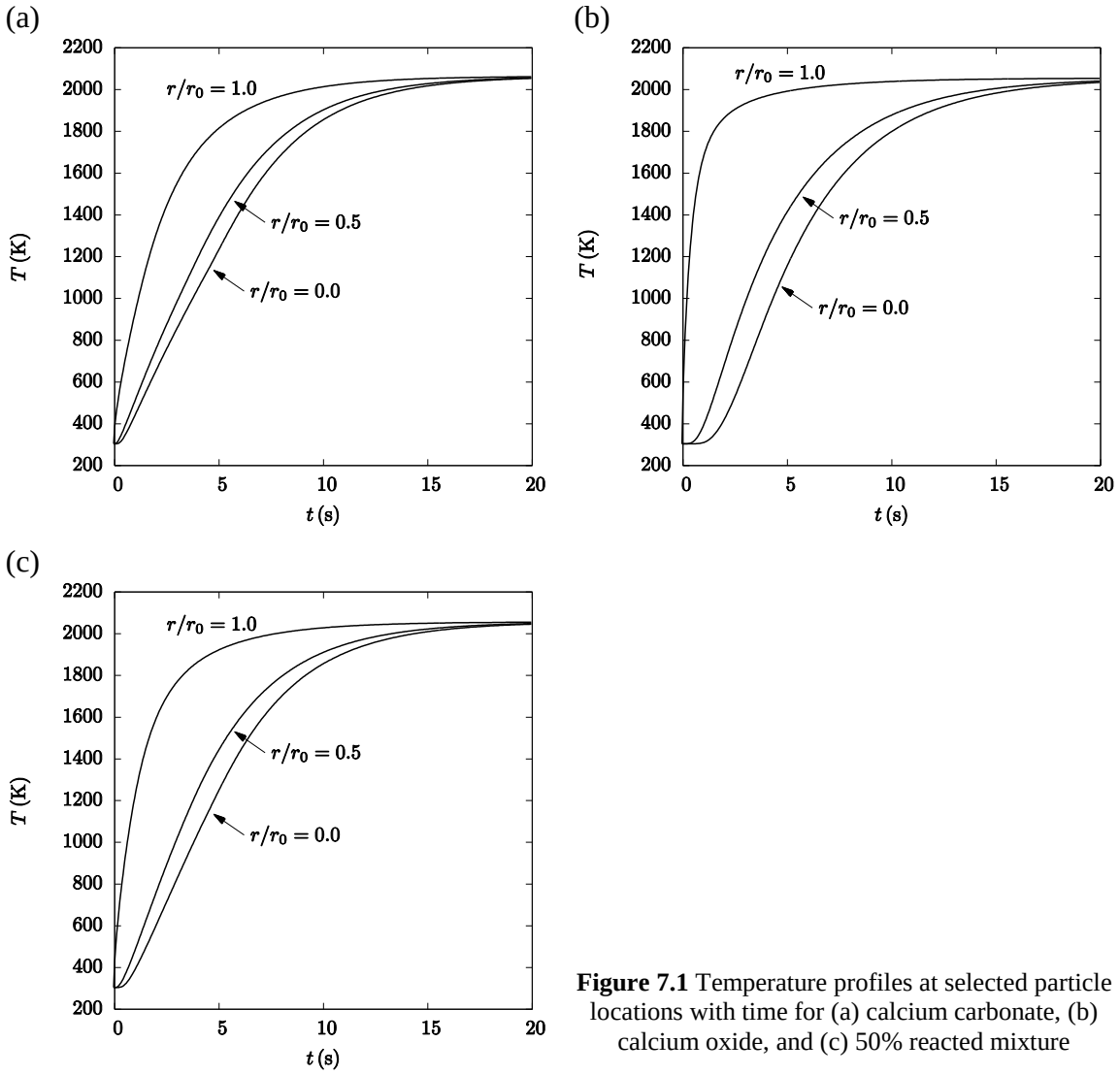

Figure 7.1 Temperature profiles at selected particle locations with time for (a) calcium carbonate, (b) calcium oxide, and (c) 50% reacted mixture

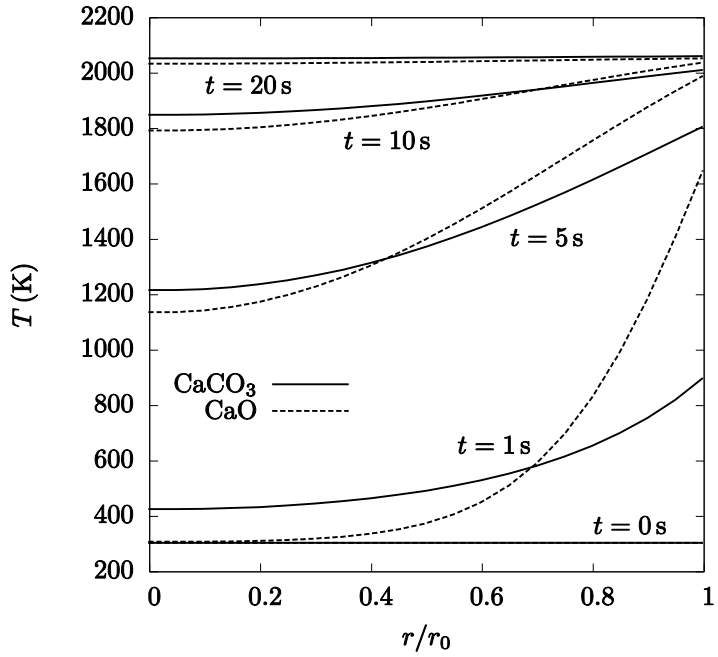

Figure 7.2 Temperature gradients for calcium carbonate and calcium oxide from the particle center to surface for selected times

Particle heating simulations were also conducted without internal radiation to compare the effect of radiation on internal heating. When plotted together, the temperature profiles of conduction only versus conduction with radiation simulations are almost indistinguishable. The temperature difference between the conduction with radiation and conduction only simulations, normalized by the conduction with radiation temperature, is shown in Figure 7.3 for the calcium carbonate and calcium oxide particles. The addition of radiative heat transfer should cause the particle interior to heat up faster than without it and this can be observed in Figure 7.3, where the largest differences occur at the particle center. The center of the particle heats up faster with the inclusion of radiation, but the difference is very small relative to the magnitude of the temperatures involved.

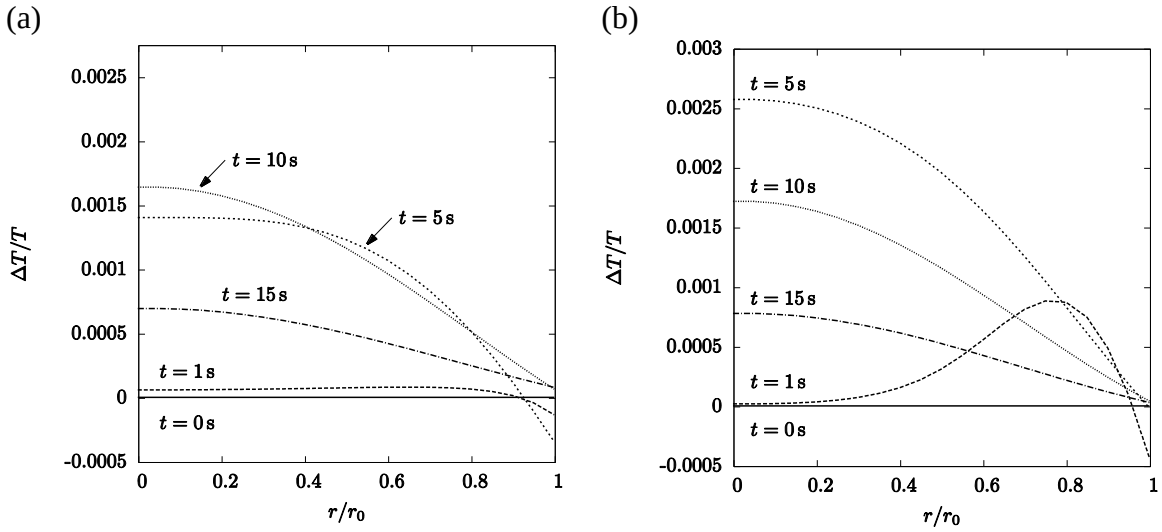

Figure 7.3 Normalized temperature difference versus location for selected times for (a) calcium carbonate and (b) calcium oxide

One possible explanation for the small difference in temperature profiles is that for the optical properties of the solids in this model, radiation is negligible. Another possible explanation is the optical models and the optical properties selected for the solids could be inaccurate. Over-prediction of the extinction coefficient would decrease the radiative conductivity. According to Eq. (5.19), radiative conductivity is proportional to the temperature cubed and inversely proportional to the extinction coefficient. In the temperature range of the current system, the conductivity of the solid components is order of magnitude 1, denoted $O(1)$. In order for the radiative conductive to be of the same order of magnitude, β_{R} must be $O\left(10^4\ \mathrm{m}^{-1}\right)$. Though β_{R} is not directly calculated, values for β_λ plotted in Figure 5.3 are $O\left(10^6\ \mathrm{m}^{-1}\right)$. Numerical investigation of the sensitivity of the system to the extinction coefficient is presented in Section 7.5 below. Numerical investigation with more rigorously selected properties and modeling methods as well as experimental validation are warranted in future work.

7.2 Cyclic heating and cooling

To illustrate the model is capable of being extended to include the carbonation reaction step as well as the calcination reaction step, heating and cooling cycles are simulated. A cycle consists of a heating portion and cooling portion as follows:

$$t_{\text{total}} = t_1 + ct_2 \tag{7.1}$$

where t_{total} is the total cycle time, t_1 is the heating portion of the cycle, t_2 is the cooling portion of the cycle, and c is a varied constant. From the results shown above, a particle reaches near steady state conditions after 10–15 s of heating, so 10 s is selected as the length of the heating portion of the cycle. While particle heating is actively driven by irradiation, cooling of the particle is passive and due only to reradiation and convection. The cooling portion of the cycle also represents particle carbonation. Carbonation reaction kinetics are slower than calcination reaction kinetics. The cooling time is taken to be the same as the heating time, and values of the constant investigated are 1, 2, and 3. The incident flux is defined by the step function

$$\begin{aligned} q''_{\text{solar}} &= 1\times10^{6}\ \text{W m}^{-2}, \quad 0 \le t-(n-1)t_{\text{total}} < t_1 \\ q''_{\text{solar}} &= 0, \qquad\qquad\quad t_1 \le t-(n-1)t_{\text{total}} \le ct_2 \end{aligned} \tag{7.2}$$

where n is the cycle number. Four cycles were simulated for a particle of calcium carbonate. The results of the simulations are shown in Figure 7.4.

The particle does not achieve the maximum temperature in the heating portion of the first cycle but is able to reach near its maximum temperature in all subsequent heating portions regardless of the cooling portion time. When compared to the heating results shown in Section 7.1, the maximum surface temperatures reached in the cycling simulations are slightly lower than the steady state temperature of 2058 K. The maximum temperatures at the surface are 2040 K when c = 1, 2033 K when c = 2, and 2029 K when c = 3. Maximum and minimum temperature of each cycle at the surface and center of the particle are shown in Table 7.2 and Table 7.3. As expected, the particle cools slower than it is heated and cools to a lower temperature the longer the cooling portion of the cycle. The minimum temperatures at the surface are 1196 K when c = 1, 994 K when $c = 2$, and 881 K when c = 3.

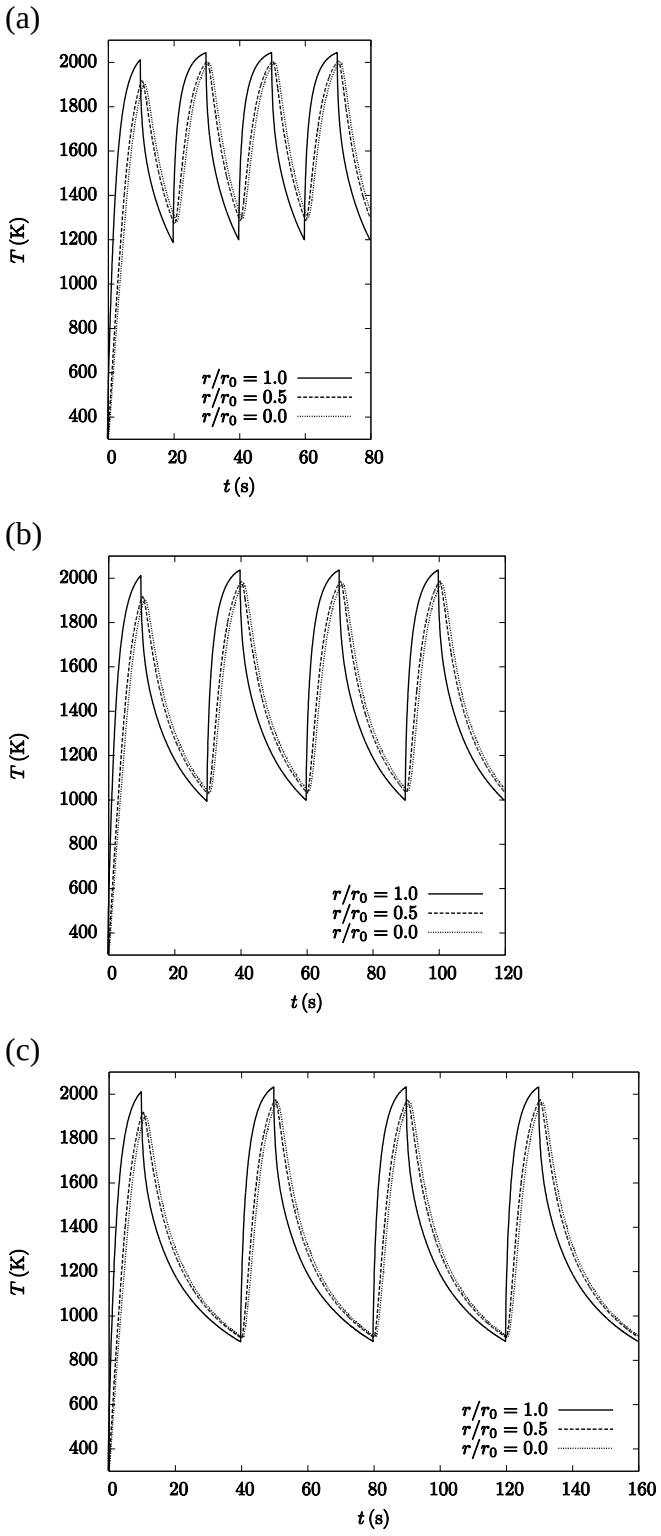

Figure 7.4 Temperature in a particle of calcium carbonate at select locations undergoing cyclic heating and cooling versus time for (a) c = 1, (b) c = 2, and (c) c = 3

Table 7.2 Maximum and minimum particle surface temperatures

Parameter	Times	Cycle 1	Cycle 2	Cycle 3	Cycle 4
T_{max}, $c=1$	10 s, 30 s, 50 s, 70 s	2008	2040	2040	2040
T_{max}, $c=2$	10 s, 40 s, 70 s, 100 s	2008	2033	2033	2033
T_{max}, $c=3$	10 s, 50 s, 90 s, 130 s	2008	2029	2029	2029
T_{min}, $c=1$	20 s, 40 s, 60 s, 80 s	1184	1196	1196	1196
T_{min}, $c=2$	30 s, 60 s, 90 s, 120 s	989	994	994	994
T_{min}, $c=3$	40 s, 80 s, 120 s, 160 s	879	881	881	881

Table 7.3 Maximum and minimum particle center temperatures

Parameter	Times	Cycle 1	Cycle 2	Cycle 3	Cycle 4
T_{max}, $c=1$	10 s, 30 s, 50 s, 70 s	1848	1977	1978	1978
T_{max}, $c=2$	10 s, 40 s, 70 s, 100 s	1848	1948	1948	1948
T_{max}, $c=3$	10 s, 50 s, 90 s, 130 s	1848	1931	1932	1932
T_{min}, $c=1$	20 s, 40 s, 60 s, 80 s	1313	1331	1331	1331
T_{min}, $c=2$	30 s, 60 s, 90 s, 120 s	1040	1046	1046	1046
T_{min}, $c=3$	40 s, 80 s, 120 s, 160 s	905	907	907	907

The temperature at center of the particle lags behind the surface temperature in all simulations. When heating, the temperature at the center of the particle is lower than the surface temperature; when cooling, the temperature at the center of the particle is higher than the surface temperature. With the addition of carbonation kinetics and a model for determining the direction of the reaction, the model could be used to simulation reaction cycling with the appropriate boundary conditions.

7.3 Fixed–pressure calcination

The heat transfer and chemical kinetics components of the model are used to reproduce previously published numerical results to serve as model validation. Ebner and Lipiński [21] modeled the heterogeneous decomposition of calcium carbonate. They considered two different models for the chemical reaction: the volumetric reaction model (VM) and the shrinking core model (SCM). To compare these reaction models, they simulate the

thermochemical calcination of a particle neglecting mass transfer. This is accomplished by fixing the total pressure and partial pressure of carbon dioxide everywhere in the particle.

The model in this work was modified to match the fixed–pressure conditions described in [21]. The largest modifications include neglecting the fluid phase in the same manner as in Sections 7.1 and 7.2, adjusting the ambient surrounding conditions, and changing the ambient carbon dioxide concentration to 400 ppm. The results for total reaction extent are compared in Figure 7.5 and show good agreement.

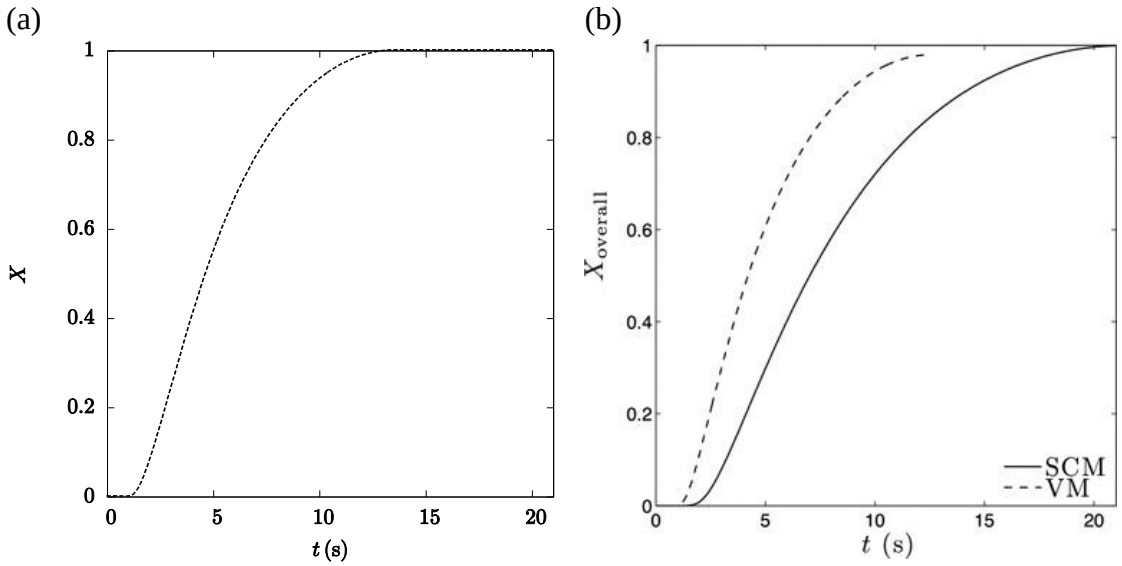

Figure 7.5 Reaction extent versus time from (a) this work and (b) Ebner and Lipiński [21] reproduced with permission from Taylor & Francis

Though there is good agreement, differences are observed between the two simulations. In the results from this work, the particle temperature increases at a slower rate. As a result, the particle also reacts slower and takes longer to reach complete conversion. The model presented here utilizes volume–averaged governing equations. The effective heat transfer properties used with volume–averaged equations account for diminished heat transfer in the solid phase due to the porosity of the solid. The model in [21] does not use volume–averaged equations or effective properties; and the reported heat transfer rates in the particle are likely over-predicted as a result.

7.4 Calcination with mass transfer

The full model is implemented with baseline parameters and results are presented below. The model is then used to investigate reactor operating conditions by varying selected parameters and comparing the results to the baseline simulation.

Baseline simulation

In the initial part of the simulation, all irradiation goes towards heating the particle. The particle begins to react at $t = 1.9$ s when the surface temperature reaches $T = 1274$ K. The reaction progresses through the particle until full conversion is achieved at $t = 34.6$ s. Total particle conversion versus time is shown in Figure 7.6.

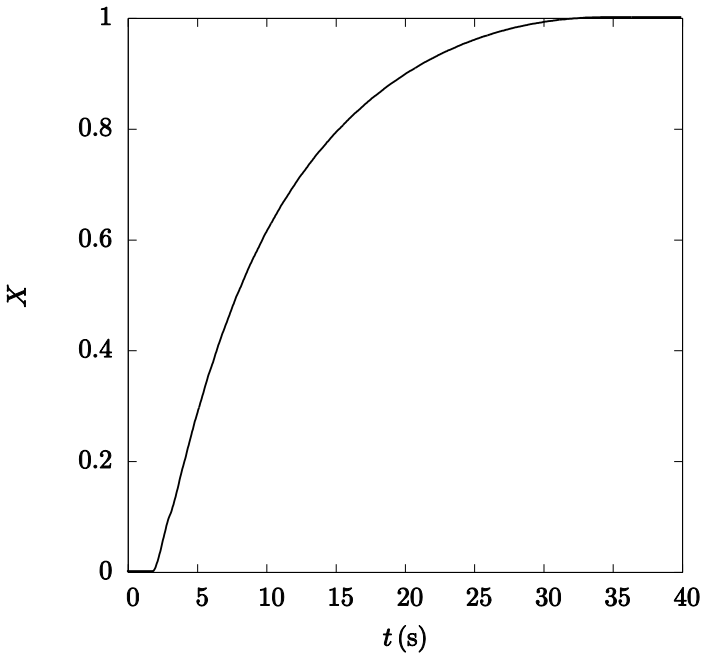

Figure 7.6 Total particle conversion versus time

Once the surface of the particle begins to react, the endothermic reaction consumes most of the irradiated energy and particle heating is impeded. When the particle is locally converted and the chemical reaction stops, particle heating resumes. Figure 7.7 shows the temperature at the particle surface, the particle center, and midway between. Initially, the temperature increases in all three locations until the onset of chemical reaction at the surface. Once the surface of the particle starts reacting, the

heating rate of the surface slows and remains slower until the reaction stops. At which time, the particle surface resumes heating. The temperature at the interior locations remains nearly constant as the outer portions of the particle react. At approximately t = 20 s, the location midway into the particle at $r/r_0 = 0.5$ begins to react. After the reaction completes, the temperature of that location begins to increase again and approaches the surface temperature at the end of the simulation. At approximately $t = 34$ s, the center of the particle begins to react. The chemical reaction stops when the particle is completely converted, and the temperature at the center begins to increase again and approaches the surface temperature.

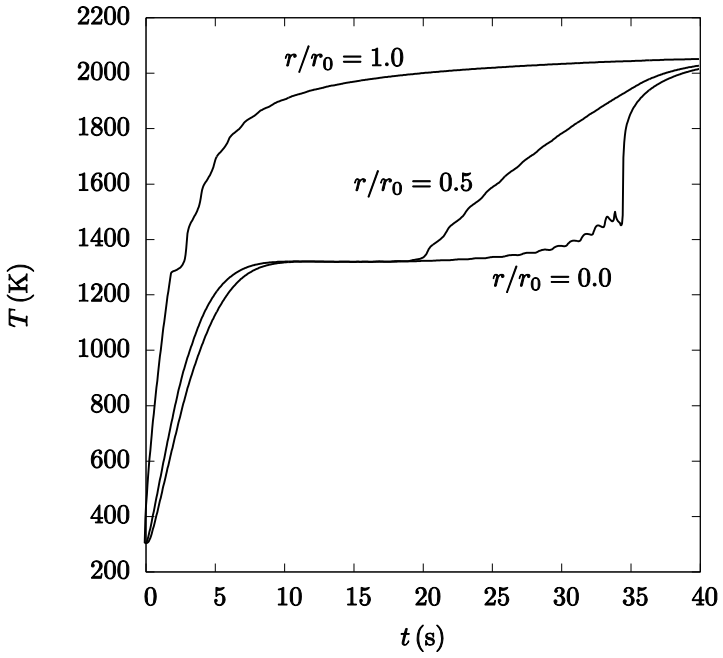

Figure 7.7 Local temperature versus time for selected particle locations

Oscillations can be observed in the temperature profiles at all locations shown in Figure 7.7. After the surface has reacted, there are oscillations as the temperature rises to the maximum values. These oscillations correspond to chemical reaction beginning and ending in interior neighboring elements. When a neighboring interior element starts to react, energy is consumed by the reaction, and the rate of heating of the exterior elements slows. When the reaction in the interior neighboring elements slows and eventually completes, the rate of heating of the exterior elements increases. This starting and

stopping of endothermic decomposition leads to the observed oscillations in the temperature profiles. The oscillations corresponding to onset and completion of chemical reaction. The correspondence is shown in Figure 7.8.

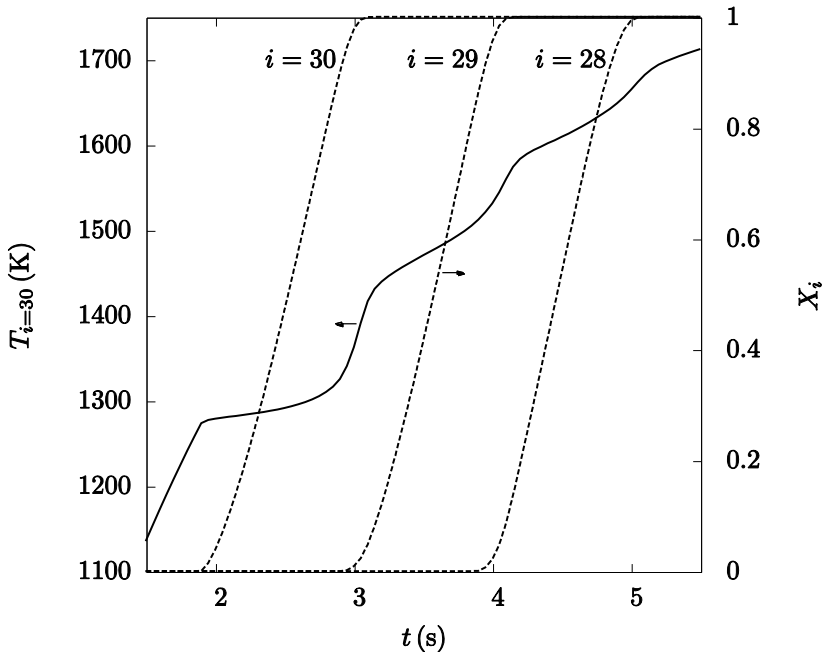

Figure 7.8 Oscillations in surface temperature profile correspond to onset and completion of chemical reaction in neighboring interior elements

The interior most elements begin to heat before the exterior neighboring elements have completed chemical reaction. They also exhibit more severe temperature oscillations than the monotonically increasing temperature oscillations seen in the exterior elements. The thickness of the volume element shells in constant and the grid is uniform, so the volume elements have increasingly smaller volume towards the center of the particle. Once the volume elements have reached a sufficiently small size, the volume over which the chemical reaction is occurring is not large enough for the chemical reaction to consume all of the incoming thermal energy and the excess is conducted to the inner neighboring elements. The temperature oscillations are likely due to numerical instability caused by the very small volumes of the innermost elements where the fast chemical reaction is consuming more energy than is being delivered to the element.

Increasing the number of nodes reduces the oscillations in the temperature profiles, but requires a smaller time step for stability, and the innermost elements still

show small oscillations. With a fine enough grid, the model does produce smooth temperature profiles. It is hypothesized that a non-uniform grid with elements of constant volume would resolve the temperature oscillations in the centermost elements, though this has not yet been tested.

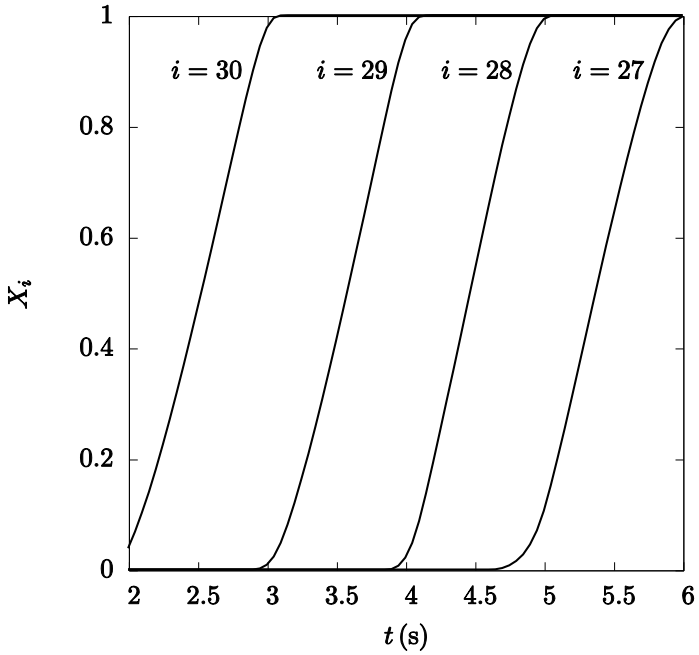

Figure 7.9 Local reaction extent versus time for the outer most four elements

The transition between the reacted portion of the particle and the unreacted portion is fairly sharp and the reaction primarily progresses one element at a time. Consider the first three elements, i = 30, 29, and 28. Onset of chemical reaction in element 30 is equivalent to onset of chemical reaction in the particle and occurs at $t = 1.9$ s. Element 29 begins reacting at $t = 2.95$ s when element 30 is 94.5% reacted. Element 28 begins reacting at $t = 3.90$ s when element 29 is 86.4% reacted. The reaction progresses through the particle in this manner, with the most overlap between neighboring elements occurring midway through the particle. Local reaction extent and minimal overlap between the first four elements is shown in Figure 7.9.

Local reaction rate is shown versus time for several locations in Figure 7.10. Each curve peak represents the local reaction rate in a single element. In the outer elements, the reaction rate peaks are higher and narrower. They also start and stop more sharply than in

the middle elements. This translates to chemical reaction begin and ending suddenly and elements converting quickly. In the middle elements, the reaction rate does not reach as high a value as at the extremes. The peaks are broader and start and end more gradually. This translates into elements that begin reacting slow, take longer to completely convert, and end reacting gradually. In the center elements, the reaction rate peaks are again higher and narrower. This is likely because the volume of the center elements is much smaller than the outer elements so there is less volume to heat and the elements reach reaction temperature faster. The reaction rate is also less impeded by carbon dioxide partial pressure at the center because the preceding elements produce less and less CO_2 towards the particle center. This gives the CO_2 more time to diffuse away from the center elements. The highest reaction rate occurs at the particle center, because the mass of the center element is small and the element is located at the particle center. The size of the element results in the temperature continuing to increase while the element is reacting, increasing the reaction rate. CO_2 produced in interior neighboring elements decreases the local reaction rate in all elements except the central one, because the central element has no interior neighboring elements.

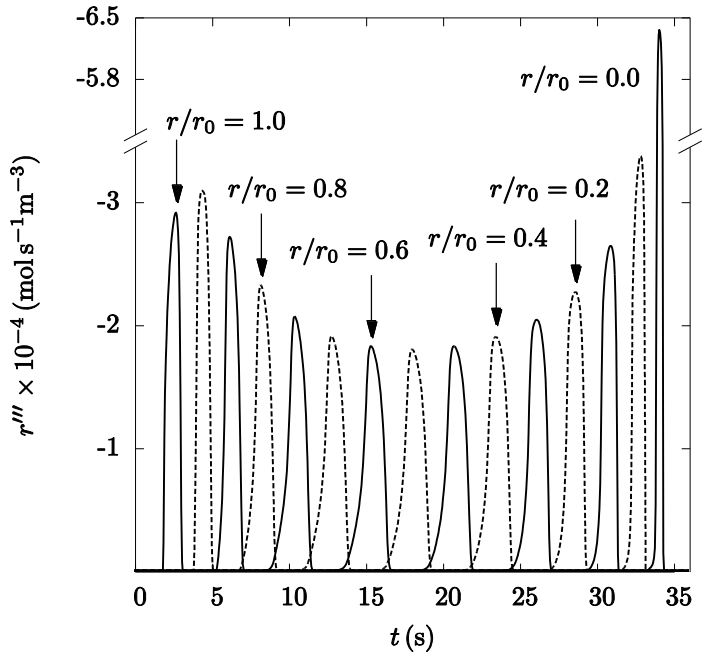

Figure 7.10 Local reaction rate versus time for several locations within the particle

Temperature profiles for different times are shown in Figure 7.11. The temperature profiles within the particle show a distinct transition point between reacted and unreacted areas of the particle in the curves for t = 5, 10, and 30 s. The distinct transition location indicates the reaction zone. The temperature of the reaction zone is fairly constant throughout the simulation and falls between approximately 1300 K and 1375 K. After the onset of chemical reaction, the temperature of the unreacted particle interior is also fairly isothermal at the same temperature as the reaction zone. The reacted portion of the particle is not isothermal and shows strong temperature gradients from the surface to the reaction front. The unreacted portion of the particle at $t = 30$ s is at a higher temperature than the unreacted portion of the particle at $t = 10$ s, so it is clear a small portion of energy is being diverted to particle heating, though the majority goes towards driving the endothermic reaction, indicating the reaction is heat transfer limited.

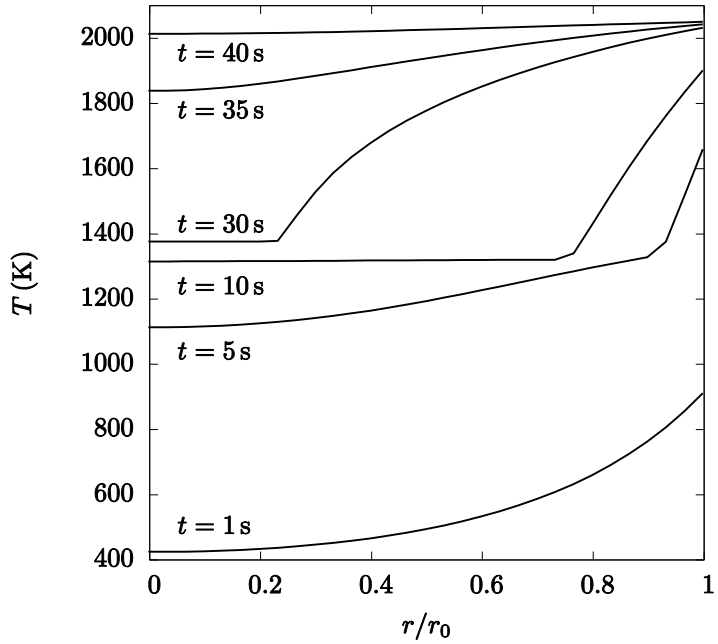

Figure 7.11 Local temperature profiles in the particle for selected times

In the following results, the model is used to investigate the effect of potential operating and reactor conditions. These conditions are solar irradiation, ambient carbon dioxide concentrations, and particle diameter. The values investigated for solar irradiation are 0.5, 1.5, and 2 MW m^{-2}, for ambient carbon dioxide concentration are 400×10^{-6}, 0.15,

and 0.5, and for particle diameter are 0.5, 1.75, 3.75, and 5 mm. Investigated parameters values are shown in Table 7.4 in lighter gray. The baseline values are shown in darker gray.

Table 7.4 Values investigated for solar irradiation, ambient carbon dioxide concentration, and particle diameter

$q''_{\text{solar}}\left(\text{MW m}^{-2}\right)$			0.5	1	1.5	2
$\bar{y}_{\infty,\text{CO}_2}$	400×10^{-6}	0.15	0.5	0.99		
$r_0\ (\text{mm})$		0.5	1.75	2.5	3.75	5

Effect of particle irradiation

Incident irradiation is varied, and the results are presented below. Increased irradiance is expected to heat the particle faster and therefore drive decomposition faster. The results shown here support this. Total particle conversion versus time for all cases is shown in Figure 7.12. Reaction onset and completion times are given in Table 7.5. Increased irradiation results in faster heating rates resulting in faster conversion time.

Table 7.5 Effect of changing irradiation and baseline simulation on reaction onset and completion time

q''_{solar}	Reaction onset time	Complete conversion time
0.5 WM m^{-2}	5 s	61.75 s
1 MW m^{-2}	1.90 s	34.55 s
1.5 MW m^{-2}	1.05 s	26.70 s
2 MW m^{-2}	0.70 s	22.80 s

Decreasing solar concentration from 1 MW m^{-2} to 0.5 MW m^{-2} increased the reaction time by 178%. Doubling the solar concentration from 1 MW m^{-2} to 2 MW m^{-2} decreased the reaction time by 34%.

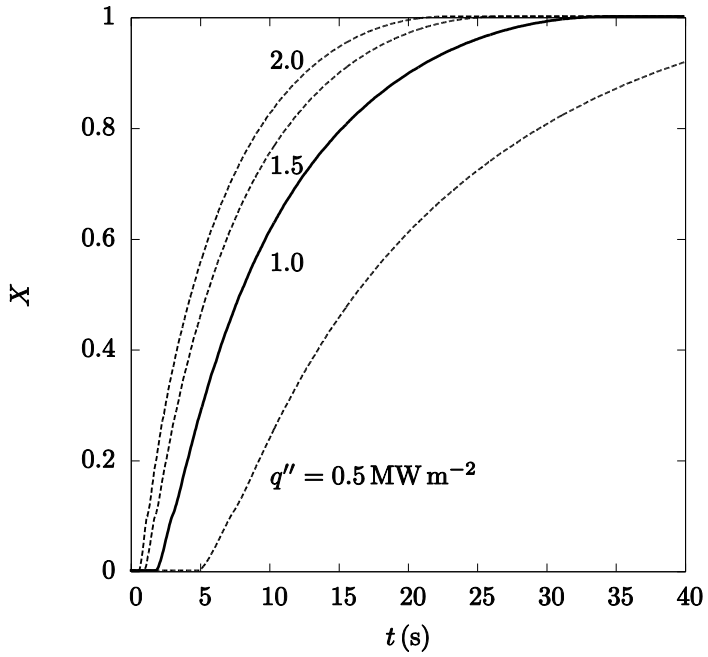

Figure 7.12 Total reaction extent versus time for different irradiation

Effect of ambient CO_2 concentration

Three additional ambient carbon dioxide concentrations were investigated and compared to the baseline concentration. Total particle conversion versus time is shown for the three ambient carbon dioxide concentrations and the baseline case in Figure 7.13. Figure 7.13 shows decreasing ambient carbon dioxide concentration results in faster particle conversion. Reaction onset time, reaction onset temperature, and time to complete conversion are given in Table 7.6. Particle conversion times shown in Table 7.6 show decreasing ambient carbon dioxide concentrations result in decreased time to complete particle conversion.

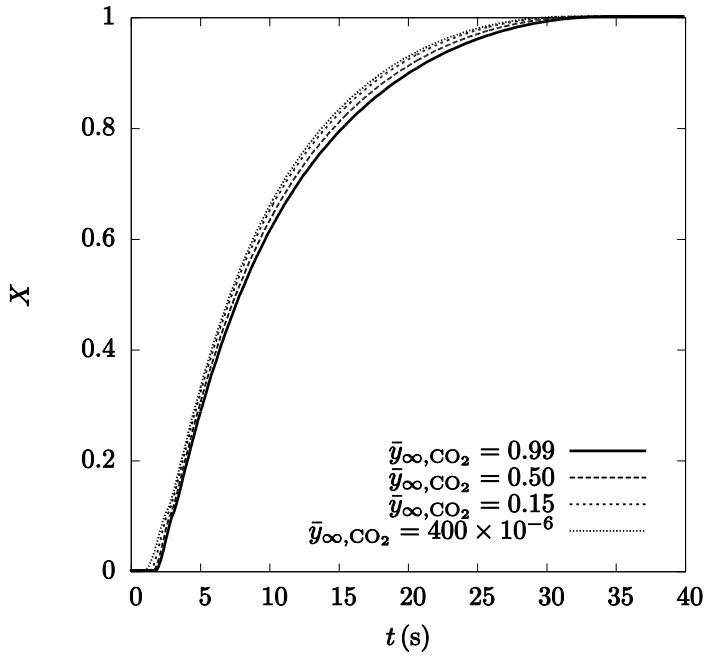

Figure 7.13 Total reaction extent versus time for different ambient carbon dioxide concentrations

While decreasing the ambient carbon dioxide concentration will result in the particle reacting faster, the maximum difference in conversion time, which occurs between 99% CO_2 and 400 ppm CO_2, is only 2.2 s or just over 6% of the time to complete conversion. More significant is the difference in reaction onset temperature. When the ambient carbon dioxide concentration is decreased, the temperature required for decomposition is lower. When the concentration of carbon dioxide is lowered from 99% to 50%, the onset temperature decreases by 52 K or 4%. When the concentration is lowered from 99% to 400 ppm, the onset temperature decreases by 411 K or 32%.

Table 7.6 Effect of changing carbon dioxide concentration and baseline simulation on reaction onset time, reaction onset temperature, and complete conversion time

$\bar{y}_{\infty,CO_2}$	Reaction onset time	Onset temperature	Complete conversion time
400×10^{-6}	0.85 s	863 K	32.35 s
0.15	1.50 s	1136 K	32.80 s
0.5	1.75 s	1222 K	33.80 s
0.99	1.90 s	1274 K	34.55 s

When designing a reactor, changing the ambient carbon dioxide concentration will likely not dramatically change the time to complete conversion, but it may change the temperature and amount of solar concentration required for decomposition. Assuming a blackbody receiver, the minimum amount of irradiation required to reach calcination temperatures when the concentration of CO_2 is 400 ppm is 32 kW m^{-2} or 32 suns. This amount increases for 15%, 50%, and 99% to 95 suns, 127 suns, and 150 suns, respectively.

Effect of particle size

Particle sizes smaller and larger than the baseline particle were investigated. Total particle conversion versus time is shown in Figure 7.14. Smaller particles react significantly faster than the baseline case, while larger particles react significantly slower than the baseline case. Onset of reaction and complete conversion times for all cases are shown in Table 7.7. With less volume, the smaller particles heat faster, react earlier, and finish reacting more quickly. With more volume, the converse is true for larger particles: they heat and react slower.

A smaller particle may react much faster, but in a carbon dioxide capturing system, a smaller particle would be able to capture less carbon dioxide per particle compared to a larger one. The number of particles needed to have an equivalent volume of a 5 mm radius particle is shown in the fourth column of Table 7.7. A 0.5 mm radius particle will reach complete conversion in 2% of the time required for a 5 mm radius particle, but 1000 0.5 mm radius particles are needed to capture the equivalent amount of carbon dioxide that a single 5 mm radius particle could capture with the same CO_2 and radiation conditions at the particle surface.

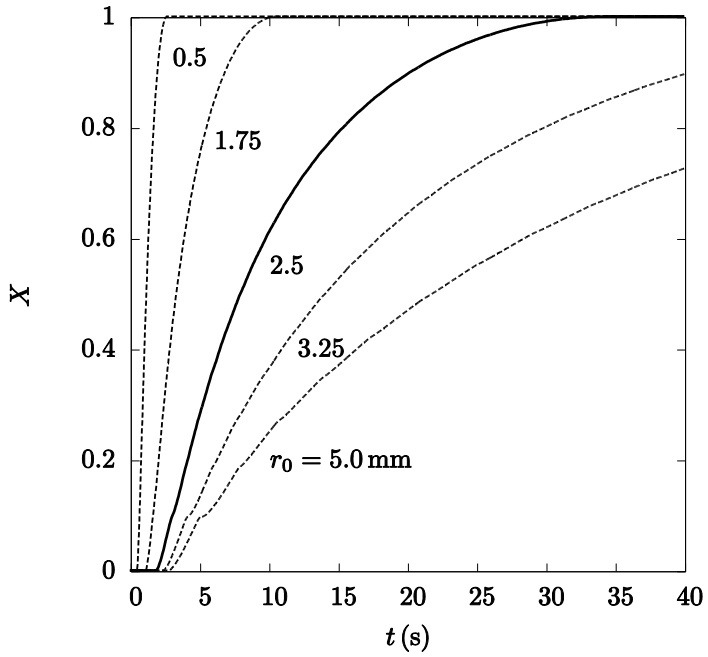

Figure 7.14 Total reaction extent versus time for different particle radii

Table 7.7 Effect of particle radius on reaction onset and complete conversion time

r_0	Reaction onset time	Complete conversion time	$V_{r_0=5\text{ mm}}/V$
0.5 mm	0.55 s	2.70 s	1000
1.75 mm	1.15 s	10.65 s	64
2.5 mm	1.90 s	34.55 s	8
3.75 mm	2.45 s	72.25 s	$2^{10}/_{27}$
5 mm	2.85 s	123.90 s	1

Temperature profiles for the particle surface, center, and midway point are shown in Figure 7.15 for the 0.5 mm radius particle and 1.75 mm radius particle, respectively. Comparing Figure 7.15a to Figure 7.7, the monotonic temperature oscillations observed in the baseline simulation are not observed in the 0.5 mm radius simulation. The monotonic oscillations are observed in the 1.75 mm radius particle simulation as shown in Figure 7.15b, but they are less pronounced than in the baseline simulation. The same number of nodes is used in each simulation, but the 0.5 mm radius particle simulation requires as smaller time step for stability. The same time step for the baseline simulation is used for the 1.75 mm radius particle simulation. The relative spatial resolution is the

same in all simulations, but the elements have smaller volumes in the smaller particle simulations. Smaller element volumes mean the onset and completion of chemistry in each element is over a smaller volume and the reaction does not consume as much energy. As a result the monotonic oscillations are eliminated. The non-monotonic temperature oscillations at the particle center are observed in the 1.75 mm radius simulation but not the 0.5 mm radius simulation. This is likely due to the smaller time step and smaller element volumes in the 1 mm diameter simulation.

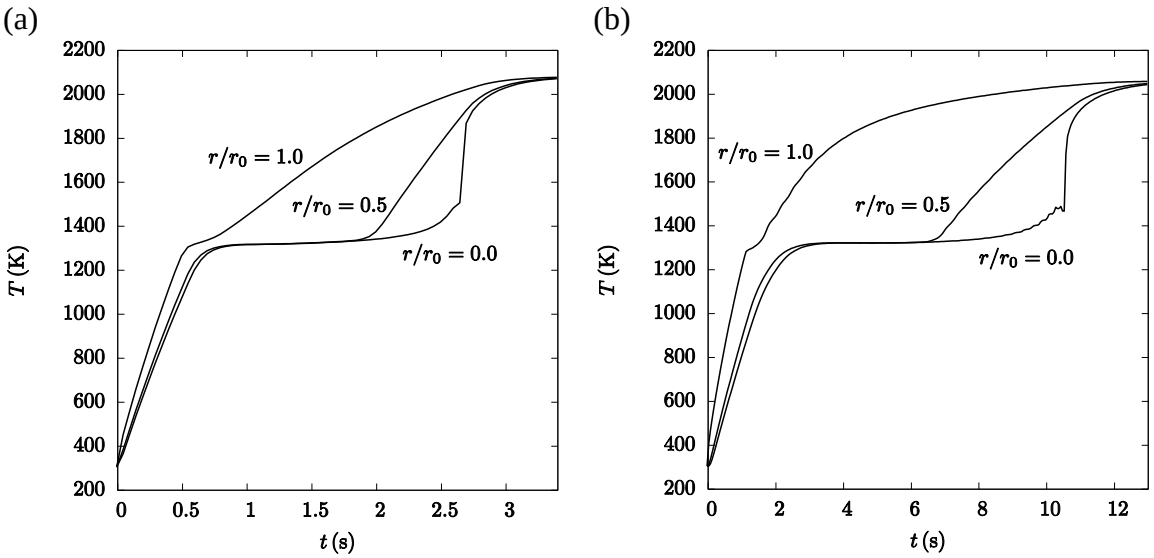

Figure 7.15 Local temperature versus time for selected particle locations for (a) 0.5 mm radius particle and (b) 1.75 mm radius particle

7.5 Sensitivity analysis

An analysis is presented investigating the model's sensitivity to reaction rate, diffusivity, advection, surface radiative properties, and internal radiative heat transfer.

Reaction rate

To investigate the sensitivity of the model to chemical kinetics, the reaction rate is increased and decreased. The slowest reaction rate found in literature was reported by Borgwardt [29]. The reaction rate constant reported in [29] for calcination at 850°C is roughly one order of magnitude smaller than the reaction rate constant yielded by the expression used in this work for the same temperature. The fastest reaction rate the author

was able to find was reported by Fuertes et al. [45], for particles in a fluidized bed reactor roughly one order of magnitude larger than the value range used in this work. Using the reaction rate constants reported in [29] and [45] to establish bounds, two simulations are shown below with reaction rates ten times more and less than the value used in the baseline simulation.

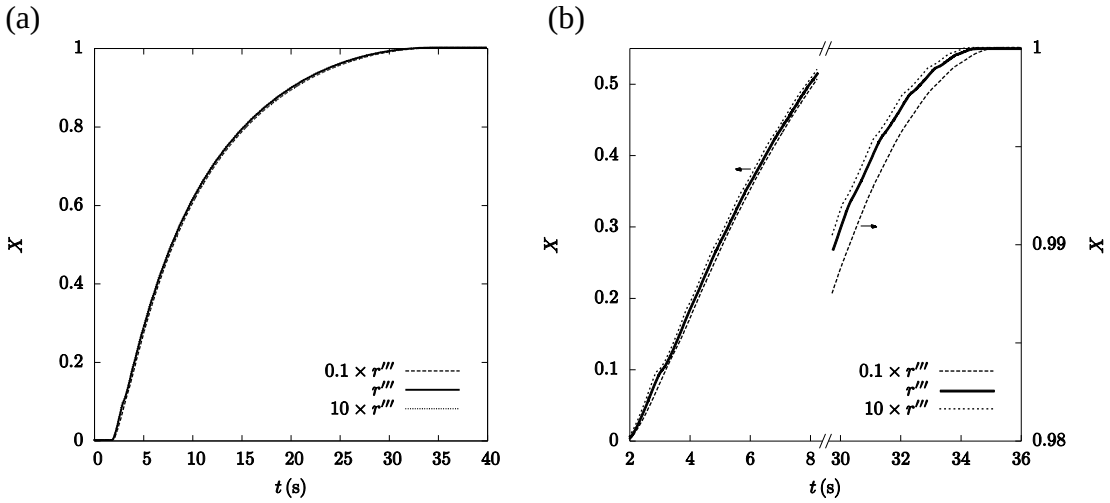

Figure 7.16 Total reaction extent versus time for different reaction rates for (a) the complete simulation and (b) the beginning and end of reaction

Total reaction extent is shown for the reaction rate bounds as well as the baseline simulation in Figure 7.16a. The cases with faster and slower kinetics do not vary enough to be distinguished from the baseline simulation in Figure 7.16a, so a magnified view of the onset of reaction and the completion of reaction is shown in Figure 7.16b. Onset of reaction occurs at the same time in the faster and slower kinetics simulations as it does in the baseline simulation. Once the reaction starts, the simulation with faster kinetics reacts faster and the simulation with slower kinetics reacts slower, as expected. The faster kinetics simulation reaches complete conversion at 34.35 s, which is 0.2 s earlier than in the baseline simulation. The slower kinetics simulation reaches complete conversion at 35.35 seconds, which is 0.8 s later than in the baseline simulation.

Diffusivity

The two effective diffusivity models described in Section 4.1 are compared. DM1 is used in the baseline simulation. The total reaction extent versus time for the two models is

shown in Figure 7.17. The reaction proceeds slightly faster with DM2 than with DM1. The DM2 simulation reached complete conversion after 32.70 s, which is 1.85 s or 5% faster than in the baseline simulation.

DM2 yields a higher effective diffusivity than DM1 for both carbon dioxide and air at the same temperature and porosity (Figure 4.2). The higher diffusivity results in carbon dioxide diffusing away from the reaction site faster. This allows the reaction to proceed faster. Even though the diffusivity differs between the two models by one to two orders of magnitude, overall, the differences in reaction rate and time to conversion between the two models are small.

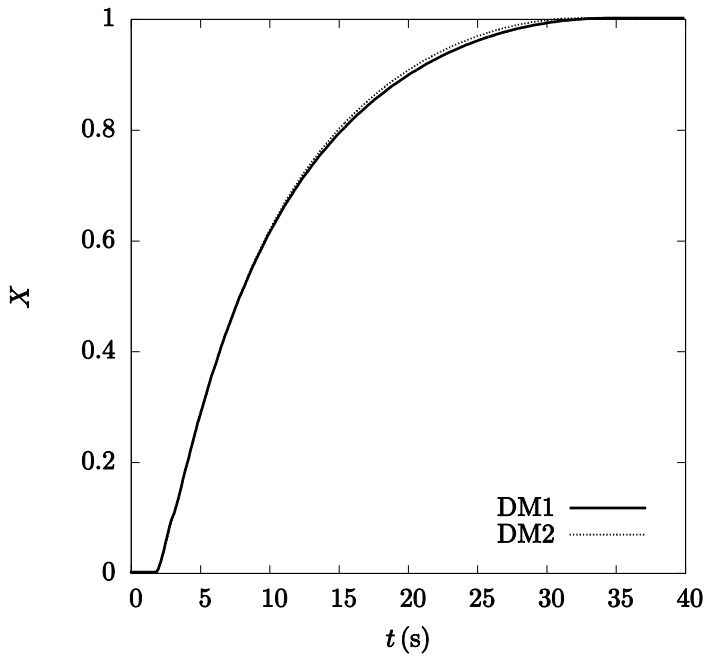

Figure 7.17 Total reaction extent versus time for two effective diffusivity models

Permeability

The effect of permeability on the model on the time to complete calcination and local molar density of carbon dioxide is investigated. The lowest permeability value given in [27] and [34] for the permeability of calcium carbonate (as limestone) is on the order of 10^{-15} m^2. The highest permeability value measured by [35] for the permeability of calcium oxide (as lime) is on the order of 10^{-12} m^2. Two simulations are shown, the first setting the permeability of the solid to a constant value of lower limit ($K = 2\times10^{-15}$ m^2)

and the second setting the permeability to a constant value of upper limit ($K = 1 \times 10^{-12}$ m^2). Higher permeability will allow fluid to advect from areas of higher pressure to areas of lower pressure faster than the baseline simulation. Lower permeability will cause the fluid to advect slower.

The time to complete particle conversion in the higher and lower permeability simulations does not significantly differ from the time to complete particle conversion in the baseline simulation. Comparing the different permeability simulations to the baseline simulation, differences are observed in the predicted molar densities of carbon dioxide. These differences are observed in time and at all locations of the particle. The higher permeability simulation predicts densities higher and lower than in the baseline simulation. The largest increase in molar density in the higher permeability simulation is 33% higher density than in the baseline simulation. The largest decrease in molar density is 3% lower than in the baseline simulation. Similar observations are made for the lower permeability simulation, where the largest differences observed in the molar density of carbon dioxide are 0.8% higher than the baseline simulation and 6% lower than the baseline simulation. Higher and lower values are likely observed in both simulations because the pressure gradients that drive advection can oppose the concentration gradients that drive diffusion. The opposing fluxes result in locations of higher and lower densities.

While the different permeability values do alter the concentrations of the fluid species from the baseline simulation and at certain times up to 33%, the difference in fluid species concentration does not change the overall conversion time. This is likely because mass transfer by diffusion dominates mass transfer by advection for all permeability values considered. In the baseline simulation, the largest mass flux due to advection is one order of magnitude smaller than the largest mass flux due to diffusion. In the lower permeability simulation, the largest mass flux due to advection is three orders of magnitude smaller than the largest mass flux due to diffusion. In the higher permeability simulation, the largest mass flux due to advection is the same order of magnitude as the largest mass flux due to diffusion but six times smaller. The permeability of the solid everywhere would have to be at least as high as the maximum

reported value for calcium oxide for advection to have the same order of magnitude as diffusion.

Surface radiative properties

Four surface radiative property models, as identified in Section 5.5, are investigated. The results for Models 1 and 3, which both assume the particle is non-absorbing, are practically identical. The total reaction extent versus time is shown in Figure 7.18 for each case. The non-absorbing model simulations reach complete conversion first after 33.80 s, the Model 2 simulation reaches complete conversion next at 34.15 s, and then the Model 4 simulation, which is the baseline simulation, reaches complete conversion at 34.55 s.

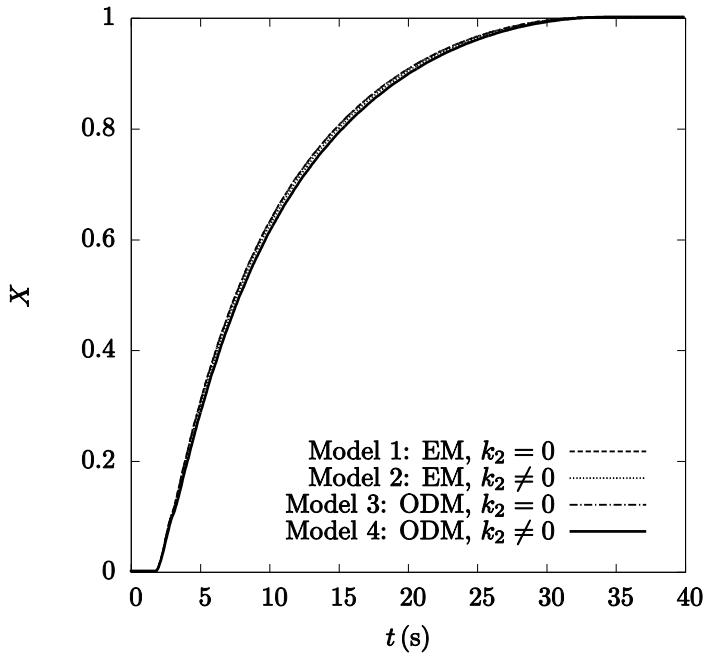

Figure 7.18 Total reaction extent versus time for different surface radiative property models

Another difference between the models is the maximum surface temperature reached in the simulation. The surface temperature approaches the maximum steady state temperature the particle would achieve if it was indefinitely heated. This temperature depends on the surface radiative properties. The surface temperature versus time is shown in Figure 7.19. As before with complete conversion time, the non-absorbing models reach

the highest temperature of 2054.9 K, Model 2 reaches the next highest temperature of 2051.2 K, and Model 4, the baseline simulation, reaches the lowest temperature of 2046.4 K. Higher surface temperature and faster reaction time suggest that the non-absorbing models have the lowest reflectivity, while Model 4 yields the highest reflectivity, but the overall effect on particle heating and reaction rate are small.

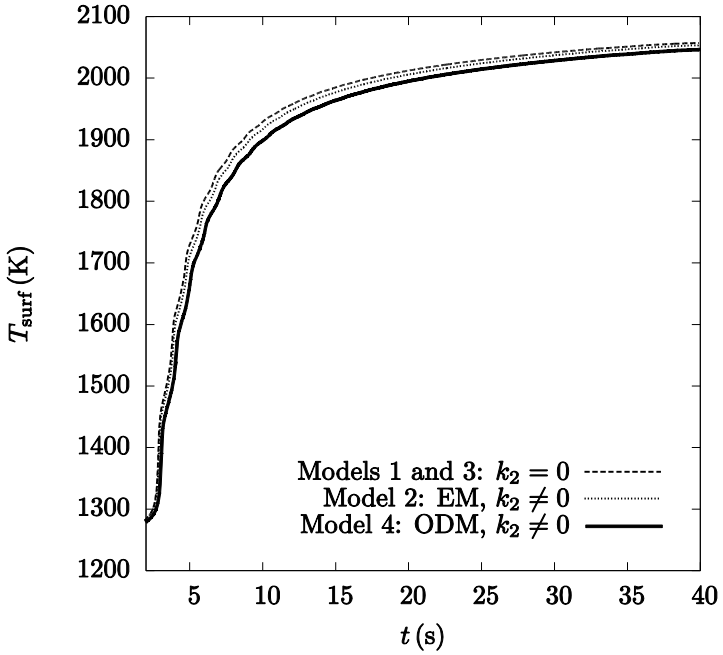

Figure 7.19 Surface temperature versus time for different surface radiative property models

Internal radiative heat transfer

The effect of internal radiative heat transfer is investigated. Since it was established in Section 8.1 that the radiative conductivity had little effect on heat transfer in the particle, only cases that increases the radiative conductivity are explored in this section. The radiative conductivity is inversely proportional to the Rosseland-mean extinction coefficient in Eq. (5.19). Thus, to investigate increased radiative conductivity, values of the extinction coefficient 10 and 100 times smaller than the baseline value are used. The total reaction extent versus time is shown in Figure 7.20. The lower extinction coefficients delay onset of reaction time but decrease time to complete conversion. The onset and complete conversion times are given in Table 7.8.

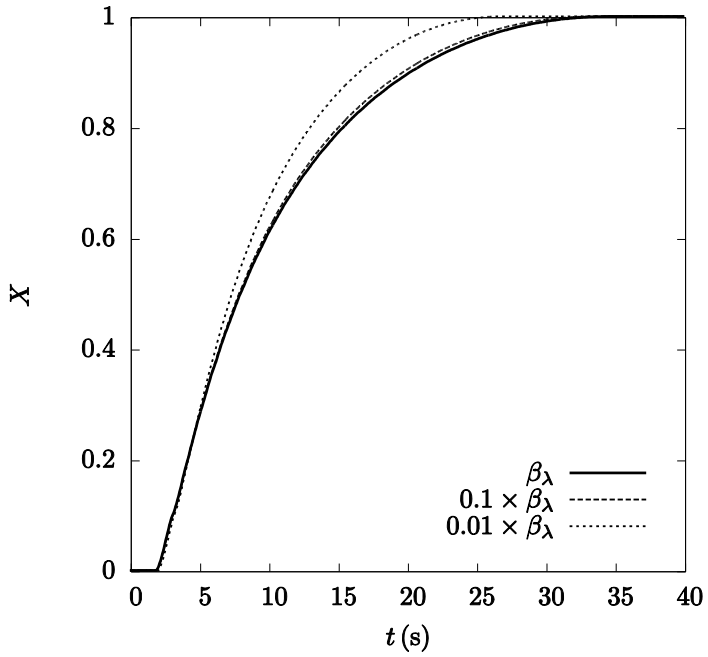

Figure 7.20 Total reaction extent versus time for different extinction coefficients

Table 7.8 Reaction onset and conversion time and final surface temperature for different extinction coefficients

β_λ	Reaction onset time	Complete conversion time	T_{surf} after 40 s
β_λ	1.90 s	34.55 s	2046 K
$0.1\times\beta_\lambda$	1.95 s	33.45 s	2047 K
$0.01\times\beta_\lambda$	2.05 s	26.70 s	2049 K

Increased radiative conductivity delays onset of reaction because the temperature in the surface element does not heat up as fast as the baseline simulation. More energy is conducted into the particle when conductivity is higher rather than the energy increasing the local temperature. This results in delayed onset of reaction at the surface but also results in the interior elements heating faster and reacting earlier.

The local reaction extent versus time is shown in Figure 7.21 for locations at and near the particle surface. At the surface, the surface element in the baseline simulation reacts first. Elements not shown in Figure 7.21 between the surface element and the $r/r_0 = 0.9$ element react at approximately the same time and rate. When reaction front reaches $r/r_0 = 0.9$, the order has reversed and the element in the baseline simulation

reacts last. As the reaction front progresses into the particle, the difference in time between when the elements react in each simulation increases. This results in the $0.01\times\beta_\lambda$ simulation reaching complete conversion 77% faster than the baseline simulation.

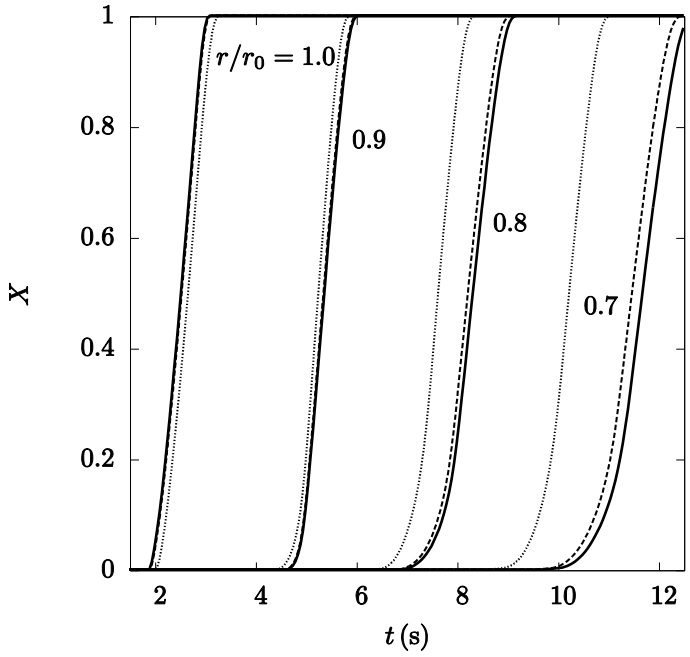

Figure 7.21 Local reaction extent versus time for elements near the particle surface

Chapter 8 Conclusions and outlook

A model has been presented that captures the coupled physical phenomena of chemistry, mass transfer, and heat transfer in a two phase, reacting porous particle. Using the model, the thermochemical decomposition of calcium carbonate is analyzed for use in a solar carbon capture application. The effect of selected physical parameters, operating conditions, and modeling methods are investigated. The model predicts, with previously unreported detail, the interaction of the couple physical phenomena at the intraparticle level.

Conclusions

A goal of this work is to understand the coupled heat transfer, mass transfer, and chemical processes in a decomposing calcium carbonate particle. A distinct reaction front moving through the particle is observed. The distinction in temperature gradients at the reaction front between the reacted and unreacted portions of the particle is pronounced and suggests the reaction is heat transfer limited for the conditions considered in this work. The analysis of the effect of irradiation and particle size agree with the heat transfer limitation conclusion: 1) smaller particles reach complete conversion faster than larger particle under the same conditions, and 2) particles subjected to higher irradiation reach complete conversion faster than particles subjected to lower irradiation under the same conditions. In both cases, the temperature required for the chemical reaction to proceed is reached earlier in the simulation resulting in faster particle conversion.

For the analysis of a potential reactor and operating conditions, the effect of the ambient carbon dioxide concentration is considered in addition to irradiation and particle size mentioned above. For these parameters and in the ranges investigated, particle size has the greatest effect on particle conversion time. This suggests an optimal reactor design would contain many evenly-heated, small particles as opposed to an equivalent volume of larger particles. Ambient carbon dioxide concentration did not significantly alter the time required for complete particle conversion, but it did alter the minimum temperature required for the reaction to proceed. A required minimum temperature would

aid in the determination of the minimum amount of solar concentration required for a calcination reactor. The sensitivity analysis shows the model is less sensitive to mass transfer related quantities and chemical kinetics, and it is more sensitive to heat transfer related quantities.

The numerical solution of the model utilizes the explicit Euler method for time integration. The time step required for stability with this method is sufficiently small to produce meaningful results for this study, but simulations are computationally costly. The computational costs of extending this model to a group of particles, as in a reactor, would be prohibitively high. The evaluation of radiative conductivity is the most computationally expensive component. Simulations which do not solve Eq. (5.37) for the radiative conductivity are ten times less computationally expensive which is significantly faster than the equivalent simulation with radiative conductivity.

Outlook

Several lengths scales are involved in the implementation of solar carbon dioxide capture using calcium oxide looping. This study focuses on processes of interest at the particle level for the calcination reaction. The next step is to add carbonation kinetics to the model in order to simulation the complete reaction loop. Because full carbonation of each particle is ideal, it is expected that the mass transfer of carbon dioxide through the outer layer of calcium carbonate will be an important design concern. The addition of carbonation kinetics and experimental validation of the modeling methods employed in this work would result in a powerful tool for providing guidance in reactor design and the realization of calcium oxide looping for carbon capture.

The mathematical model can also be applied to other thermochemical systems with applications of industrial interest. With the appropriate closure equations, the model could be applied to other heterogeneous solid–fluid reacting systems, such as metal plating, the oxidation of sulfide ores into metal oxides and other metallurgic refining processes, and the nitrogenation of calcium carbite to cyanamide. It could also be employed for use with shrinking-particle reacting systems of industrial interest or porous phase-changing systems for thermal storage.

References

[1] H. Herzog. Carbon Dioxide Capture and Storage. Chapter 13 of D. Helm and C. Hepburn, Eds. *The Economics and Politics of Climate Change,* Oxford University Press, New York, 2009.

[2] S. A. Rackley. *Carbon Capture and Storage*, Butterworth-Heinemann, Cambridge, 2010.

[3] L. Reich, L. Yue, R. Bader, and W. Lipiński. Towards solar thermochemical carbon dioxide capture via calcium oxide looping: A review. *Aerosol and Air Quality Research,* 2013, in press.

[4] W. Lipiński and A. Steinfeld. Heterogeneous thermochemical decomposition under direct irradiation. *International Journal of Heat and Mass Transfer,* 47: 1907–1916, 2004.

[5] W. Lipiński, A. Z'Graggen, and A. Steinfeld. Transient radiation heat transfer within a nongray nonisothermal absorbing–emitting–scattering suspension of reacting particles undergoing shrinkage. *Numerical Heat Transfer, Part B: Fundamentals,* 47:443–457, 2005.

[6] S. Haussener, W. Lipiński, J. Petrasch, P. Wyss, and A. Steinfeld. Tomographic characterization of a semitransparent-particle packed bed and determination of its thermal radiative properties. *Journal of Heat Transfer,* 131:072701, 2009.

[7] L. Dombrovsky and W. Lipiński. Transient temperature and thermal stress profiles in semi-transparent particles under high-flux irradiation. *International Journal of Heat and Mass Transfer,* 50: 2117–2123, 2007.

[8] P. K. Gallagher and D. W. Johnson Jr. The effect of sample size and heating rate on the kinetics of the thermal decomposition of $CaCO_3$. *Thermochimica Acta,* 6:67–83, 1973.

[9] J. Khinast, G. F. Krammer, C. Brunner, and G. Staudinger. Decomposition of limestone: the influence of CO_2 and particle size on the reaction rate. *Chemical Engineering Science,* 51:623–634, 1996.

[10] F. García-Labiano, A. Abad, L. F. de Diego, P. Gayán, and J. Adánez. Calcination of calcium-based sorbents at pressure in a broad range of CO_2 concentrations. *Chemical Engineering Science,* 57:2381–2393, 2002.

[11] S. K. Bhatia and D. D. Perlmutter. Effect of the product layer on the kinetics of the CO2-lime reaction. *AIChE Journal,* 29:79–86, 1983.

[12] V. Nikulshina, M. E. Gálvez, and A. Steinfeld. Kinetic analysis of the carbonation reactions for the capture of CO_2 from air via the $Ca(OH)_2$–$CaCO_3$–CaO solar thermochemical cycle. *Chemical Engineering Journal,* 129:75–83, 2007.

[13] S. Stendardo and P. U. Foscolo. Carbon dioxide capture with dolomite: a model for gas–solid reaction within the grains of a particulate sorbent. *Chemical Engineering Science*, 64:2343–2352, 2009.

[14] G. D. Silcox, J. C. Kramlich, and D. W. Pershling. A mathematical model for the flash calcination of dispersed $CaCO_3$ and $Ca(OH)_2$ particles. *Industrial and Engineering Chemistry Research*, 28:155–160, 1989.

[15] D. Mess, A. F. Sarofim, and J. P. Longwell. Product layer diffusion during the reaction of calcium oxide with carbon dioxide. *Energy and Fuels*, 13:999–1005, 1999.

[16] J. C. Abanades. The maximum capture efficiency of CO_2 using a carbonation/calcination cycle of $CaO/CaCO_3$. *Chemical Engineering Journal*, 90:303–306, 2002.

[17] H. Gupta and L. S. Fan. Carbonation-calcination cycle using high reactivity calcium oxide for carbon dioxide separation from flue gas. *Industrial and Engineering Chemistry Research*, 41:4035–4042, 2002.

[18] B. Khoshandam, R. V. Kumar, and L. Allahgholi. Mathematical modeling of CO_2 removal using carbonation with CaO: The grain model. *Korean Journal of Chemical Engineering*, 27:766–776, 2010.

[19] P. P Ebner and W. Lipiński. Heterogeneous thermochemical decomposition of a semi-transparent particle under direct irradiation. *Chemical Engineering Science*, 66: 2677–2689, 2011.

[20] Y. S. Yu, W. Q. Liu, H. An, F. S. Yang, G. X. Wang, B. Feng, Z. X. Zhang, and V. Rudolph. Modeling of the carbonation behavior of a calcium based sorbent for CO_2 capture. *International Journal of Greenhouse Gas Control*, 10:510–519, 2012.

[21] P. P. Ebner and W. Lipiński. Heterogeneous thermochemical decomposition of a semi-transparent particle under high-flux irradiation-changing grain size versus shrinking core models. *Numerical Heat Transfer, Part A: Applications*, 62:412–431, 2013.

[22] B. R. Stanmore and P. Gilot. Review—calcination and carbonation of limestone during thermal cycling for CO_2 capture. *Fuel Processing Technology*, 86: 1707–1743, 2005.

[23] C. Georgakis, C. W. Chang, and J. Szekely. A changing grain size model for gas-solid reactions. *Chemical Engineering Science*, 34:1072–1075, 1979.

[24] S. K. Bhatia and D. D. Perlmutter. A random pore model for fluid–solid reactions: I. Isothermal, kinetic control. *AIChE Journal*, 26:379–386, 1980.

[25] S. K. Bhatia and D. D. Perlmutter. A random pore model for fluid-solid reactions: II. Diffusion and transport effects. *AIChE Journal*, 27:247–254, 1981.

[26] S. Whitaker. *The Method of Volume Averaging*, Kluwer Academic, Dordrecht, 1999.

[27] M. Kaviany. *Principles of Heat Transfer in Porous Media*, 2nd ed., Springer, New York, 1995.

[28] D. J. Keene, J. H. Davidson, and W. Lipiński. A model of transient heat and mass transfer in a heterogeneous medium of ceria undergoing nonstoichiometric reduction. *Journal of Heat Transfer*, 135:052701, 2013.

[29] R. H. Borgwardt. Calcination kinetics and surface area of dispersed limestone particles. *AIChE Journal*, 31:103–111, 1985.

[30] J. R. Ingraham and P. Marier. Kinetic studies on the thermal decomposition of calcium carbonate. *Canadian Journal of Chemical Engineering*, 41:170–173, 1963.

[31] I. Barin. *Thermochemical data of pure substances*, VCH, Weinheim, 1989.

[32] S. R. Turns. *An Introduction to Combustion*, 3rd ed., McGraw–Hill, New York, 2012.

[33] E. N. Fuller, P. D. Schettler, and J. C. Giddings. A new method for prediction of binary gas-phase diffusion coefficients. *Industrial and Engineering Chemistry*, 58:19–27, 1966.

[34] B. Zinszner and F. M. Pellerin. *A Geoscientist's Guide to Petrophysics*. Editions Technip, Paris, 2007.

[35] J. Válek, J. Hughes, and P. Bartos. Gas Permeability, Porosity and Carbonation of Modern Conservation Lime Mortar Mix. In F. H. Wittman, *Materials for Buildings and Structures*, Wiley–VCH, Weinheim, 2000.

[36] C. J. Geankoplis. *Transport Processes and Separation Process Principles*, 4th ed., Prentice Hall, Upper Saddle River, 2003.

[37] N. Wakao, S. Kaguei, and T. Funazkri. Effect of fluid dispersion coefficients on particle-to-fluid heat transfer coefficients in packed beds. *Chemical Engineering Science*, 34: 325–336, 1979.

[38] S. Whitaker. Forced convection heat transfer correlations for flow in pipes, past flat plates, single cylinders, single spheres, and for flow in packed beds and tube bundles. *AIChE Journal*, 18:361–371, 1972.

[39] M. F. Modest. *Radiative Heat Transfer*, 2nd ed., Academic Press, San Diego, 2003.

[40] V. Orofino, A. Blanco, M. I. Blecka, S. Fonti and A. Jurewicz. Carbonates and coated particles on Mars. *Planetary and Space Science*, 48: 1341–1347, 2000.

[41] M. Q. Brewster and T. Kunitomo. The optical constants of coal, char, and limestone. *Transactions of the ASME*, 106:678–683, 1984.

[42] C. F. Bohren and D. R. Huffman. *Absorption and Scattering of Light by Small Particles*, Wiley–VCH, Weinheim, 2004.

[43] L. A. Dombrovsky. The use of transport approximation and diffusion-based models in radiative transfer calculations. *Computational Thermal Sciences*, 4:297–315, 2012.

[44] J. A. Duffie and W. A. Beckman. *Solar Engineering of Thermal Processes*, 3rd ed., Wiley, Hoboken, 2006.

[45] A. B. Fuertes, G. Marbán, and F. Rubiera. Kinetics of thermal decomposition of limestone particles in a fluidized bed reactor. *Transactions of the Institution of Chemical Engineers*, 71(A):421–728, 1993.

[46] C. L. Yaws. *Handbook of Transport Property Data*, Gulf Publishing, Houston, 1995.

[47] C. L. Yaws. *Transport Properties of Chemicals and Hydrocarbons*, William Andrews, Norwich, 2009.

[48] M. Binnewies and E. Milke. *Thermochemical Data of Elements and Compounds*, 2nd ed., Wiley–VCH, Weinheim, 2002.

[49] G. Zoth and R. Haenel. Appendix of R. Haenel, L. Rybach, and L. Stegena, Ed., *Handbook of Terrestrial Heat-Flow Density Determination*, Kluwer Academic, Dordrecht, 1988.

[50] T. L. Bergman, A. S. Lavine, F. P. Incropera, and D. P. Dewitt. *Fundamentals of Heat and Mass Transfer*, 7th ed., Wiley, Hoboken, 2011.

Appendix

The material properties used for calcium carbonate, calcium oxide, carbon dioxide, and air are reported in the following tables. Properties include mass density, molar mass, viscosity, molar specific enthalpy, molar specific heat capacity, and conductivity. Expressions for specific enthalpy for calcium carbonate, calcium oxide, and carbon dioxide were obtained by the integration of specific heat capacity for each species. Specific enthalpies and heat capacities of nitrogen and oxygen are linearly interpolated from tabulated data in [32] and converted to molar quantities. When ranges are given for expressions, the value at the range limit is used outside of the applicable range.

Table A.1 Density and molar mass

Variable	Value	Units
ρ_{CaCO_3}	2730	kg m^{-3}
ρ_{CaO}	3350	kg m^{-3}
M_{CaCO_3}	0.10009	kg mol^{-1}
M_{CaO}	0.5607	kg mol^{-1}
M_{CO_2}	0.44011	kg mol^{-1}
M_{air}	0.2885	kg mol^{-1}

Table A.2 Viscosity expressions

Parameter	Expression (N s m^{-2})	Range (K)	Ref.
μ_{CO_2}	$1.2\times10^{-6}+\left(5.0\times10^{-8}\right)T-\left(1.1\times10^{-11}\right)T^2$	$195\le T\le1500$	[46]
μ_{N_2}	$4.5+\left(6.4\times10^{-1}\right)T-\left(2.7\times10^{-4}\right)T^2+\left(5.4\times10^{-8}\right)T^3$	$63\le T\le1970$	[47]
μ_{O_2}	$-4.9+\left(8.1\times10^{-1}\right)T-\left(4.0\times10^{-4}\right)T^2+\left(1.0\times10^{-7}\right)T^3$	$54\le T\le1500$	[47]

Table A.3 Molar specific enthalpy expressions

Parameter	Expression (J mol^{-1})	Range (K)
$\bar{h}_{\mathrm{CaCO_3}}$	$\left(1.1\times10^{2}\right)T+\left(1.1\times10^{-2}\right)T^{2}+\left(2.6\times10^{6}\right)T^{-1}-1.3\times10^{6}$	$298\le T\le1170$
$\bar{h}_{\mathrm{CaO}}$	$50.4T+\left(2.1\times10^{-3}\right)T^{2}+\left(8.5\times10^{5}\right)T^{-1}-6.5\times10^{5}$	$298\le T\le3200$
$\bar{h}_{\mathrm{CO_2}}$	$51.1T+\left(2.2\times10^{-3}\right)T^{2}+\left(1.5\times10^{6}\right)T^{-1}-4.1\times10^{5}$	$298\le T\le1500$
$\bar{h}_{\mathrm{air}}$	$0.79\bar{h}_{\mathrm{N_2}}+0.21\bar{h}_{\mathrm{O_2}}$	

Table A.4 Molar specific heat capacity expressions

$\bar{c}_{\mathrm{p}}$	Expression (J mol^{-1} K^{-1})	Range (K)	Ref.
$\bar{c}_{\mathrm{p,CaCO_3}}$	$1.1\times10^{2}+\left(2.2\times10^{-2}\right)T-\left(2.6\times10^{6}\right)T^{-2}$	$298\le T\le1170$	[48]
$\bar{c}_{\mathrm{p,CaO}}$	$50.4+\left(4.2\times10^{-3}\right)T-\left(8.5\times10^{5}\right)T^{-2}$	$298\le T\le3200$	[48]
$\bar{c}_{\mathrm{p,CO_2}}$	$51.1+\left(4.4\times10^{-3}\right)T-\left(1.5\times10^{6}\right)T^{-2}$	$298\le T\le1500$	[48]

Table A.5 Conductivity expressions

k	Expression (W m^{-1} K^{-1})	Range (K)	Ref.
$k_{\mathrm{CaCO_3}}$	$\left(1.073\times10^{3}\right)\left(77+T\right)^{-1}+0.13$	$273\le T\le1173$	[49]
k_{CaO}	0.6		[19]
$k_{\mathrm{CO_2}}$	$-6.1\times10^{-3}+\left(7.5\times10^{-5}\right)T+\left(9.5\times10^{-9}\right)T^{2}-\left(1.1\times10^{-11}\right)T^{3}$	$195\ \le T\le1500$	[46]
k_{air}	$0.79k_{\mathrm{N_2}}+0.21k_{\mathrm{O_2}}$		
$k_{\mathrm{N_2}}$	$-2.3\times10^{-4}+\left(1.0\times10^{-4}\right)T-\left(6.0\times10^{-8}\right)T^{2}+\left(2.2\times10^{-11}\right)T^{3}$	$63\le T\le1500$	[50]
$k_{\mathrm{O_2}}$	$1.6\times10^{-4}+\left(9.4\times10^{-5}\right)T-\left(2.8\times10^{-8}\right)T^{2}+\left(5.2\times10^{-12}\right)T^{3}$	$80\le T\le2000$	[50]